JUSTUS-LIEBIG-
UNIVERSITÄT
GIESSEN

DLR

Dissertation

Advancement of the DLR TAU Code Method to Simulate Two-phase Flow with Phase-change at the Interface with Applications in Upper Stages of Space Launch Systems

Presented by
David Keiderling

Justus - Liebig - University Giessen,
Faculty 07, Institute of Experimental Physics I
Prepared at the
Institute of Aerodynamics and Flow Technology
of the German Aerospace Center (DLR)
in Göttingen

February 2023

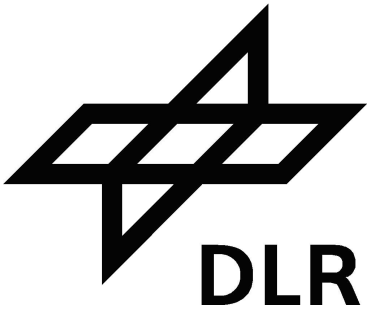

Advancement of the DLR TAU Code Method to Simulate Two-phase Flow with Phase-change at the Interface with Applications in Upper Stages of Space Launch Systems

Dissertation

submitted in fulfilment of the requirements for the degree

Doctor rerum naturalium

- Dr. rer. nat. -

presented by

David Keiderling, M.Sc.

Institute of Experimental Physics I of the Faculty 07
of the Justus - Liebig - University Giessen
Prepared at the
DLR Göttingen - Institute of Aerodynamics and Flow Technology
Department Spacecraft
February 2023

Supervisors

Prof. Dr. Klaus Hannemann†
Prof. Dr. Christian Heiliger

David Keiderling, M.Sc.

Advancement of the DLR TAU Code Method to Simulate Two-phase Flow with Phase-change at the Interface with Applications in Upper Stages of Space Launch Systems

First Reviewer: Prof. Dr. Christian Heiliger
Second Reviewer: Prof. Dr. Andreas Dillmann
Presented: February 2023

Per aspera ad astra.
Über raue Pfade gelangt man zu den Sternen.

Danksagung

Diese Arbeit wäre ohne die Unterstützung vieler Menschen nicht möglich gewesen. Zunächst möchte ich dem verstorbenen Klaus Hannemann danken, der mir die Chance eröffnet hat diese Arbeit anzufertigen und diese auch immer unterstützt hat. Großer Dank gilt auch den Mitgliedern der Abteilung Raumfahrzeuge am Institut für Strömungstechnik und Aerodynamik für die beständige Unterstützung bei allen Belangen, mit denen ich sie belasten musste. Hier sind allen voran mein ehemaliger Teamleiter Sebastian Karl und die Kollegen Tim Horchler, Stefan Fechter, Oliver Lietz, Jan Martinez Schramm und Volker Hannemann zu nennen! Ihre Unterstützung in technischen, administrativen sowie fachlichen Fragen und Diskussionen war stehts eine große Hilfe zur Anfertigung dieser Dissertation!

Zu vergessen sind aber auch die Kollegen aus dem Verbundprojekt Oberstufe nicht, die während meiner Zeit am DLR immer ein offenes Ohr hatten und mit denen man immer produktiv an Aufgabenstellungen arbeiten konnte. Hier sind vor allem Jens Gerstmann vom DLR Bremen und Peter Noeding sowie Martin Konopka von Airbus Defence & Space zu erwähnen. In diesem Rahmen danke ich auch der Airbus Defence & Space GmbH für die Bereitstellung der Daten zum KOALA Experiment, dass ich in dieser Arbeit nutzen durfte.

Weiterhin gilt mein Dank Martin Grabe, der die Übergabe der Promotionsbetreuung an der Justus-Liebig-Universität Gießen organisierte. Mein Dank gilt in diesem Zusammenhang ebenfalls Peter Klar und vor allem Christian Heiliger, der sich bereit erklärt hat, die Betreuung der Promotion von Klaus Hannemann zu übernehmen. Auch möchte ich Prof. Dr. Andreas Dillmann danken, der das zweite Gutachten übernommen hat.

Natürlich spielt auch der private Rückhalt eine wichtige Rolle und hier möchte ich vor allem meiner Mutter und meinem Vater für ihre fortlaufende Unterstützung danken, die mich immer begleitet hat! Für die anhaltende Motivation auch in schwierigen Momenten weiterzumachen danke ich meiner engsten Familie und Freunden!

Per aspera ad astra.
Through hardships, to the stars.

Acknowledgement

This thesis would not have been possible without the help of many people. First, I want to thank the late Klaus Hannemann, which offered me the chance to start this work. His continued support will never be forgotten. Another big portion of gratitude goes to the members of the Institute of Aerodynamics and Flow Technology, Department Spacecraft for their enduring support that I had to occupy them with. Special thanks goes here to my former team leader Sebastian Karl and colleagues Tim Horchler, Stefan Fechter, Oliver Lietz, Jan Martinez Schramm and Volker Hannemann. Their support in technical, scientific and administrative questions regarding this thesis were a great help to produce this work.

Not be forgotten should be the colleagues of the Research Association Upper Stage that always had an open ear and productive feedback during my time at the DLR. Here I want to name Jens Gerstmann of the DLR Bremen and Peter Noeding as well as Martin Konopka of Airbus Defence & Space. My gratitude also goes to the Airbus Defence & Space GmbH itself, which allowed me the use of experimental data from the KOALA experiment that I was able to use in this work.

Furthermore, my appreciation goes to Martin Grabe who organized the transition of this thesis to a new supervisor at the Justus-Liebig-University Giessen. In this respect my further appreciation goes to Peter Klar and foremost Christian Heiliger, who was willing to take over the supervision of this thesis from Klaus Hannemann. Additionally, I want to thank Prof. Dr. Andreas Dillmann for taking over the second certificate.

Finally, the private support is always very important! My gratitude here goes to my mum and dad for their ongoing support that I could always count on. For the continued motivation to keep going, I want to thank my closed family and friends!

Advancement of the DLR TAU Code Method to Simulate Two-phase Flow with Phase-change at the Interface with Applications in Upper Stages of Space Launch Systems

David Keiderling
M.Sc.

2023-February-1st

Abstract

The presented thesis discusses work that has been conducted to extend the German Aerospace Center (DLR) TAU Code to simulate heat and mass transfer in two-phase systems in launcher cryogenic upper stages. Preceding work has been performed to extend the incompressible version of the DLR in-house Computational Fluid Dynamic (CFD) Code TAU to simulate isothermal two-phase flows. A Volume of Fluid (VOF) approach and a finite volume discretization are used. Due to the grid handling in TAU, an algebraic solution of the interface position was necessary and implemented yielding shorter computation times compared to geometrical approaches on both structured and unstructured grids. This model was extended to simulate heat and mass transfer over the two-phase interface. The work includes updating the energy equation, the mass conservation equation and adapting the respective numerical simulation. Density deviations are included via the Boussinesq-approximation and heat convection is modelled by Fouriers law. The resulting changes were then tested and validated using basic test-cases and a complex use case of the stratification process within a dewar filled with liquid and gaseous hydrogen. The achieved results are presented in this work. Generally, an agreement

for the validation test cases with the analytical results were found although some issues with curved interfaces remained. The implementation was also able to simulate the complex test case of stratification, yielding compatible results when compared to the experimental data that has been provided to analyze the simulations.

Zusammenfassung

Die vorliegende Arbeit diskutiert die Erweiterung des DLR TAU-Codes um die Simulation von Massentransport in Zweiphasensystem von Trägerraketen zu ermöglichen. Dieser Arbeit gingen Aktivitäten voraus die den inkompressiblen DLR-eigenen CFD Code TAU um die Möglichkeit erweiterten Zweistoffsysteme zu simulieren. Dabei kommen ein sogenannter VOF Ansatz zum Einsatz sowie ein finites Volumen Verfahren. Aufgrund der Netzbehandlung in TAU war ein algebraischer Ansatz für die Auflösung des Interfaces nötig. Dieser Ansatz ermöglichte kürzere Rechenzeit im Vergleich zu geometrischen Verfahren. Dies gilt sowohl für unstrukturierte als auch für strukturierte Netze. Dieses Rechenmodell wurde nun ergänzt um Wärme- und Stofftransport über eine Zweiphasengrenzfläche darstellen zu können. Diese Änderungen beinhaltet eine Erweiterung der Energiegleichung, der Massenerhaltung sowie die Anpassung der entsprechenden numerischen Simulationen. Dichteänderungen werden durch den Boussinesq-Ansatz berücksichtigt und Wärmekonvektion durch das Fouriersche Gesetz. Die daraus resultierenden Änderungen wurden dann mit grundlegenden Testfällen getestet und ein komplexer Anwendungsfall wurde simuliert. Dieser bestand aus dem Stratifizierungsprozess in einem Behälter gefüllt mit flüssigem und gasförmigem Wasserstoff. Die erreichten Ergebnisse werden in dieser Arbeit präsentiert. Größtenteils konnte eine Übereinstimmung mit den analytischen Ergebnissen im Vergleich zur Simulation erreicht werden. Für gekrümmte Grenzflächen konnte jedoch eine komplette Übereinstimmung nicht erreicht werden. Der verfolgte Ansatz war auch in der Lage den komplexen Testfall der Stratifizierung zu simulieren und vergleichbare Resultate wie im zugrundeliegenden Experiment zu erreichen. Diese wurden zur Verfügung gestellt um die Simulation zu analysieren.

Contents

Acronyms

CBC	Convection Boundness Criterion
CICSAM	Compressive Interface Capturing Scheme for Arbitrary Meshes
CFL	CFL Number
CFD	Computational Fluid Dynamics
CNES	Centre National d'Etudes Spatiales
COMPERE	Comportement des Ergols dans les Réservoir
CSF	Continuum Surface Force
CST	Continuous Species Transfer
DLR	German Aerospace Center
DNS	Direct Numerical Simulation
EOF	Energy of Fluid
EOS	Equation of State
ESA	European Space Agency
FGMRES	Flexible Generalized Minimal Residual Method
GH2	Gaseous Hydrogen
GN2	Gaseous Nitrogen
GHe	Gaseous Helium
GEO	Geostationary Earth Orbit
CFD	Computational Fluid Dynamic
GTO	Geostationary Transfer Orbit
ILS	International Launch Services
IMFT	L'Institut de Mécanique des Fluides de Toulouse
KOALA	Kryogener Flüssigkeiten für Oberstufen-Antriebssysteme - Charakterisierung von LH2 für Angetriebene Flugphasen
LEGI	Laboratoire des Écoulements Géophysiques et Industriels
LH2	Liquid Hydrogen

LN2	Liquid Nitrogen
LOX	Liquid Oxygen
MECO	Main Engine Cut-Off
NASA	National Aeronautics and Spaceflight Agency
NetCDF	Network Common Data Format
ODE	Ordinary Differential Equation
ONERA	Office National d'Études et de Recherches Aérospatiales
PLIC	Piecewise Linear Interface-Capturing
PMD	Propellant Management Device
RCS	Reaction Control System
SIMPLE	Semi-Implicit Method for Pressure Linked Equations
SOURCE-II	Sounding Rocket COMPERE Experiment II
SST	Shear-Stress Transport
TAU	TAU
THETA	THETA
UQ	Ultimate-Quickest
VOF	Volume of Fluid
ZARM	Center of Applied Space Technology and Microgravity

Nomenclature

Greek Letters

α	Volume of Fluid Value	–
β	Expansion Coefficient	K^{-1}
β_f	CICSAM Weighting Factor	–
β_g	Growth Constant	–
χ	Solution of Transcendental Function	–
γ_f	Directional Weighting Factor	–
κ	Thermal Diffusivity	m^2/s
λ	Heat Conductivity	$W/m \cdot K$
μ	Dynamic Viscosity	$Pa \cdot s$
ν	Kinematic Viscosity	m^2/s
ρ	Density	kg/m^3
σ	Surface Tension	N/m
τ	Viscous Stress Tensor	Pa
θ_f	Angle of normal interface and connection vector of donor/acceptor	deg
φ	Mass Source Distribution	–

Latin Letters

c	CFL Number	–
c_p	Heat Capacity	$J/kg \cdot K$
D	Diffusion Coefficient	m^2/s
h	Enthalpy	J

H	Heaviside Function	$-$
L	Latent Heat	J/kg
L	Characteristic Length	m
m	Mass	kg
$\dot{m}$	Mass Flux	$kg/m^3 \cdot s$
$\dot{M}$	Mass Flow Rate	kg/s
N	Normalization Factor	$-$
p	Pressure	bar
q	Heat Flux	W/m^2
r	Radius	m
S	Surface	m^2
t	Time	s
T	Temperature	K
u	x-Velocity	ms^{-1}
v	y-Velocity	ms^{-1}
V	Volume	m^3
w	z-Velocity	ms^{-1}
x	x-Position	m
y	y-Position	m
z	z-Position	m

Similarity Numbers

Gr	Grashof Number	$-$

Ja	Jakob Number	–
Pr	Prandtl Number	–
Ra	Rayleigh Number	–

Subscripts

0	Initial
$cell$	Cell
int	Interface
K	Critical Point
PCH	Phase Change
ref	Reference
sat	Saturation
smo	Smoothed
v	Vapor
W	Wall

List of Figures

List of Tables

1 Introduction

In the aspiration to improve upper stages of launch vehicles for demanding tasks, one aspect of this optimization is a detailed understanding of the thermal behavior of propellant in these mentioned upper stages of launch vehicles. A lack of understanding of the involved processes in the propellants can result in false orbit insertions or the possibilities of launch mishaps. At the end of 2012 a Proton launcher with a Breeze M upper stage operated by International Launch Services (ILS) had an incomplete fourth burn of the upper stage. The error occurred on the oxidizer side of the turbo-pump of the hydrazine/nitrogen-tetroxide engine. Unexpected heating caused a concentration of oxidizer gas at the inlet line to the Breeze-M main engine, yielding to an eventual over-speed of the oxidizer turbo-pump bearing (see [12]).

The payload finally reached its intended orbit after four additional engine burns of the payload propulsion system, reducing the planned mission time from 15 to 11 years (see [13]). Important aspects of cryogenic propellant management are an active field of intense research, like the chill-down processes, liquid behavior in Propellant Management Device (PMD) or phase change processes during long coasting phases between upper stage engine burns as described by Gerstmann [14].

In the presented work the implemented improvements of the two-phase flow modeling in the German Aerospace Center (DLR) TAU code for non-isothermal cases are described. The TAU code is a computational fluid dynamics tool developed by DLR. It is capable of simulating viscous and inviscid flows on structured and unstructured grids in Mach regimes ranging from low subsonic to hypersonic flows. The two-phase model is based on a VOF approach. The utilized VOF formulation is especially useful since due to the dual-grid approach of TAU (TAU) the exact cell and face geometry is not available during the computation. The VOF method therefore enables an analytical solution of the transport equation. The scalar convective transport equation of the VOF variable is solved with the Compressive Interface Capturing Scheme for Arbitrary Meshes (CICSAM).

1.1 *Problem Setting*

The main field of interest for this work was the application of Computational Fluid Dynamic (CFD) simulations of two-phase flows for the investigation of European launch vehicles, such as the Ariane 5 or the upcoming Ariane 6 launcher classes of the Ariane-

Group. Figure 1 is a schematic depiction of the Ariane 5 rocket with a cut through the lower, upper stages and the booster.

Figure 1: Ariane 5 launch vehicle. Reprinted with permission from [1]. Copyright: **Arianespace - ESA - NASA**

Visible at the bottom part of the cut is the upper stage itself with its Liquid Oxygen (LOX) and Liquid Hydrogen (LH2) tanks and the HM7B engine. Connected through the payload adapter are either two payloads that are separated by the Sylda 5 structure or one major payload (as depicted here with the James-Webb Telescope). Those mentioned double payload often requires the separation into two different orbits at different elapsed times during the launch mission. Thus, a reignition of the upper stage engine is required, especially when two different orbits are needed in order to reach the designated position of the satellites. This can also be the case for complex orbits for single spacecrafts. Additionally, during the resulting coasting phase the upper stage is exposed to the variable space environment with changing acceleration levels due to the Reaction Control System (RCS) and alternating thermal loads resulting from attitude and the relative position to the earth or the sun.

Figure 2 visualizes the sequence of an Ariane 5 launch campaign for the common example of a commercial Geostationary Earth Orbit (GEO) mission that most commonly transfers telecommunication satellites into orbit. The launch begins

with the ignition of the central core stage and the solid rocket boosters. After separation of the two boosters and the following Main Engine Cut-Off (MECO), the upper stage will ignite to bring the payloads on a Geostationary Transfer Orbit (GTO) to deliver the satellites in their designed orbit. Here the first payload will be separated, followed by the separation of the Sylda payload adapter. Consecutively, the second payload will be released, possibly after an engine reignition to adjust its orbit. Finally, the upper stage needs to be decommissioned to full-fill orbital debris avoidance requirements. Thus, another engine utilization is possible before the stage is passivated and to re-enter or be transferred into a graveyard orbit.

During these maneuvers several critical phases are to be considered in order to design an efficient upper stage that can function under different mission scenarios in a reliable and cost-efficient manner.

One of the major phases is the propulsive period where either the main engine of the first stage (including boosters) or the main engine of the upper stage is active and delivering thrust. Thereby, increasing the speed of the launcher and forcing the propellant towards the bottom of the tank. During this phase sloshing, primary in lateral direction, is important as well as the forces that the fluid motion inputs into the rocket that have to be handled by the RCS. This needs to be considered during development and the optimization of stages. It is also required to know the propellant motion during this phase in order to design and increase efficiency of PMD like baffles and anti-slosh rings. Concentration and vaporization of droplets during this phase influences the pressure within the tank and thereby the feeding system. Furthermore, heat and mass transfer at the walls and the fluid interface play a role and thermal stratification during draining can influence the performance of subsequent engine parts like turbo pumps, feed lines etc.

Following these propelled phases, the engine shutdown (MECO) is another critical part of the trajectory where the forces that pressed the propellant towards the bottom are removed and fluid within the tanks will now start to experience reduced gravity (central stage) or even microgravity (in the upper stage). These changes in acceleration levels can amplify sloshing thus influencing heat and mass transfer at the interface or wall and also influencing the force budget of the stage making it necessary to correct altitude by the RCS. Bubble and droplet formation can occur.

Thereafter, reduced gravity levels influence the propellant and reorientation occur in the liquid and gas phases. Sloshing is dampened but still can influence the RCS. Now

thermal effects play a major role, since the heat and mass transfer at the interface is strongly influenced and boiling, natural and Marangoni convection as well as thermal stratification are occurring. Also, the gas mixture in the tank (consisting of pressurant gas and propellant vapor) can be diluted into the liquid.

In order to provide the aforementioned flexibility for the orbits and the mission, the restart of the engine yields to its own set of difficulties like geyser formation due to the sudden increase in acceleration, thereby fragmenting the liquid bulk or possible inclusion of bubbles within it. The propellant then needs time to settle and outgas. Caused by the required pressurization and de-pressurization, bubbles can form within the fluid or due to chill-down effects during these sequences.

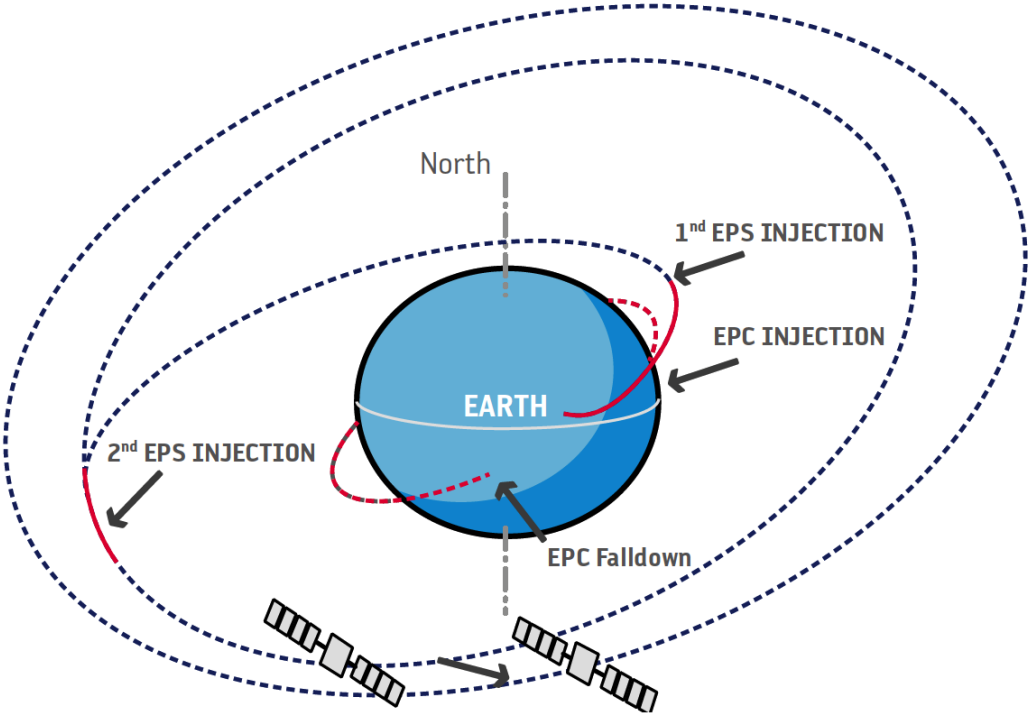

Figure 2: The Ariane 5 launch sequence. Reprinted with permission from [2]. Copyright: **European Space Agency (ESA)**

There are two major research groups that investigate these kinds of effects and provide insight into the involved physics in Europe. The French-German Comportement des Ergols dans les Réservoir (COMPERE) project and the sole German main project Research Association Upper Stage. Within the COMPERE research consortium the main

focus is to understand fluid motion and related physical processes in the upper stages. The group consists of members from industry like Air Liquide, Airbus Defence & Space, Cryospace and members of the academic world like L'Institut de Mécanique des Fluides de Toulouse (IMFT), Laboratoire des Écoulements Géophysiques et Industriels (LEGI) and Center of Applied Space Technology and Microgravity (ZARM) and the research institute of Office National d'Études et de Recherches Aérospatiales (ONERA). Also Centre National d'Etudes Spatiales (CNES) and DLR as agencies are involved and provide the necessary funding.

The Research Association Upper Stage a DLR funded and initiated a major research project that is concerned with technology development for upper stage applications within the European launcher family [14]. Participants in the group are the national space industry (Airbus Defence & Space and MT Aerospace), ZARM, as well as four DLR Institutes (located in Bremen, Lampoldshausen, Göttingen and Braunschweig). Since the announcement of the Ariane 6 the focus of the group is concentrated on this new launcher. Within the research project several technical areas are of interest:

- Cryogenic fuel handling
- The further development of DLR TAU
- Simulations of fuel delivery systems
- Fiber composite technology
- Avionics

The presented work was associated with the development of DLR TAU. Furthermore, experimental investigation in the Cryo-Lab of DLR Bremen were conducted by Gerstmann et al. [15]. Additional information on these related fields of activity will be provided in section 2.

All these activities highlight the relevance of the mentioned challenges in the design and optimization of cryogenic upper stages. The present work is intended to contribute in this field by developing the DLR TAU in order to being able to study incompressible two-phase flows with phase change and contribute thereby to the efforts of the Research Association Upper Stage in understanding propellant behavior in reduced gravity and under complex mechanical and thermodynamic loads for an extended period of time.

1.2 *Solution Approach*

In order to achieve the goal of developing the DLR TAU to being able to mimic phase change, a study on numerical approaches was conducted in order to identify the most promising model to simulate phase change in a CFD framework like the DLR TAU code.

Beginning with the relevant equations of state, a summary of different numerical approaches will be covered in section 2.2. After several tests a suitable approach was selected and implemented in the numerical solver. Eventually, this implementation was tested with simple basic test cases that are widely accepted in the area of phase change implementations. The results are presented in section 5.

Continuing from this basic validation, a more application related simulation was needed to be selected for this study. The so-called Kryogener Flüssigkeiten für Oberstufen-Antriebssysteme - Charakterisierung von LH2 für Angetriebene Flugphasen (KOALA) test case was found to be a suitable candidate and the test specifications and results were kindly provided by Airbus Defence & Space of Bremen. In this work the experimental and numerical set-up of this test are detailed described in section 6 in sub sections 6.2 and 6.3, respectively. In sections 6.4 and 6.5 these results will be presented in detail and discussion will take place in section 7.

2 Modeling Phase Change: State-of-the-Art

2.1 *The Physical Process of Phase Change*

Phase-change is an omnipresent process that takes place on a day-to-day basis. For example when water is heated for a coffee, when electricity is produced in turbo machinery or when a launch vehicle puts the latest telecommunication satellite into its designated orbit.

In this thesis we are mainly concerned with the liquid and its vapor. Here vapor is defined as a real gas near its liquefaction, also called condensation, at relatively low temperatures. At higher temperatures vapor can be treated as an ideal gas, which corresponds to equilateral hyperbola in the p-v diagram, which is shown in the right cut-out of figure 3 and corresponds to the thermal equation of state in the following form:

$$p \cdot v = R \cdot T \,. \tag{1}$$

The basis for the understanding of phase-change problems is the p-v-T diagram or phase diagram that is shown in figure 3 for a pure substance and shows the relation between pressure p, specific volume v and the temperature T and the corresponding state. The diagram depicts different equations of state for the three phases gaseous, liquid and solid and their mixtures. Those are solid-liquid or the melting area, the saturated liquid-vapor or wet vapor region and the solid-vapor or sublimation region. When moving at constant pressure through the diagram a solid, with low specific volume, is heated causing only small changes in volume. Finally, the melting region is reached, and the solids starts the transition into the liquid phase by increasing its specific volume while remaining at the melting temperature. After the solid is completely melted, adding additional heat will raise the temperature of the liquid of the pure substance, which will eventually reach the evaporation line. Here the state of the substance is changed again, now becoming vapor and transiting the saturated liquid-vapor region at constant temperature. The evaporation process is finished when the complete liquid has changed the state to vapor. On the p,v plane of figure 3 this moment is depicted as the saturated vapor line, from there on only vapor exists whose temperature and volume are further increased by adding heat.

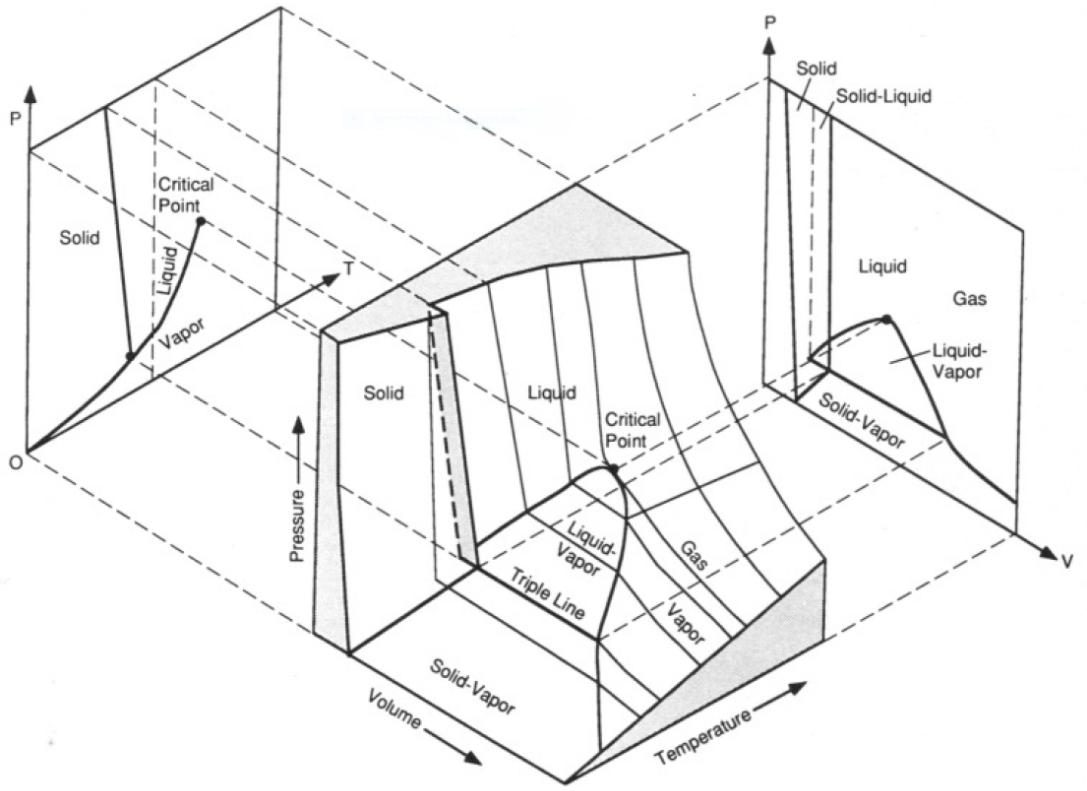

Figure 3: The p-v-T diagram or phase diagram. Reprinted by permission from Springer US from [3], COPYRIGHT (2002).

There are two special ways for the substance to progress that omits one of the aforementioned phases. When for a solid the pressure is low enough it will immediate transition from the solid state into the gaseous state. This process is called sublimation and might occur to fallen snow above certain altitudes where the air pressure is low enough e.g. the Rocky Mountains. Furthermore, at high temperatures and pressures a liquid can directly change to vapor, avoiding the wet vapor region entirely, resulting in no discontinuity between the two phases. This will happen above the critical point K, which is a characteristic value for every substance, where saturated liquid and vapor line meet. It is only below this temperature an equilibrium between liquid and its vapor exists. This point is defined by a specific pressure p_K, specific temperature T_K and a characteristic volume or density $\rho_K = 1/v_K$.

There is also a constant pressure and temperature level where solid, liquid and vapor phases exist in an equilibrium - the so-called triple line Tr. To get an overview, the values

of some common substances are presented in table 1 with their corresponding critical and triple values.

Fluid	Water	Nitrogen	Oxygen	Hydrogen
$p_k\,[bar]$	221.3	33.9	50.8	12.97
$\rho_K\,[kg/m^3]$	310	311	410	31
$T_K\,[K]$	647.3	126.2	154.75	33.25
$p_{Tr}\,[bar]$	0.00611	0.126	0.00152	0.0704
$T_{Tr}\,[K]$	273.16	63.18	54.36	13.84

Table 1: Critical and triple line fluid properties.

When keeping the specific volume in the p-v-T diagram constant one gets the p-T diagram, which again differentiates the three phases, as is visible in figure 3 on the right cut-out. Those regions are now divided by the melting curve (solid to liquid), the sublimation curve (solid to vapor) and, of most interest in the present work, the saturation pressure curve.

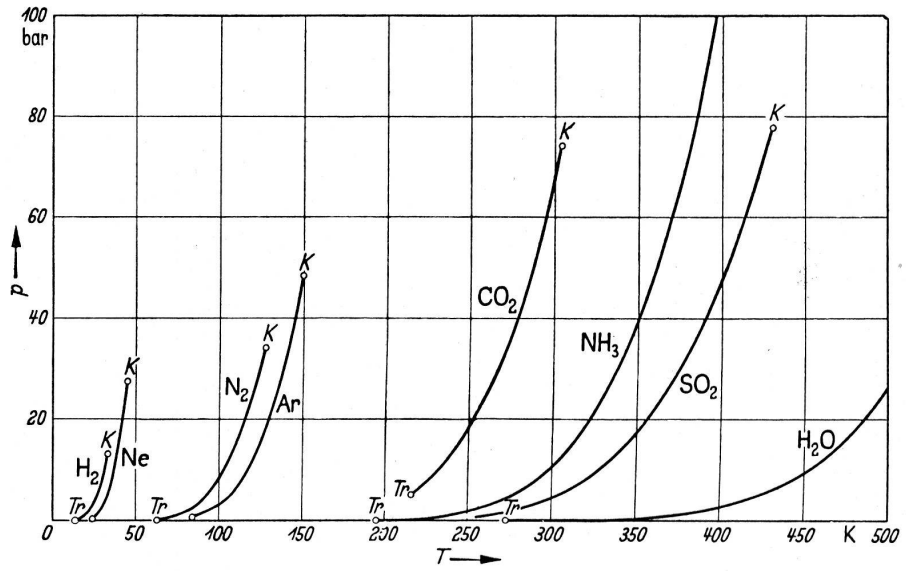

Figure 4: The saturation pressure curve for different substances in p-T diagram. Tr donating the triple point and K the critical point. Reprinted by permission from Springer: Nature from [4], COPYRIGHT (2012)

In heterogeneous areas like the wet-vapor region the two corresponding phases need to have the same pressure and temperature in order to coexist and be in an equilibrium. Furthermore, the system is only entirely defined when the composition of the two

phases is known as well. The gradient of the saturation pressure curve is known as the Clausius-Clapeyron equation and can be defined for all three of the two-phase areas. Since evaporation and condensation is our main concern in this work we will focus on the wet-vapor region and the gradient of the saturation pressure curve. The Clausius-Clapeyron equation for these regions reads:

$$\frac{\mathrm{d}p}{\mathrm{d}T} = \frac{1}{T} \cdot \frac{h'' - h'}{v'' - v'} \,. \tag{2}$$

with $h'' - h'$ being the measurable enthalpy difference of the two phases and $v'' - v'$ the corresponding difference in specific volume. Where the $'$ indicates the initial state and $''$ the final state. For every pressure level a related temperature exists and vis-versa where liquid is evaporating. This pressure is the saturation pressure p_{sat} and associated saturation temperature T_{sat}. The saturation pressure curve relates to $p_{sat} = p_{sat}(T)$ as function of temperature. At $p < p_{sat}$ the fluid is completely gaseous and at $p > p_{sat}$ it is in existence as liquid. The saturation pressure curve is characteristic for any substance and starts at the triple point and runs to the critical point. Some trends are depicted in figure 4 as curves in the p-T diagram. Usually, these curves are determined by measurements and some simple but accurate representations were developed by Wagner [16]. With the help of the Wagner equation (equation (3) from Hase [17]) it is possible to calculate the saturation pressure p_{sp} for a given temperature or vise-versa.

$$\ln p_{sp_r} = \frac{a\tau + b\tau^{1.5} + c\tau^3 + d\tau^6}{T_r} \,. \tag{3}$$

Where a,b,c and d are the coefficients of the Wagner equation, which are characteristic for every substance, $p_{sp_r} = p_{sp}/p_c$ is the reduced saturation pressure and $T_r = T/T_c$ the reduced saturation temperature with the subscript c donating the critical values of temperature and pressure. Furthermore, τ is a reduced temperature in the form:

$$\tau = \frac{1 - T}{T_C} = 1 - T_r \,. \tag{4}$$

An overview of saturation pressure curves for different substances can be found in

figure 4. Therefore, equation (3) can be used to determine the pressure development with regards to the temperature as shown in figure 4, that is a p,T projection of figure 3 (compare left cut-out).

The needed evaporation enthalpy L can be visualized in a T-s diagram where the entropy s is increased due to the heat flux into the fluid. In this case the temperature remains constant until all liquid is evaporated and therefore can be expressed as:

$$L = h'' - h' = T(s'' - s')\,. \tag{5}$$

By applying the first law of thermodynamics, that energy in a closed system is constant, where one starts at the liquid saturation line (1) and ends at the saturated vapor line (2). The change in energy can now be expressed

$$u'' - u' = u_2 - u_1 = q_{12} + w12\,. \tag{6}$$

Since we assume an irreversible process

$$w_{12} = \int_1^2 p\mathrm{d}v = -p(v'' - v')\,. \tag{7}$$

With the enthalpy definition $h = u + pv$:

$$q_{12} = h'' - h' = L = u'' - u' + p(v'' - v')\,. \tag{8}$$

Thus, the applied heat q_{12} is split into a volume work $p(v'' - v')$ and the change of the internal energy $u'' - u'$. The largest amount of heat will go into the breakup of the molecular bounds to transfer from the dense liquid to the much looser bounds of the gas phase resulting in an increased internal energy. Only a smaller fraction is required for the volume work.

For an isobaric phase change process figure 5 demonstrates the steps the liquid will pass until only vapor is present in the container. The compressed liquid at state 1 will heat up due to an energy influx until the saturation temperature is reached, meanwhile expanding

due to the dependence of the density on the temperature (state 2). At this point in the shown T-v diagram the saturation liquid line is crossed, and the first vapor bubble will manifest itself. At any point between state 2 and 4 a mixture between saturated liquid and saturated vapor is present (state 3). During this phase of the evaporation process the temperature will remain constant, and all added energy is spent on the aforementioned volume work and increase of internal energy. Once all the liquid is evaporated, meaning the saturated vapor line is crossed, the temperature can increase again. One is now in state 4. Adding additional heat will result again in the increase of the temperature and an increase of the specific volume reaching the state 5, which correspondents to superheated vapor - an ideal gas.

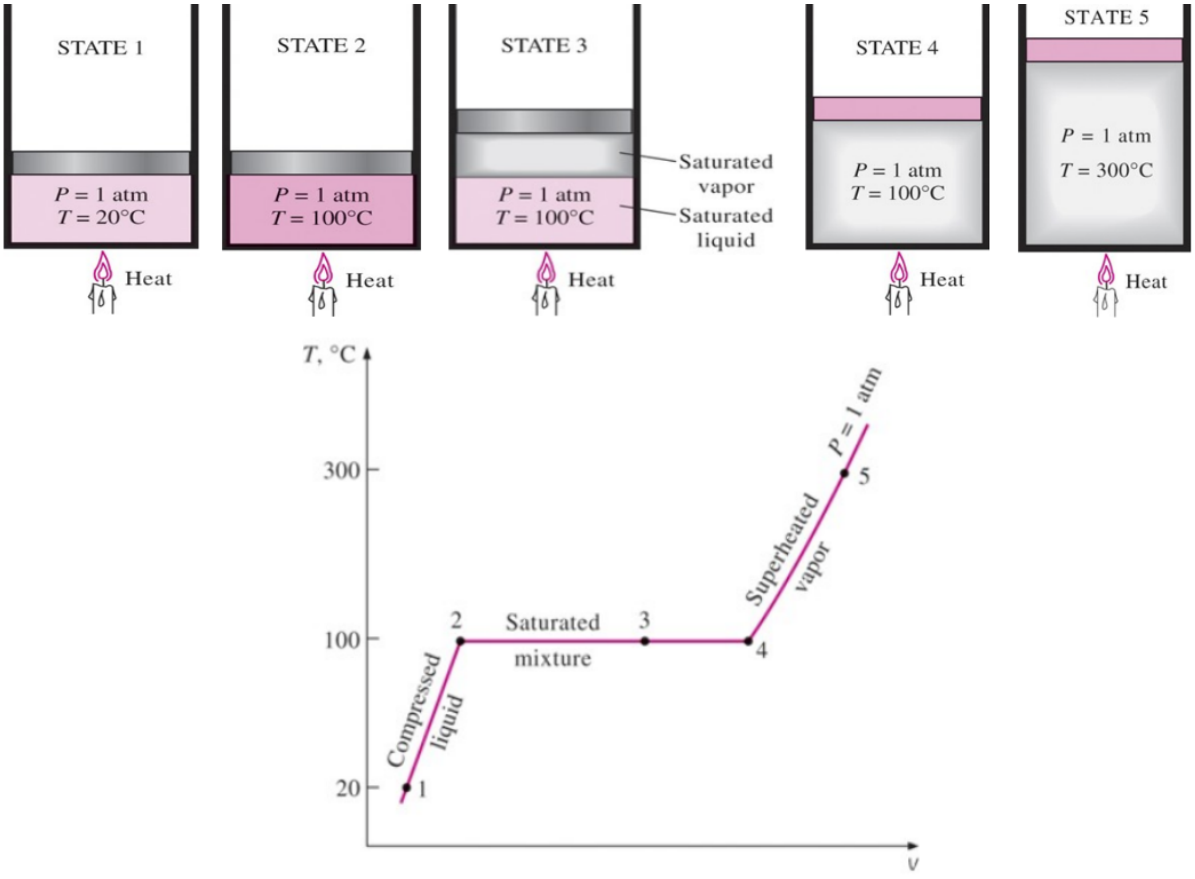

Figure 5: The change of state for heating and evaporating water at a constant pressure and schematic representation of the phase change process at the different states. Reprinted by permission from McGrawHill LLC from [5], COPYRIGHT (2015)

The behavior described can be repeated at different pressures and the same effect will occur. In cases where the critical pressure is exceeded there is no simultaneous occurrence of two phases (liquid and vapor) possible. This is also the case when the pressures are below the triple point level for the corresponding substance.

2.2 *Numerical Modeling Approaches towards Phase Change*

First attempts to simulate phase change where made by Son and Dhir [18] through using the energy balance as well as the mass continuity at the interface and implement it into the two-phase algorithm introduced by Sussman et al. [19]. Its resulting method is applied to a one-dimensional test problem and a more sophisticated film boiling problem near the critical pressure.

Juric and Tryggvason [20] used a front tracking method and applied a simple phase change model at the interface that is mainly based on the temperature difference at the interface and based on Tanasawa [21]. This is also applied to simple one-dimensional problem and film boiling.

Further early attempts to model the processes involved in phase change have been made by Hardt and Wondra [22]. They implemented a general model, which is usable in a VOF implementation. In this work the interface-concentrated source term is shifted beyond this region towards a zone that is close to interfacial region but distinguished from it. This smeared-out version of the source terms is considered to avoid numerical instabilities. The required specific mass flux was determined in Tanasawa [21] and a Piecewise Linear Interface-Capturing (PLIC) approach to two-phase representation is applied. In order to achieve this distributed source term an inhomogeneous Helmholtz equation is solved. Hardt and Wondra [22] then solved basic phase change test cases and continued with a more advanced film boiling test simulation.

An additional approach to phase change has been made by Wohak [23] who went into greater detail of modeling the actual physical phenomena at the interface. The main concern of Wohak [23] is the simulation of bubble phenomena involving phase change at the interface. He utilizes an interface-concentrated source term that is calculated from temperature gradient at the interface with a fixed distance in the denominator. His model is also expanded to three fluid flows. These results have been improved and developed further by Kunkelmann [6] and by Batzdorf [24].

In the work of Welch and Wilson [25] the gradient at the interface is calculated as

the driving element of the phase change model. This is done by avoiding calculations of gradients across the interface into the other phase state of the fluid. Thus, estimating the gradient of each distinguished phase separately. The approach is validated with the Stefan-, Sucking-Interface- and Scriven-Problem (see chapter 5) and used to simulate horizontal film boiling.

Kunkelmann [6] advanced the work of Hardt and Wondra [22] by applying a more sophisticated way in determining the mass flux due to phase change with the gradient that appears at the interface. Furthermore, he used a description of the three-phase contact line to estimate the micro-scale heat and fluid flow by including the work of Stephan and Busse [26]. This very broad approach, incorporating several important features for relevant simulations like transient heat conduction in solids and applicability to highly distorted interfaces, is applied to basic test cases as well as complicated meniscus evaporation and bubble flow regimes. Batzdorf [24] expanded this approach by using it to investigate the heat transfer into impinging drops.

Further improvements of Kunkelmann [6] have been reported by Ma and Bothe [27]. In Ma and Bothe [27] a new two-scalar approach is used to solve the heat transfer that utilizes two separate temperature fields, one for every distinct phase, to compute the interfacial temperature. This approach is meant to omit the volume averaged temperature in the interface regions and corresponding uncertainties. The article presents results for basic heat and mass transfer test cases and a liquid film on structured substrate and the rupture of a locally heated liquid film. In a continued effort the work of Deising et al. [28] introduces an improved Direct Numerical Simulation (DNS) method to handle arbitrary fluid interfaces involving high viscosity and density ratios as well as species transfer. They present a single field method, based on conditional volume-averaging techniques, taking species transport via diffusion into account but not phase change. Also, the proposed stability and accuracy of the Continuous Species Transfer (CST) model promises an improvement for the calculation of phase change phenomena by means of the avoidance of parasitic currents.

In consecutive scientific works Rieber [29], Hase [17] and Schlottke [30] developed a numerical method for two-phase simulation (Rieber [29]) as well as the modeling of phase change of droplets and their behavior (Hase [17]). Great emphasis is put into the calculation of the interface velocity, which is used to progress all concerned variables in the flow field. The mass flux rate of evaporation and condensation is determined via a simple

model in order to focus on fluid mechanical implementation. Schlottke [30] improves the approach of Hase [17] by a model to estimate the phase change mass source via the vapor gradient.

Using the Energy of Fluid method Wróbel [31] also successfully implemented a phase change model. This approach is based on the calculation of a VOF value change due to evaporation and condensation and uses a different logic than previously described methods. The scheme is calculating interface-concentrated source terms by estimating the change within the VOF scalar due to the temperature difference between the local temperature and the interface temperature. Furthermore, the source terms of the temperature equations are derived with the changing VOF scalar value. Finally, a mass source can be deducted from the volume change. An advantage of the scheme is that a reconstruction of the interface position can be omitted since only the temperature difference to the saturation value and the VOF value in a computational cell is required. No basic validation test cases similar to the other studies were presented but an application of the phase change scheme to investigate the injection of coolant into a duct containing hot liquid and its vapor. Wróbel [31] also discusses that the Energy of Fluid (EOF) method is not able to provide information on the phase change rate.

Describing phase change with sharp source terms, Sato and Ničeno [7] were able to get good results for the basic test cases and apply their model successfully to bubble growth processes. Sato and Ničeno [7] use a concentrated source term at the interface in order to implement the jump conditions and the effects of phase change into the incompressible Navier-Stokes equations. The introduced model uses the heat flux at the interface to determine mass flux rates by applying a second-order-accurate scheme for the gradient reconstruction. His approach delivers good agreement for the basic test cases as well as for more complex applications of rising bubbles and nucleate pool boiling.

Defining benchmark test cases based on the aforementioned analytical solutions (also see 5) Tanguy et al. [32] used these cases to compare the numerical schemes of the Ghost Fluid and Delta Function methods as well as high order extrapolation schemes on structured fixed computational grids. The paper highlighted the importance of the modeling of the thermal boundary layer and the importance of using an accurate extrapolation scheme to predict the correct results for the defined benchmark tests.

Due to a high industrial demand for phase change simulation tools in order to predict very different processes commercial CFD codes also investigate the improvement and

extension of phase change models. In the realm of the simulation of upper stage propellant management FLOW-3D is used in industry and academia to simulate the life cycle of upper stages. Konopka et al. [33] provide insight in some of the activities involving FLOW3D. Konopka et al. [9] present a comprehensive study about the extensions of the CFD suite in order to simulate phase change phenomena with the specialization of utilizing this code for CFD simulations for cryogenic upper stages. An analogue approach as proposed by Kunkelmann [6] is applied to the basic test cases and the Sounding Rocket COMPERE Experiment II (SOURCE-II) experiment (see for example Schmitt [34]) with an overall satisfying result. Continued effort in the Joint Research Project Upper Stage is under way to further improve the Flow-3D capabilities of phase change CFD-simulations.

The open-source code OPENFOAM is also capable of using phase change models and is used and improved further at ZARM and DLR Bremen. Compared to the aforementioned flow solvers, a different class of numerical solvers to predict the conditions of cryogenic propellants in an upper stages of launch vehicles exist. This approach solves one-dimensional continuity, momentum and energy equations for an internal flow. Another part of the code solves the heat equation by modeling a system with "nodes" and "conductors". These parts are then connected and form a simpler one-dimensional approach to the modeling of fluid behavior, which is applicable to mission analysis of the whole upper stage in comparison to high computational demand of CFD solvers. This software is then capable of simulating stratification, rotation and sloshing events by incorporating correlations and simplified model approaches to the defining physical processes. One such simulation environment is used by National Aeronautics and Spaceflight Agency (NASA) and is based on a commercially available code called SINDA/FLUINT and is used in the Launch Service Program by Schallhorn et al. [35].

Likewise, the ArianeGroup uses their own in-house 1-D tank flow solver, which is used by Konopka et al. [33] in order to perform mission analysis and design tasks to evaluate complex mission profiles and systems architectures. The KOALA test case, that will be investigated in chapter 6, was also studied with this approach of Konopka et al. [9]. Some of these works are also discussed in the next chapter.

2.3 Experimental and Numerical Investigations of Phase Change for Launcher Applications

Evaporating and condensation propellant has been investigated since the Apollo era when restart ability and long coasting phases started playing a role. A famous large scale experiment is the test flight AS-203 of the Saturn S-1B stage, which used an instrumented upper stage to look at basic flow parameters like pressure, temperature and mass flow during ascent and the in orbit phase of the experiment by NASA [36]. Video material from the LH2 tank interior is also available.

Although these measurements are limited, it remains one of the only large-scale experiments that is publicly available and several studies have been conducted to interpret the results. Grayson et al. [37] predicts this low-gravity, cryogenic self-pressurization test with an axis-symmetric model that is able to reproduce LH2 surface motion, as well as boil-off and thermal stratification in both, the liquid and gaseous phase. Heat is introduced via the tank forward dome, side wall, aft dome and common bulkhead. Test and simulation confirm that gas and liquid stratify in a low-gravity natural convection and pressure increases due to boil-off at the interface.

This work is expanded by Kartuzova and Kassemi [38] who also consider turbulence effect in the tank by using two engineering models namely the k-ϵ and the Shear-Stress Transport (SST) k-ω model. It was found that, next to an also tested sharp interface model, the VOF model is the best choice to simulate initial turbulence level, interfacial turbulence and turbulent heat transfer with reasonable accuracy at the price of small-time steps and high computational resources. Since the sharp interface model showed insufficiency when taking interfacial deformation effect on turbulent heat transfer into account, it was concluded that a VOF model approach is more promising in producing accurate results for thermal stratification and self-pressurization.

On a smaller scale sloshing in a 1750 l spherical tank was investigated by Moran et al. [39] under normal gravity. Different parameters like sloshing frequency, ramp pressure, pressurant type and ullage volume were varied and the influence on tank pressure and tank wall, as well as fluid temperatures were investigated extensively. There was liquid and slush Hydrogen in use during closed tank testing. Some major findings of the experiments included pressurant mass and flow rate requirements and pressure collapse magnitudes. It was also shown that sloshing excitation frequency and amplitude has an important effect on the ullage and its collapse. Although secondary effects, pressurant type and ullage

volume are also important parameters that change the thermodynamic response of the storage tank.

Furthermore, Hasan et al. [40] conducted self-pressurization experiments of a flightweight LH2 storage tank under the influence of low heat flux. The $4.89\,m^3$ tank, made in a low mass-to-volume fashion and using high performance multilayer thermal insulation, was subjected to different levels of low heat flux (0.35, 2.0 and $3.5\,W/m^2$) under normal gravity. It could be shown that with an increased heat flux the pressure rose and the stratification increased. Also, the pressure rise rate depends strongly on the heat flux, where the lowest heat flux produces a rise rate that is comparable to the homogeneous rate whereas the highest heat flow yields to almost three times the pressure rise rate.

Furthermore, initial conditions influence the initial pressure rise rate significantly. On the contrary the quasi-steady pressure rise rate is nearly independent of these initial conditions. Hence, in order to measure the steady-state rise rates, a pre-chilled tank is required since the initial pressure rise rates exceeds the steady-state value.

Based on these experimental results numerical follow up studies were performed for example by Barsi and Kassemi [41] in order to investigate performance of two-phase CFD models to analyze their prediction capabilities in the design of cryogenic storage systems. A lumped vapor CFD model was used to simulate the self-pressurization of the aforementioned experiments by Hasan et al. [40] of a closed spheroidal tank system under normal gravity. The model delivered reasonable predictions for the pressure rise during self-pressurization of a variety of fill level. Since a uniform heating distribution was assumed, some discrepancies arose when there was the possibility for a non-uniform heating of the tank walls at median fill levels.

Flow patterns and thermal stratification of a cylindrical tank were investigated in Lin and Hasan [42] in a numerical simulation but without experimental comparison. Parameters like the modified Rayleigh number, Prandtl number, tank aspect ratio, wall material parameters, and wall heat-flux distribution on the liquid velocity and temperature fields were altered and their influence on the flow investigated. The liquid region was decoupled from the vapor region since an effect of vapor superheat and vapor motion on the interface was assumed to be of no major influence on the flow. Furthermore, a constant pressure in the system was assumed, bottom and interface were set to fixed temperatures and the wall heat was either uniform or divided in two distinguished regions of different heat-flux. Conclusions on the flow patterns and the temperature distribution were possible

and influences of parameters on both were investigated.

A broader overview of NASA efforts on the development of cryogenic storage technology can be found by Moran [43], where summary results, key impacts and ongoing efforts are listed. Included are also experimental data for different fluids like hydrogen, oxygen and methane. Furthermore, numerical efforts on lumped parameter CFD and engineering tools are discussed.

In recent years, notably after the successful introduction of the Ariane 5, efforts have been under way to improve the understanding of propellants, tanks and management devises for rocket upper stages within the consortium that is producing the European launchers. The goal of this program is to improve capacity and operational safety of the European upper stages. Within this program several sounding rocket and drop tower experiments have been conducted.

One of the centers of European and especially German efforts for improving the design of launch vehicle upper stages is the ZARM, which conducted and contributed to several well-known experiments in this field. The ZARM is mainly concerned with the investigation of fluids in microgravity and conducts drop experiments at its drop tower facility. The drop container with experiments experiences up to $4.7\,s$ of microgravity. The set-up consists of the experimental container that is made of borosilicate that is filled with relevant fluid and is again included in an evacuated stainless-steel container. This container is enclosed by another cylinder, which is filled with liquid helium, which acts as a cooling bath to shield the experiment from outer heat flow. Finally, this set-up is housed in an also evacuated cryostat that will be dropped in the tower.

Among others, the ZARM conducted several reorientation experiments by Kulev and Dreyer [44] and those were already investigated with the DLR TAU code by Meyer [45]. Furthermore, isothermal and non-isothermal experiments were conducted with a para-hydrogen filled experimental container where the gas phase is comprised of para-hydrogen vapor. Both experiments will see the initial free surface rise due to capillary effects with the isothermal case experiencing negligible or minimal evaporation of the fluid. Only in the strong non-isothermal case the evaporation will play a major role, especially at the wall contact line. A detailed description and numerical analysis of the experiments can be found in the work by Schmitt [34].

Under the patronage of the French-German research group COMPERE a suborbital flight experiment (SOURCE-II) was conducted to study the free surface behavior of a two-

phase, single-species system with non-isothermal boundary conditions in reduced gravity investigating active- and self-pressurization, filling, pressure reduction and boiling. The used storage tank had a hight of 120 mm and a radius of 30 mm and was made from quartz class. Through two feed lines the tank was filled with the test liquid HFE-7000 and pressure control was performed through the top. A diffuser at the end of the vapor line prevented a direct flow of entering vapor on the free surface. Two heaters were installed at the bottom and at the top to establish a temperature gradient along the wall.

At the beginning of the experiment the storage tank was evacuated and subsequently filled with liquid HFE-7000 in two filling events. Afterwards, four pressurizations events with gaseous HFE-7000 took place at different times and varying vapor masses with an automated venting after the first pressurization event. The total experimental time that was investigated by ZARM was 210 s. Other partners also studied boil-off, stratification and reorientation events. Further information, among others, and a comparison with a numerical simulation performed by the commercially available codes FLOW-3D and FLUENT can also be found in Schmitt [34] and Schmitt and Dreyer [46] where reasonable predictions of the development of pressure and temperature are presented for the SOURCE-II experiment.

A lot of these work packages were conducted under the mentioned COMPERE program (see chapter 1.1). The main concern is the improvement of the understanding of fluid motion in tanks of upper stages of launch vehicles.

The group conducted experiments concerning the propelled and ballistic flight phases with the main focus on excitation due to sloshing during the active phase of the engine and the problems of reorientation and boiling during the non-propelled phases. Furthermore, geysering during the restart of the propulsion system and depressurization during different phases like restart or chill-down.

To provide valid test data and benchmarks the following experiments have been conducted:

- Sloshing in a rotating tank with sudden axial acceleration
- Two-dimensional lateral sloshing to study wave breaking
- Axial sloshing due to sudden gravity reduction
- Stratification in a closed container

- Non-isothermal reorientation due to gravity reduction
- Reorientation due to gravity increase to study geysering

Additionally, two sounding rocket experiments were conducted within the European Space Agency (ESA) MAP framework that is related to COMPERE studying similar effects as the aforementioned experiments but during longer periods of reduced gravity. Further details and references can be obtained from Dreyer [47].

On a smaller scale Ludwig and Dreyer [48] analyzed the active pressurization for launcher application by combining analytical studies, numerical simulation and ground experiments in order to investigate the interplay of the used pressurant gas, its mass and temperature on the efficiency of the pressurization system. During the experiment a tank ($0.65\,m$ height and with radius of $0.148\,m$) was filled with Liquid Nitrogen (LN2) as a cryogenic propellant substitute and pressurized with Gaseous Nitrogen (GN2) or Gaseous Helium (GHe) with varying inlet temperatures. The actual active phase of the experiments was started after a defined fill level and stratification was reached due to the boil-off of LN2. After feed-line chill-down the outlet valve of the tank was closed and the active pressurization started until the final pressure value was reached. A relaxation phase took place, and the experiment was concluded by the reopening of the tank outlet. Temperature and pressure were recorded.

For the numerical simulation the commercially available Flow-3D CFD was utilized and good comparison to the experiments was reported. An analytical approach to the pressure development in the tank during active pressurization was proposed and showed good agreement with the experiments. A simulation of the tank pressure development with Flow-3D yielded a too low final tank pressure. More details can be found in Ludwig [49]. A major conclusion of the investigation was that the highest pressurant gas temperature leads to the lowest required pressurant gas mass (with gas lines chilled).

A more technical focused suborbital experiment was performed during the TEXUS 48 sounding rocket flight by Behruzi et al. [50]. Two experimental modules deal with the management of cryogenic LN2 in order to validate PMD concepts that are used in upper stages under μg conditions. Work was focused on draining, refilling, heating and depressurization. The tested PMD consists of a refillable reservoir on a half dome shape attached to the tank bottom and baffles inside to trap liquid for the restart of the engine. During the flight a LOX and LH2 PMD experiment was performed with scale models of

actual management devices or simplified versions to improve observations. The experiment showed that the PMD can handle all flight phases of the TEXUS 48 flight, improved the understanding of the analytical and numerical predications and allowed insight into the PMD performance during ballistic flight phases.

Additional work has been performed by Behruzi and Michaelis [51] and Behruzi et al. [52] in order to understand the behavior of cryogenic propellants in upper stage tanks. Efforts are made to investigate the location of the fluid in actual flight hardware like the Ariane 5 ESC-A upper stage by comparing in-flight sensor data with FLOW-3D simulation and also investigate temperature and pressure data at sensor locations. In Behruzi et al. [52] this kind of sloshing analysis was coupled with in-house tools to perform a closed loop analysis considering the storage tank and the RCS of an upper stage. Later the ESATAN thermal modeling software suite was utilized to also shed light on the temperature development of the tank structure and the propellant.

Developing the aforementioned works further Konopka et al. [33] utilized numerical simulations and experiments performed with the Airbus Defence & Space cryogenic tank demonstrator at the Cryolab of DLR Bremen. LN2 was used to investigate first mode sloshing, stratification of wall and liquid temperature as well as filling and draining. Finally, pressure history was investigated during first mode sloshing. Those experiments were then compared to numerical codes utilized by the authors: Flow-3D, the DLR THETA code and the Airbus Defence & Space in-house ullage pressure solver based on van Foreest [53], [54] and [55]. This code is a 1-D solver considering the energy equation in the liquid phase, an ideal gas and mass exchange at the free interface via the Hertz-Knudsen equation. A main outcome of the work was the influence of the turbulence during the experiment. In addition, the question whether to consider it in the simulations was verified.

A relatively new experiment is KOALA, which was performed by ArianeGroup to investigate stratification and pressure development in cryogenic fluids. These experiments will be further discussed in chapter 6.

3 Governing Equations

3.1 *Isothermal Theory*

The two-phase flow implementation in the DLR TAU code is based on a VOF approach. This approach is not tracking the sharp interface position but the ratio of the volume V of a fluid k in a cell to the entire volume of the control volume:

$$\alpha_k = \frac{V_{cell}^k}{V_{cell}} \tag{9}$$

Thus, the VOF value defines the fraction of fluid k in the considered cell by:

$$\alpha_k = \begin{cases} 1 & \text{inside fluid k} \\ 0 < \alpha_k < 1 & \text{at fluid interface} \\ 0 & \text{outside fluid k} \end{cases} \tag{10}$$

The VOF value is advected via a dedicated scalar transport equation:

$$\frac{\partial \alpha_k}{\partial t} + \nabla \left(\alpha_k \boldsymbol{u} \right) = 0 \tag{11}$$

The total density ρ in a cell is calculated by summation of the products of partial densities of the fluid and the VOF value:

$$\rho = \alpha_k \rho_1 + \left(1 - \alpha_k \right) \rho_0 \tag{12}$$

With ρ_0 an ρ_1 describing the densities of the different phases. The continuity equation in the source free case is given by

$$\frac{\partial \rho}{\partial t} + \left(\nabla \cdot \rho \boldsymbol{u} \right) = 0 \tag{13}$$

With the incompressible condition stating the velocity field is divergence free within the fluids and at the interface

$$\nabla \cdot \boldsymbol{u} = 0 \tag{14}$$

For the isothermal case this source free velocity field leads to a source free scalar transport equation for the VOF value. Equation (13) is solved in a semi-implicit way, which is important for the calculations of the weighting factors to the implemented CICSAM method, which ensures a smooth switch between different differencing methods to prevent non-physical deformation of the interface. More detailed information about the implementation can be found in Ubbink [56], Gauer et al. [57], Gauer and Hannemann [58], Gauer et al. [59], and Gauer [60]. The incompressible Navier-Stokes equation is implemented in the following form:

$$\begin{aligned} &\frac{\partial (\rho \boldsymbol{u})}{\partial t} + \nabla \cdot (\rho \boldsymbol{u}\boldsymbol{u}) = \\ &- \nabla \boldsymbol{p} + \nabla \boldsymbol{\tau} + \rho \boldsymbol{g} + \boldsymbol{F}_{CSF}\,, \end{aligned} \tag{15}$$

where p is the pressure, the term $\nabla \boldsymbol{\tau}$ is the viscous force contribution, and the vector $\boldsymbol{g}$ is the gravitational acceleration vector. It is possible to consider time-dependent acceleration terms via the gravitational acceleration vector in all spatial directions in the DLR TAU code. For this purpose acceleration time histories of the three spatial direction can be specified where values in between two data points are interpolated by using an Akima interpolation (see Hurst [61]). Finally, $\boldsymbol{F}_{CSF}$ is the force vector describing the surface tension force via the Continuum Surface Force (CSF) approach, Brackbill et al. [62].

$$F_{CSF} = \sigma \kappa \nabla \alpha \tag{16}$$

Within the CSF approach the interfacial surface tension σ, is converted into a volume force, which is then applied to the Navier-Stokes equation Gauer et al. [57](see equation (15)). This force depends on the curvature κ and the gradient of the VOF value $\nabla \alpha$. Further details are provided in section 4.2.3. The already mentioned viscous force contri-

bution, represented by the term $\nabla\boldsymbol{\tau}$ with the viscous stress tensor

$$\boldsymbol{\tau} = \mu\left[2\boldsymbol{S} - \frac{2}{3}\boldsymbol{\delta}\nabla\cdot\boldsymbol{u}\right] \tag{17}$$

and the strain rate tensor $\boldsymbol{S}$ is defined as

$$\boldsymbol{S} = \frac{1}{2}\left(\nabla\boldsymbol{u} + (\nabla\boldsymbol{u})^T\right) \tag{18}$$

with μ being the dynamic viscosity calculated in the same manner as the density in equation (12) since the VOF value is volume based:

$$\mu = \alpha_k\mu_1 + (1-\alpha_k)\,\mu_0\,. \tag{19}$$

3.2 *Non-Isothermal Theory without Source Terms*

The energy equation is introduced, as described for example by Hase [17], using the temperature formulation:

$$\frac{\partial\left(\rho c_p T\right)}{\partial t} + \nabla\left(\rho c_p \boldsymbol{u} T\right) = \nabla\lambda T\,, \tag{20}$$

where T is the temperature of the fluid, c_p the heat capacity and λ the heat conductivity; λ is calculated in a similar manner as the density and the dynamic viscosity by

$$\lambda = \alpha_k\lambda_1 + (1-\alpha_k)\,\lambda_0\,. \tag{21}$$

But as has been stated by Patankar [63] it is important that the thermal conductivity should be implemented as a harmonic interpolation instead of a linear one, when a heat flux is applied normal to the interface between two phases. For a general three-dimensional case the following model is assumed:

$$\lambda = \frac{\lambda_0 \lambda_1}{\alpha_k \lambda_1 + (1 - \alpha_k)\, \lambda_0}\,. \tag{22}$$

Further details can be found in a later chapter. The heat capacity is given by Wohak [23]

$$c_p = c_{p_0} \frac{\alpha_k \rho_0}{\rho} + c_{p_1} \frac{(1 - \alpha_k)\, \rho_1}{\rho} \tag{23}$$

Buoyancy forces are modelled via the Boussinesq approximation. Within this approach the density is calculated as a function of the temperature either via a linear approximation using the thermal expansion coefficient β and the reference temperature T_{ref} (equation (24)) or the ideal gas law with the specific gas constant R (equation (25)).

$$\rho = \rho_{ref}(1 - \beta\,(T - T_{ref})) \tag{24}$$

$$\rho = \frac{p}{RT} \tag{25}$$

These terms allow a convective flow within each fluid in the two-phase implementation. The Fourier law on the right-hand side of equation (20) describes the conduction of heat.

3.3 *Non-Isothermal Theory with Source Terms*

Furthermore, an approach to implement phase change, in particular evaporation and condensation, in a two-phase system was performed. This was accomplished by applying a suitable model for both, VOF and the finite volume approach. The implementation of a phase change model was performed to be able to simulate evaporation and condensation in two-phase flows. To achieve this, equation (14) is expanded by a source term resulting in a velocity field that is not source free any longer

$$\nabla \boldsymbol{u} = -\dot{m}_{pch} \left(\frac{1}{\rho_1} - \frac{1}{\rho_0} \right) \tag{26}$$

This source term depends on the phase change mass flux $\dot{m}_{pch}$ and the density difference of the involved fluids making the velocity divergence dependent on the mass-flux difference during phase change. A suitable model to calculate the mass transfer during phase change has to be implemented. Where a Hertz-Knudson model is conceivable, among others. For a single fluid, two-phase system the VOF transport equation also has to be modified with a source term as follows

$$\frac{\partial \alpha_k}{\partial t} + \nabla \left(\alpha_k \boldsymbol{u} \right) = \frac{\dot{m}_{pch}}{\rho_0} \tag{27}$$

Finally, the energy equation has to be modified by a source term $h_v \cdot \dot{m}_{pch}$ to consider the energy transfer by the phase change enthalpy h_v occurring during phase change. Further information can for example be found in Hase [17], Wohak [23] or Schlottke [30].

The conservation of mass is an important feature of two-phase codes and the density change over time has to be considered:

$$\rho \nabla \cdot \vec{u} = \dot{\rho} \tag{28}$$

Where $\dot{\rho}$ is the core of every phase change model and needs careful consideration. Furthermore, the energy equation 20 has to be modified with source term to determine the impact of phase change on the energy and temperature field:

$$\frac{\partial \left(\rho c_p T \right)}{\partial t} + \nabla \left(\rho c_p \boldsymbol{u} T \right) = \nabla \lambda T \; + \dot{h} \tag{29}$$

Further details on the calculation of $\dot{h}$ can be found in chapter 4.3.1.

4 Numerical Modeling

4.1 *The DLR TAU Code*

The DLR THETA code is the incompressible extension of the compressible DLR TAU code that is used in a wide area of usages ranging from sub- and transonic applications for commercial transport aircraft to reacting flows in rocket combustion chambers to external flows around orbital launch systems and flow – engine exhaust interactions.

The DLR THETA code is used for the incompressible flow regime. The solver is used in wind turbine engineering, cabin flow studies and all sorts of internal flow computations. Chemical reacting flows and acoustics are also other fields of applications for the THETA code. Last but not least, THETA can be used to simulate two-phase flows including a variety of effects like surface tension, static contact angle, three dimensional time-varying accelerations and rotational motions as well as evaporation and condensation at the two-phase interface.

The code uses a finite-volume approach to solve the incompressible Navier-Stokes equation by utilizing Semi-Implicit Method for Pressure Linked Equations (SIMPLE) or projection methods to couple the pressure with the velocity equation. Details will be discussed in section 4.2 to provide an overview of the procedure to the reader. The implicit discretization scheme yields to a system of linear equations, that are solved with various Krylov methods. The mentioned pressure correction is computed with a Flexible Generalized Minimal Residual Method (FGMRES) solver that is preconditioned with a geometrical multi-grid method. THETA uses the data structure, libraries and utilities of the DLR TAU code to solve complex flow fields on hybrid, unstructured grids that can be obtained by different measures and that are built in the Network Common Data Format (NetCDF). Special applications like grid movement, deformation and overlap can be handled by the code. A variety of models are supported for example a range of turbulence models as well as models for transition, mixing, temperature effects, porous media and two-phase flow.

4.2 The DLR Theta Code for Two-Phase Flows

4.2.1 The Volume of Fluid Method

The original two-phase implementation was introduced by Gauer [60] and utilizes a transport equation for the VOF variable and the CICSAM method to advance the interface and maintain a sharp interface during motion.

The transport is either limited by the CFL Number (CFL) constraint, which was investigated by Gauer [60] and turned out to be favorable at $c = 0.2$. In cases where a constant time step is required (in cases when there is no or only marginal motion within the fluid) there are two limiting factors. On the one hand, surface tensions limits the advection of the interface by reducing stability if the time step is too large. On the other hand, heat conduction is a driver to limit time steps even further depending on the thermal properties of the considered fluid.

$$\Delta t = MIN\left(c\frac{\Delta x}{u_{max}}, \sqrt{\frac{\rho_0 \Delta x^3}{2\pi\sigma}}\right) . \tag{30}$$

With this time step limits in mind equation 11 can be discretized by using the divergence free velocity, applying Gauss and substituting the surface integral by a sum over all cell phases as well as an Euler implicit discretization:

$$\frac{\alpha_P^{n+1}}{\Delta t^n} V_P + \sum_{f=1}^{N} \alpha_f^{n+1} \dot{V}_f^* = \frac{\alpha_P^n}{\Delta t^n} V_P \tag{31}$$

The discretized transport equation is then handled by the CICSAM method in order to advance the prescribed VOF distribution.

4.2.2 The CICSAM Method

The main purpose of the CICSAM method is to avoid un-physical smearing and keep a sharp interface despite the numerical errors introduced by discretization schemes. Due to the need to use algebraic schemes to reconstruct the interface because geometric schemes are not applicable in THETA and the fact that THETA native schemes are unable to keep the discontinuity of the interface within a few cells the CICSAM scheme proposed

by Ubbink [56] is used. At its core this method is a smoother switching between downwind and upwind schemes when a strong deviation between the interface normal direction and the direction of motion exists.

In the first step the donor and acceptor VOF values, α_D and α_A, are required as well as the predicted upwind value α_U^*. From those VOF values a normalized donor VOF value $\tilde{\alpha}_D$ is calculated.

$$\tilde{\alpha}_D = \frac{\alpha_D - \alpha_U^*}{\alpha_A - \alpha_U^*} \,. \tag{32}$$

Here a donor (sending cell) is reducing its own amount of VOF value, thus reducing the amount of one phase it has. An acceptor (receiving cell) is a cell getting this amount of VOF value coming from a donor.

Using the upper bound of the Convection Boundness Criterion (CBC) and the lower bound of the Ultimate-Quickest (UQ) schemes, a normalized face value for the VOF value is estimated by a weighted summation of these two schemes:

$$\tilde{\alpha}_f = \gamma_f \tilde{\alpha}_{f_{CBC}} + (1 - \gamma_f)\tilde{\alpha}_{f_{UQ}} \,. \tag{33}$$

The weighting factor γ_f is determined depending on the angle θ_f between the connection of donor and acceptor and the gradient direction of VOF:

$$\gamma_f = \min\left\{ k\frac{\cos(2\theta_f) + 1}{2}, 1 \right\} \tag{34}$$

Where $\cos(2\theta_f)$, the angle between the vector normal to the interface and the connection vector $\boldsymbol{l}$ of the donor and acceptor cell, can be calculated utilizing

$$\theta_f = \arccos\left(\frac{|\nabla\alpha_D \cdot \boldsymbol{l}|}{|\nabla\alpha_D| \cdot |\boldsymbol{l}|} \right) \,. \tag{35}$$

The CICSAM weighting factor is now computed from a part of the normalized face value and a corrector step due to un-physical VOF values (bigger 1 and below 0) that can

occur from badly shaped grid cells.

$$\beta_f^{'} = \beta_f - \beta_f^* \tag{36}$$

With the normal weighting factor β_f given by $\beta_f = \frac{\tilde{\alpha}_f - \tilde{\alpha}_D}{1-\tilde{\alpha}_D}$ and the corrector step by

$$\beta_f^* = \begin{cases} \min\left\{\frac{E(2+c-2c\beta_f)}{2c(\pm\Delta\alpha^* - E)}, \beta_f\right\} & \text{when} \pm\Delta\alpha^* > E \\ 0 & \text{when } \pm\Delta\alpha^* \leq E \end{cases} \tag{37}$$

Where Δ_α^* is the difference between the mean values of the acceptor and donor cells between the actual and the next time step. Finally, the needed face value of the VOF variable can be estimated with

$$\alpha_f = (1 - \beta_f^{'})\alpha_D + \beta_f^{'}\alpha_a \,. \tag{38}$$

The usage of the corrected weighting factor β_f^* in equation (38) guarantees the VOF value remains in its bounds between $0 < \alpha_k < 1$ and un-physical values are prevented and adjusted in a meaningful manner.

4.2.3 Surface Tension and Wall Adhesion

The correct modeling of the interface is linked to a well-defined scheme for the calculation of the surface tension force that is acting onto the interface and influences the momentum equation through a volume force $\mathbf{F}_{CSF}$ as has been stated in equation (15). The resulting pressure drop across the interface is depending on the surface tension σ and the curvature of the interface and can be estimated by the simple statement $\Delta p = \sigma\kappa$. The estimation of the curvature requires a more thorough approach and needs to consider the contact phenomenon at the wall.

At a free surface, that is not bounded by any contact surfaces, the curvature κ is estimated by the negative divergence of the local unit normal vector of the fluid interface

$$\kappa = -(\nabla \cdot \hat{\mathbf{n}})\,. \tag{39}$$

The normal vector is defined as the gradient of the smoothed VOF value $\mathbf{n} = \nabla\hat{\alpha}$. Where the gradient can be expressed as a summation over all control volumes by

$$\nabla\hat{\alpha}_P = \sum_{f=1}^{N_f} \hat{\alpha}_f \mathbf{A}_f\,. \tag{40}$$

With the help of the central differencing scheme the face value of the VOF value $\hat{\alpha}_f$ is calculated and the resulting gradient and its absolute value are used to estimate $\hat{\mathbf{n}}$ via:

$$\hat{\mathbf{n}} = \frac{\mathbf{n}}{|\mathbf{n}|} = \frac{\nabla\hat{\alpha}_f}{|\nabla\hat{\alpha}_f|}\,. \tag{41}$$

At wall contact points, where solid, liquid and gaseous phase are in contact, the liquid phase will tend to coat the solid phase depending on the static contact angle Θ, which is a characteristic value of the considered fluid. This angle is implemented via $\hat{\mathbf{n}}$ at the wall:

$$\hat{\mathbf{n}} = \hat{\mathbf{n}}_W \cdot \cos\theta + \hat{\mathbf{n}}_t \cdot sin\theta\,. \tag{42}$$

Where $\hat{\mathbf{n}}_W$ donates the unit normal vector of the wall and $\hat{\mathbf{n}}_t$ the tangential component of the normalized unit normal vector, which is calculated via the tangential part of the corresponding interface gradient $\nabla\hat{\alpha}_{P,t}$:

$$\hat{\mathbf{n}}_\mathbf{t} = \frac{\nabla\hat{\alpha}_{P,t}}{|\nabla\hat{\alpha}_{P,t}|}\,. \tag{43}$$

Depending whether the curvature needs to be calculated at an inner control volume or a wall, equation (41) or equation (42) will be considered, respectively. With the now known curvature of the interface, a volume force can be introduced that will consider the influence of a free interface in the flow. This CSF approach was first presented by Brackbill

et al. [62] and was introduced into THETA by Gauer et al. [57]:

$$\mathbf{F_{CSF}} = \sigma\kappa\nabla\alpha_P V_P \frac{\rho_P}{\hat{\rho}} \,. \tag{44}$$

Where the VOF gradient is estimated similar to equation (40), volume V_P and density ρ_P of the corresponding control volume P are used and the average density of both fluids $\hat{\rho} = \frac{1}{2}(\rho_0 + \rho_1)$ is required as well.

Further information regarding this implementation and an extensive validation can be found in Gauer [60]. The implementation of a dynamic contact angle, an angle that depends on the velocity of the contact line, is not used in this work but was investigated by Meyer [45].

4.3 *Source Term Estimation*

This section will provide some insight into how the mass source term of section 3.3 is estimated and in a second subsection the estimation of the needed heat flow coming from the fluid is discussed.

4.3.1 *Smoothing of Mass Source Distribution*

For two phase flows that consider evaporation or condensation the velocity field is not divergence free anymore. Thus, both processes represent sources and sinks, respectively. This is expressed in (28). In the following we will discuss how the term $\dot{\rho}$ is estimated.

One starts with the assumption that the interface is at saturation temperature over its complete extension. This is because dispersion forces of the thermodynamic equilibrium and curvature of the interface on a macroscopic scale can be assumed to be comparably small at bulk pressure p_0:

$$T_{int} = T_{sat}(p_0) \tag{45}$$

The energy balance over the interface then yields an estimation of the mass flux due to phase change. This flow depends on the heat coming from the liquid side of the interface as well as the heat from the vapor side, thus:

$$m_{pch} = \frac{q_1 + q_0}{L} \,. \tag{46}$$

Fourier's law is again applied for the separate heat fluxes, using the temperature gradient in the liquid and vapor phase, respectively:

$$q_0 = \lambda_0 \nabla_{int_0} T \,, \tag{47}$$

and

$$q_1 = \lambda_1 \nabla_{int_1} T \,. \tag{48}$$

Eventually, one gets the phase change mass flow of one computational cell by multiplying the mass flux and the inter-facial area within this cell

$$\dot{M}_{PCH} = m_{PCH} \cdot S_{int} \,. \tag{49}$$

As introduced by Hardt and Wondra [22] the VOF gradient contains information of the interfacial area within an enclosed region. For three dimensional spaces the volume integral yields the interface area whereas in two dimensions the area integral gives the interface length

$$\int_V |\nabla \alpha| \, \mathrm{d}V = \int_S \mathrm{d}S \,. \tag{50}$$

Now one has to model the vanishing of liquid due to evaporation and the re-appearance of the vapor to satisfy mass conservation. This will be done by a method introduced by Hardt and Wondra [22] that is used by a wide range of authors e.g. Kunkelmann [6] and Sato and Ničeno [7]. This approach basically shifts the loss of fluid and the corresponding reappearance of fluid in a different phase away from the interfacial region in the corresponding phase region, which contains the pure fluid. For example, the loss of

liquid due to evaporation is completely shifted in the liquid bulk and the appearance of its vapor is done in the gaseous bulk on the other side of the interface. The initial mass source distribution is depicted as ϕ_0 and is concentrated at the interface region where the VOF is below 1 and above 0

$$\varphi_0 = \frac{\dot{M}_{PCH}}{V_{cell}} \tag{51}$$

This sharp distribution is smoothed by the solution of an inhomogeneous Helmholtz equation resulting in the smoothed-out solution ϕ

$$\nabla^2 \varphi = \frac{1}{\Delta t D} (\varphi - \varphi_0) \tag{52}$$

This equation can also be understood as a simple diffusion equation. Utilizing this smoothed distribution, one will get a new, smeared field of the density source term

$$\dot{\rho} = [N_0(1-\alpha)H - N_1 \alpha H] \cdot \varphi \,. \tag{53}$$

H donates the Heaviside function and N are normalization factors for liquid and vapor, respectively. In order to conserve the global mass, the normalization factors are calculated with

$$\iiint_V \varphi_0 \,\mathrm{d}V = N_0 \iiint_V (1-\alpha) \cdot H\varphi \,\mathrm{d}V \tag{54}$$

$$\iiint_V \varphi_0 \,\mathrm{d}V = N_1 \iiint_V \alpha \cdot H\varphi \,\mathrm{d}V \tag{55}$$

With these considerations the final density source term can be estimated

$$\dot{m}_{pch} = \dot{\rho} \left(\frac{H}{\rho_0} - \frac{H}{\rho_1} \right) . \tag{56}$$

Additionally, it is necessary to provide a source term for the energy equation to account for the production and disappearance of fluid within the bulk regions of vapor and liquid

$$\dot{q}_{smo} = [N_0(1-\alpha)Hc_{p_0} - N_1\alpha Hc_{p_1}] \cdot \varphi T . \tag{57}$$

The process of smoothing is illustrated in figure 6.

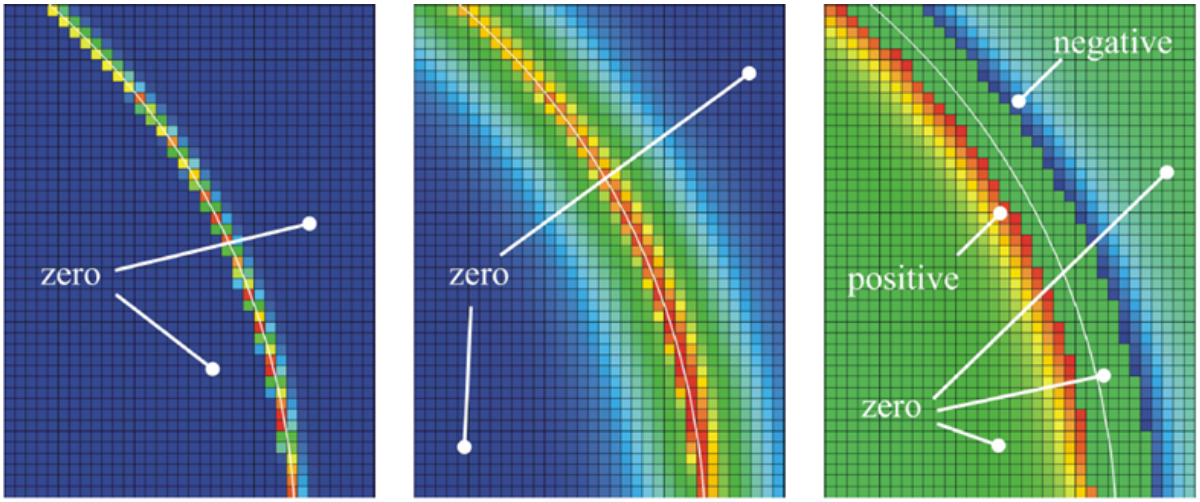

Figure 6: The smoothing process in the case of a curved interface region ($\alpha = 0.5$-contour presented by white line). Left: phase change source term at the interface. Center: smearing of the source term around the interface. Right: scaling of the source term out of the interface region. By Kunkelmann [6] is licensed under CC BY-NC-ND 2.5 .

These aforementioned source terms have to be integrated into the current state of the code that was described in section 4. For the VOF equation (9) only the smoothed source term that is located in the liquid region, where $\alpha > 0$, has to be considered since a VOF value cannot be smaller than 0 by definition of equation (10). This is done by the multiplication of the smoothed source term with the VOF value

$$\frac{\partial \alpha_k}{\partial t} + \nabla \left(\alpha_k \boldsymbol{u} \right) = \alpha \frac{\dot{m}_{pch}}{\rho_0} \,. \tag{58}$$

For the mass conservation equation, the complete smoothed source term is used to resemble the disappearance of fluid and appearance of the corresponding phase change fluid. This is achieved by putting equation (56) into equation (26).

The enthalpy source $\dot{h}$ for equation (29) is divided into two parts. The first part includes the correction for the distributed mass source of equation (57) and will have an effect outside but on both sides of the interface. Whereas the second part of $\dot{h}$ is the source term due the latent heat L of the evaporation or condensation process that is mainly dependent on $\dot{m}_{pch}$

$$\dot{h}_{pch} = \dot{m}_{pch} \cdot L \,. \tag{59}$$

Thus, yielding to a total source term for the temperature equation (equation (29))

$$\dot{h} = \dot{h}_{pch} + \dot{q}_{smo} \,. \tag{60}$$

This step concludes the implementation of the source terms into the governing equations.

4.3.2 *Estimation of Fluid Heat Flux*

As described in chapter 4.3.1 the defining quantity for the amount of phase change that is occurring is defined by the heat fluxes into the interface coming from both, the liquid and gaseous side. Equation (46) expresses this fact.

It is now the task to express this heat flux in a meaningful way since standard differencing schemes are of no use, since the interface position within a computational volume is subject to change over time. Therefore, one has to find other ways to express $\nabla_{int_0} T$. Since we assume saturation temperature T_{sat} at the interface the temperature gradient of equation (47) can be expressed for the phase k in the following way:

$$\nabla_{int_0} T = \frac{T_k - T_{sat}}{d_{int}} \,. \tag{61}$$

In order to estimate this gradient two values are needed: a temperature in the fluid T_k and the distance d_{int} from the interface to the position where T_k is estimated. Both are evaluated at every time step, taking into account the changing position of the interface and the changing temperatures. Starting with the distance d_{int} it is necessary to get the exact location of the interface. This can be done for a general interface

$$\vec{d_{int}} = \vec{n} \cdot \vec{x} - \vec{n} \cdot \vec{x_{int}} \,. \tag{62}$$

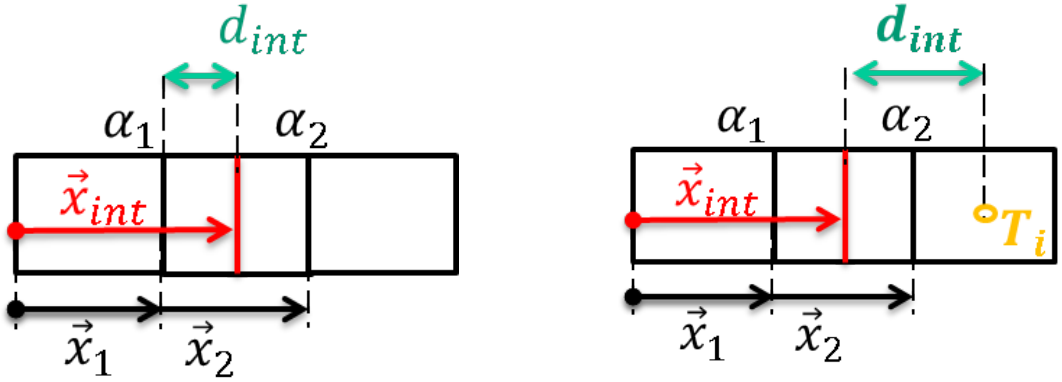

(a) Estimation of interface using the gradient of the VOF value and the corresponding location of the mesh point.

(b) Interpolating the temperature T_i at a given distance d_{int} to the interface.

Figure 7: Different estimations of distance to interface.

The corresponding situation is depicted in figure 7a. The interface position $\vec{x_{int}}$ is estimated with a simple linear function that is evaluated at $\alpha = 0.5$ in all spatial directions

$$\vec{x}_{int} = \vec{x_1} + (\vec{x_2} - \vec{x_1}) \frac{0.5 - \alpha_1}{\alpha_2 - \alpha_1} \,. \tag{63}$$

In order to avoid an oscillating d_{int} it was decided to keep it constant and estimate the temperature at a fixed distance from the interface. This situation is shown in figure 7b.

Now the difficulty is to interpolate the fluid temperature at the given distance. A tri-linear interpolation is used to evaluate the new, unknown temperature from known surrounding values. Weights are calculated to incorporate the position of the point within a volume as is shown in figure 8.

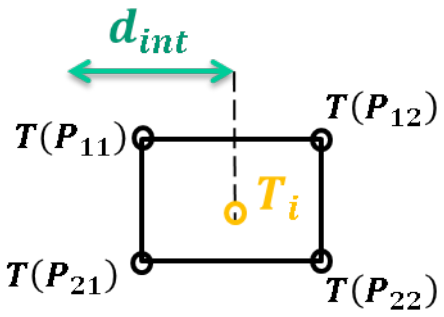

Figure 8: Interpolation of the fluid temperature in a volume.

Those weights are used to get the temperature T_k at the chosen distance to the interface using the temperature $T(P_{ij})$ at the mesh points P_{ij} of the dual grid.

$$\begin{aligned} T_k \approx & w_{11} \cdot T(P_{12}) + w_{12} \cdot T(P_{11}) \\ & + w_{21} \cdot T(P_{21}) + w_{22} \cdot T(P_{22}) \,. \end{aligned} \tag{64}$$

With the estimation of these two values the heat flux of a fluid k towards the interface can be determined and is subsequently used to solve equation (46) and is the basic value that characterizes the amount of fluid that changes phase and will be further treated according to chapter 4.3.1.

4.3.3 *Boussinesq approximation*

As already described in section 3.2 the THETA code needs the ability to calculate temperature depent density variations. This is achieved by using the already mentioned Boussinesq approximation and was already available in the THETA code for single fluid systems. It was now required to expand it to being able to numerically deal with a two-phase flow where two different fluids are divided by an interface.

The chosen approach to incorporate the different thermal expansion with the different VOF value of the fluid was to first estimate the new temperature dependent density of the partial densities $\rho_0 = f(T)$ and $\rho_1 = f(T)$. The approach used is a user input as one can either use the ideal gas law (equation (25)) or a linear approximation using the expansion coefficient β (equation (24)). After this step the densities are summed as products of the partial, temperature dependent densities and the VOF value similar to equation (12):

$$\rho(T, \alpha) = \alpha_k \rho_1(T) + (1 - \alpha_k)\rho_0(T)\,. \tag{65}$$

The in THETA usable parameters of this expansion are described in Appendix A. The approach was further described and evaluated in Keiderling et al. [64].

5 Validation on Basic Test Cases

5.1 *The Stefan Problem*

The so-called Stefan problem is a basic one-dimensional phase change test case that is used in numerous publications to validate the functionality of CFD codes regarding evaporation or condensation. The case consists of a free-slip tube and is confined by a heated wall on one end and by an outflow on the other end. At the wall end a constant temperature is maintained throughout the simulation and a temperature profile will develop towards an existing interface that separates a vapor region at the wall from a liquid region towards the outflow.

Caused by the heat flow through the vapor the liquid phase will start evaporating due to energy that is transported towards the interface and liquid phase. Both are at saturation temperature and any further increase will cause the transit from the liquid state to the vapor state. As a result, the interface will shift towards the outflow since evaporating liquid causes the production of vapor that results to a volume expansion in the isobaric domain and moves the interface towards the outflow (in case of evaporation, for condensation the interface would move towards the wall).

Both, interface position and temperature distribution, can be determined by analytical solutions as shown by Welch and Wilson [25]:

$$x_{int}(t) = 2 \cdot \chi \sqrt{\kappa_0 t}, \tag{66}$$

$$T(x,t) = T_W + \left(\frac{T_{sat} - T_W}{erf(\chi)} \right) erf \left(\frac{x}{2\sqrt{\kappa_0 t}} \right). \tag{67}$$

Where κ designates the thermal diffusivity that is generally expressed as $\kappa = \lambda/(\rho c_p)$. In the current case it is expressing the transfer of heat to the vapor (identified by the subscript 0), which is the driving factor for the evaporation rate in the Stefan Problem. Only the vapor region contains a linear temperature gradient whereas the liquid retains a zero gradient from the interface towards the end of the domain at the outflow. These relations are visualized in figure 9.

For the analytical solution, a problem specific number has to be derived. χ is the

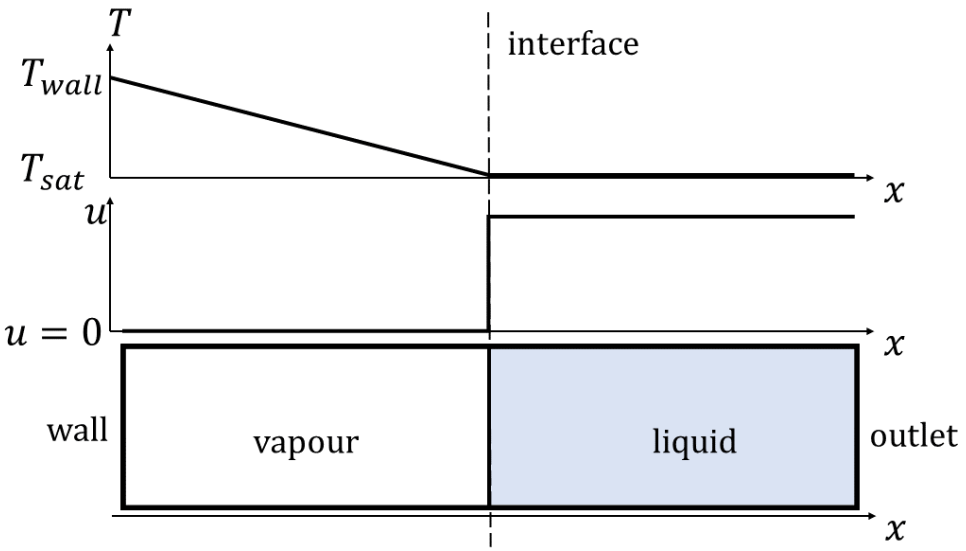

Figure 9: Schematic of the Stefan Problem. After Sato and Ničeno [7].

solution of the transcendental equation:

$$\chi \, exp(\chi^2) erf(\chi) = \frac{c_{p_v}(T_W - T_{sat})}{\sqrt{\pi} L}. \tag{68}$$

This described motion results in a velocity build up in the liquid phase, which is a sharp jump at the interface but remains constant towards the outflow. With the given temperature difference and the corresponding interface position at a given time t it is possible to calculate the temperature gradient $\frac{\partial T}{\partial x}$ and the resulting velocity of the interface:

$$u_{int}(t) = \frac{\lambda_0}{\rho_0 L} \frac{\partial T}{\partial x}. \tag{69}$$

The driving force of the evaporation and the initiated motion is the temperature gradient $\frac{\partial T}{\partial x}$ in the vapor phase, which has to be determined at time t. With the movement of the interface between vapor and liquid towards the outlet (i.e. to the right, see fig-

ure 9) the gradient is becoming flatter, resulting in decreased vapor production and slower progression of the liquid phase.

Table 2 presents the parameters for the liquid and vapor phase of water that were used to perform the validation with the Stefan Problem.

Fluid	Index	ρ	c_p	λ	μ	L	σ	T_{sat}
vapor	0	0.597	2030	0.025	$1.26 \cdot 10^{-5}$	$2.26 \cdot 10^{6}$	0.059	373.15
Liquid	1	958.4	4216	0.679	$2.80 \cdot 10^{-4}$	–	–	–
Units	$[-]$	$\left[\frac{kg}{m^3}\right]$	$\left[\frac{J}{kgK}\right]$	$\left[\frac{W}{mK}\right]$	$\left[\frac{Pa}{s}\right]$	$\left[\frac{J}{kg}\right]$	$\left[\frac{N}{m}\right]$	$[K]$

Table 2: Fluid properties of liquid water and its vapor.

The used numerical parameters are listed in table 3. The selected time step is $t = 5.0 \cdot 10^{-5}\, s$ but a time convergence study in section 5.1.2 will show that the solution is mostly independent of the selected time step range since the surface tension stability is not critical in the presented case with a flat interface and no capillary effect.

Parameter	Value	Units/Dimension
Mesh	structured, 250, 500 and 1000	cell number
Pressure Solver	FGMRES, PFM Multigrid level 3	-
Momentum Solver	BCGS, Jacobi Pre-cond., DS: UDS	-
DS VOF, T	BCGS, Jacobi Pre-cond., DS: UDS	-
DS Time	Euler Implicit	-
Models	ENG_TEMP, MOM_SRC, VOF	-
Ref. Time step	$\Delta t = 5.0 \cdot 10^{-}5$	s
Length in x	$x = 0.1$	m

Table 3: Numerical parameters for the validation test cases.

The results of the simulation are compared to the analytical solution regarding the interface position as stated in equation (66) and are shown in figure 10. A good agreement of the computational simulation with the analytical solution could be reached with errors ranging between just below 3% at simulation start and approximately 0.6% at the end of the process at $t = 0.1\, s$. A commonly used simulation duration was adopted e.g. from [7].

Another important characteristic of a correct solution of the Stefan problem is the slope of the gradient in the vapor phase. This metric shows whether the heat transport and source term in the energy equation is implemented in the right fashion. As shown in figure 11 the agreement between the analytical solution and the simulation is distinctive. Furthermore, the numerical simulation of the Stefan problem is able to predict the slope

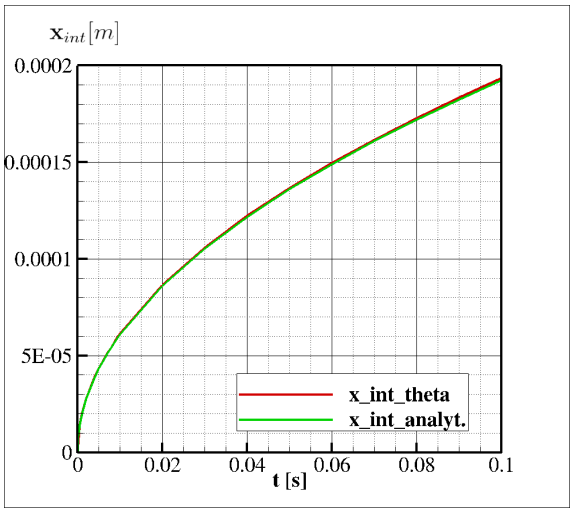

(a) Comparison of interface position from analytical solution and THETA.

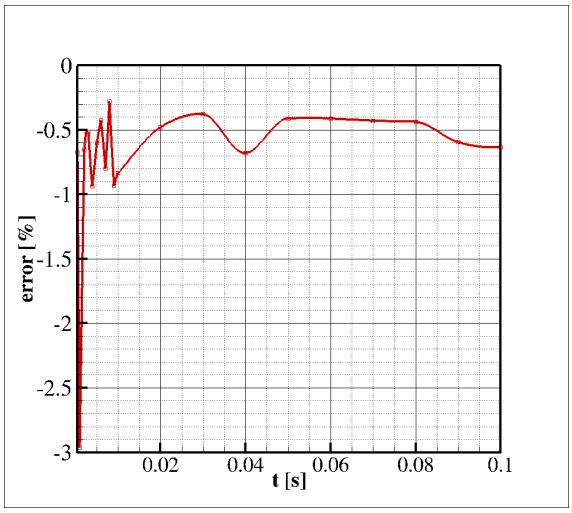

(b) Interface position error of THETA solution of Stefan Problem for the 1000 cell grid.

Figure 10: Interface position of Stefan Problem.

of the gradient at any given time and produces a sharp discontinuity at the interface where the temperature gradient becomes zero.

In figure 12 the mass flux due to evaporations calculated by THETA as of equation (46) is compared to the analytical flux from the above-described theory. Fluctuations due to the numerical formulations are visible and they can also be depicted in the velocity characteristics of figure 13.

Different numerical approaches to include the evaporation mass flux into the pressure equation are shown in figure 14 in order to show the advantage of smoothing and normalization $\dot{m}_{pch}$ as explained in chapter 4.3.1.

The direct inclusion of the phase change source term into the interface region caused a strong offset of the velocity development of the Stefan problem (red curve). Thus, a simple determination of the source term was used, which uses a simple temperature difference at the interface. With this approach the velocity now oscillates around the analytical solution (green graph). In a last step, in this simple approach the difference was corrected to use the more precise temperature gradient approach as presented in section 4.3.2. This resulted in a reduced osculation around the analytical value that is still occurring, but with a much lower peak-to-peak value compared to the two other approaches.

Next the presented implementation is validated with the so-called Sucking-Interface

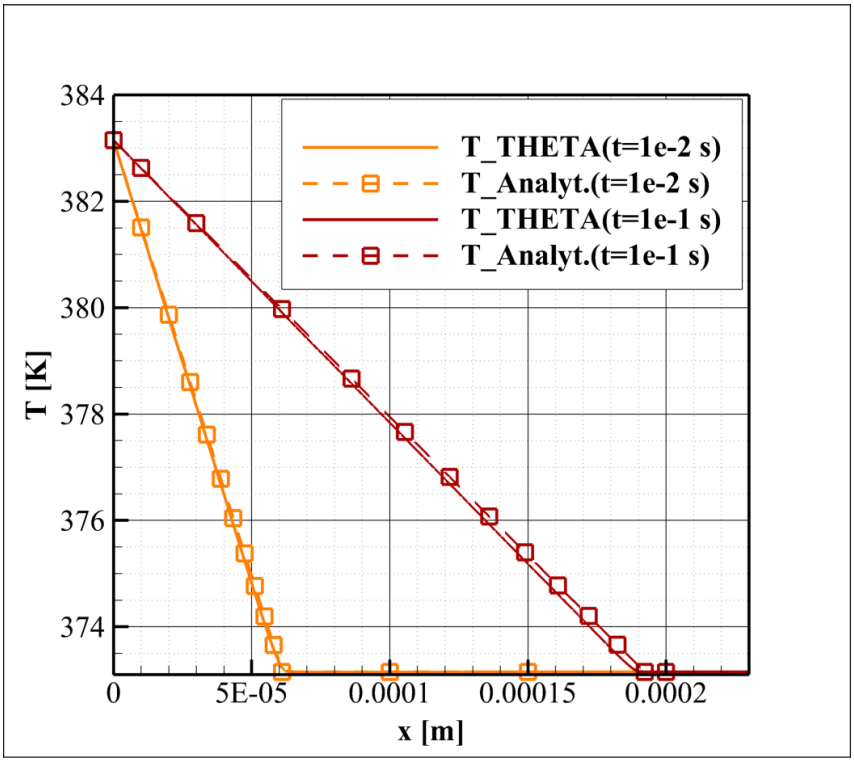

Figure 11: Different temperatures profile at different times of the simulated solution to the Stefan Problem and the solution of the energy equation. The solutions from THETA for $t = 0.01\,s$ (orange line) and for $t = 0.1\,s$ (red line) are compared to the two corresponding analytical solutions at these times (dashed orange and red lines, data points marked with squares).

Problem.

5.1.1 Mesh Convergence Study

To study the convergence of different meshes a study was performed with three grid sizes. As stated in table 3 is length of the channel is $0.1\,m$. The results are summarized in figure 15. Meshes with 200 (blue curve), 500 (green curve) and 1000 (red curve) grid cells were investigated over the simulation time of 0.1 seconds. Compared is the error of the THETA solution for the different grid sizes with respect to the analytical solution presented in section 5.1 as a relative error.

An increased error is visible at the beginning of the solution for the smaller grid sizes. This error decreases with increasing cell numbers of the grid and is about 3% for the

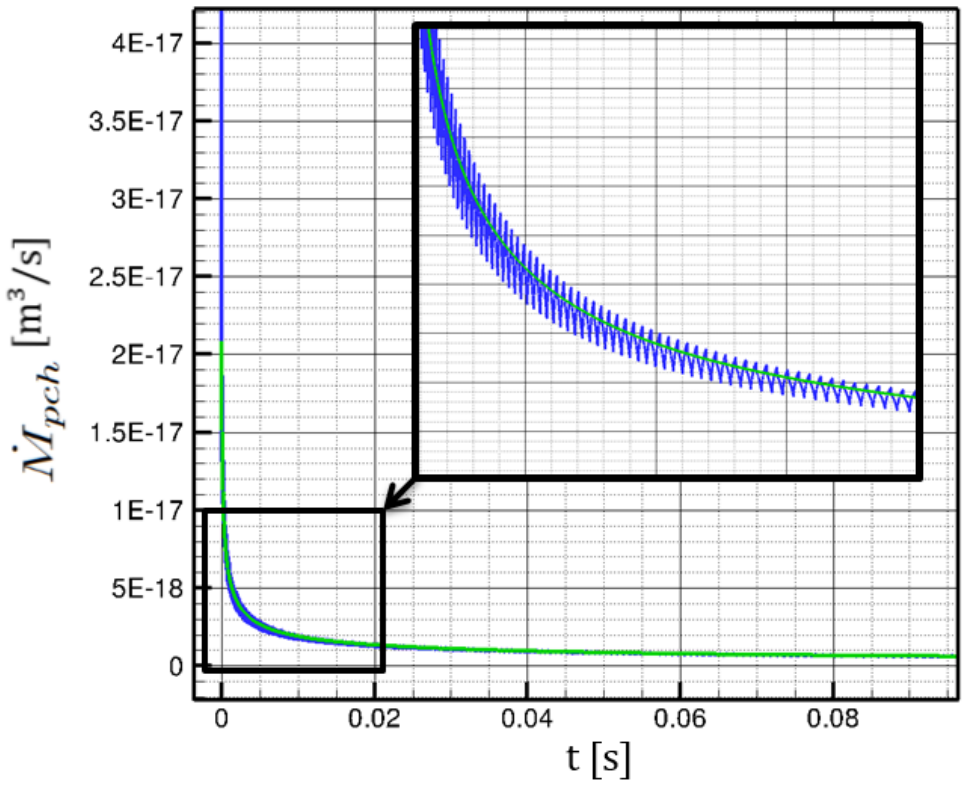

Figure 12: Comparison of phase change mass flux $\dot{M}_{pch}$ of analytical solution (green line) and THETA (blue line).

smallest grid cells. This can be interpreted as an uncertainty level at the initialization of the smeared, unsharp interface (as discussed in section 4.2.2). This error is rapidly decreasing for all meshes sizes, thus indicating that the grid discretization was sufficiently chosen for these simulations.

Here the two meshes with larger grid cells tend to oscillate around the analytical solution, with only the 1000 cell mesh demonstrating a relative smooth progression of the error over time.

5.1.2 Time Convergence Study

Additionally, to the mesh convergence study, the other important discretization axis the time step size was investigated. The results are summarized in figure 16. Time steps with $\Delta t = 1.0 \cdot 10^{-7}\, s$ (blue curve), $\Delta t = 1.0 \cdot 10^{-6}\, s$ (green curve) and $\Delta t = 1.0 \cdot 10^{-5}\, s$

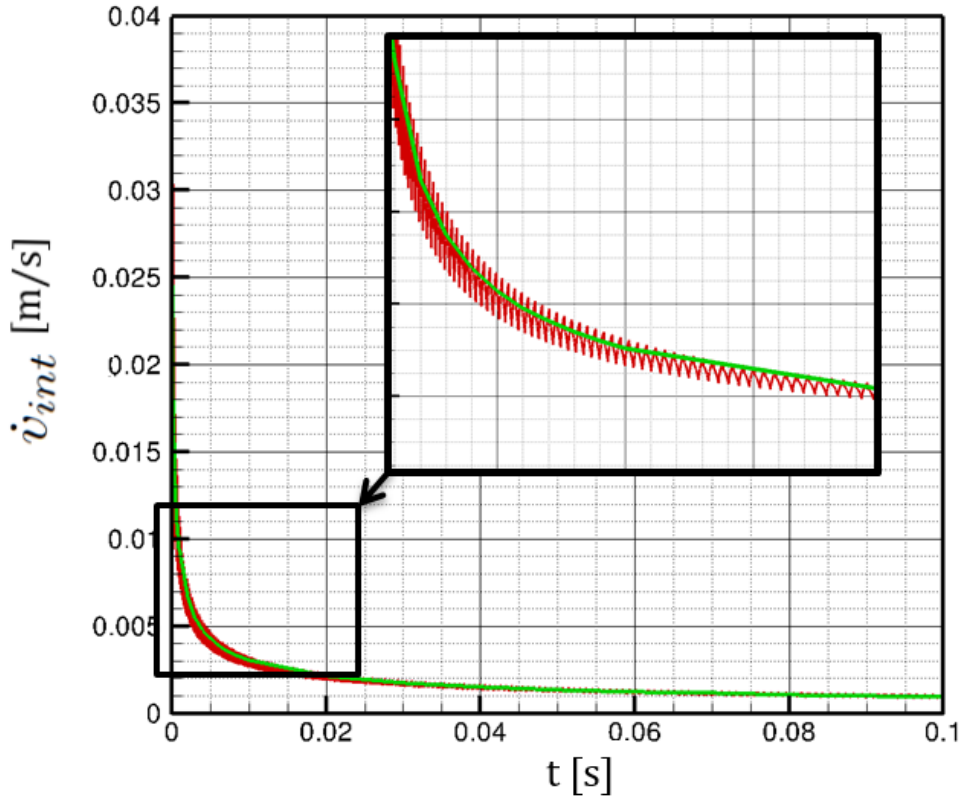

Figure 13: Comparison of interface velocity $\dot{v}_{int}$ of analytical solution (green line) and THETA (red line).

(red curve) were investigated over the simulation time of 0.1 seconds. The error is again a relative error that compares listed time steps to the reference time step of the nominal solution presented in section 5.1 of $\Delta t = 5.0 \cdot 10^{-6}\, s$.

Comparing the reference time step used in section 5.1 the three additional time steps investigated do not yield to dramatically different results in terms of error development of the simulation. The error is oscillating for all time steps investigated between -1.3% and just below 0.5%. Thus, yielding to the conclusion that even a slightly larger time step compared to the reference time step of $\Delta t = 5.0 \cdot 10^{-6}\, s$ (calculated with equation (30)) was not producing large errors.

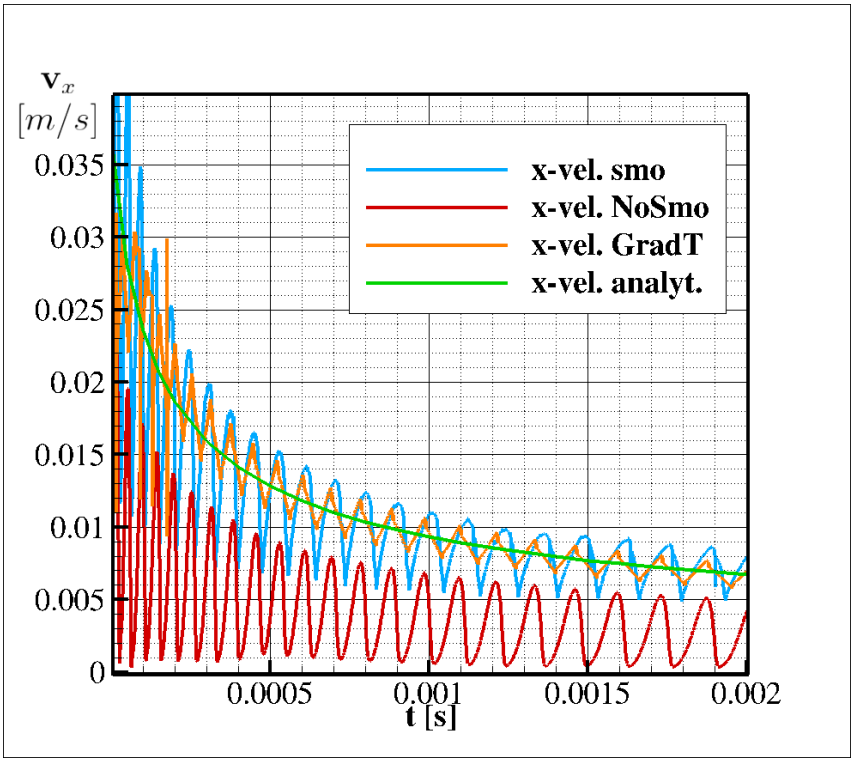

Figure 14: Velocity characteristic of the analytical solution to the Stefan Problem and the solution of the momentum equation. Shown are the analytical velocity in the x-direction (green line), the x-velocity of the THETA solution without smoothing (red line), the x-velocity of the THETA solution with smoothing (blue line) and the x-velocity of the THETA solution with smoothing and calculation of the temperature gradient according to equation (61) (orange line).

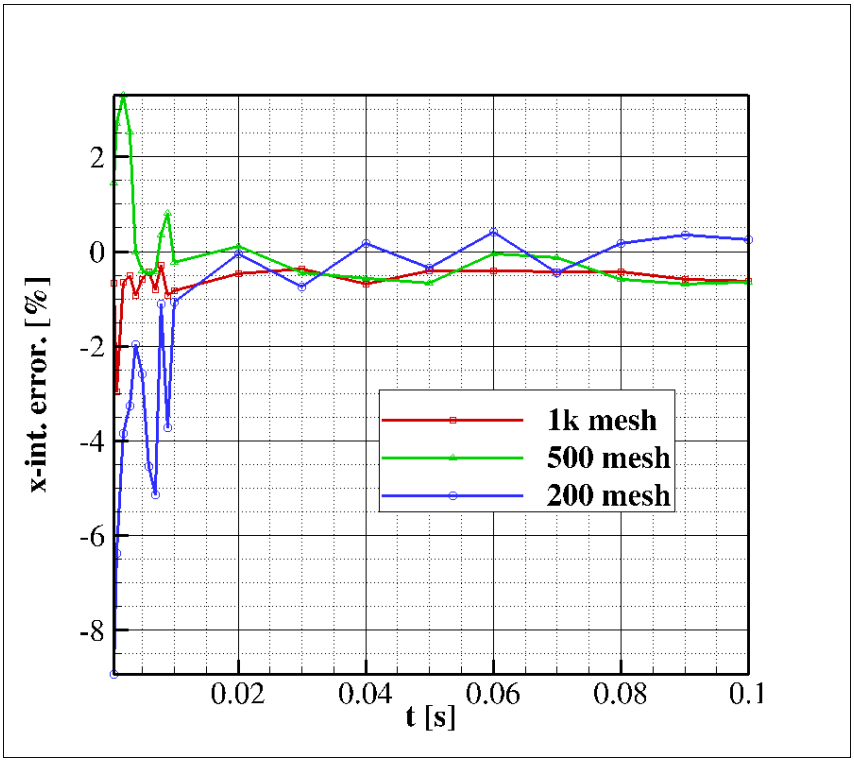

Figure 15: Grid convergence of the Stefan problem with different grid sizes of 200 (blue curve), 500 (green curve) and 1000 (red curve) cells.

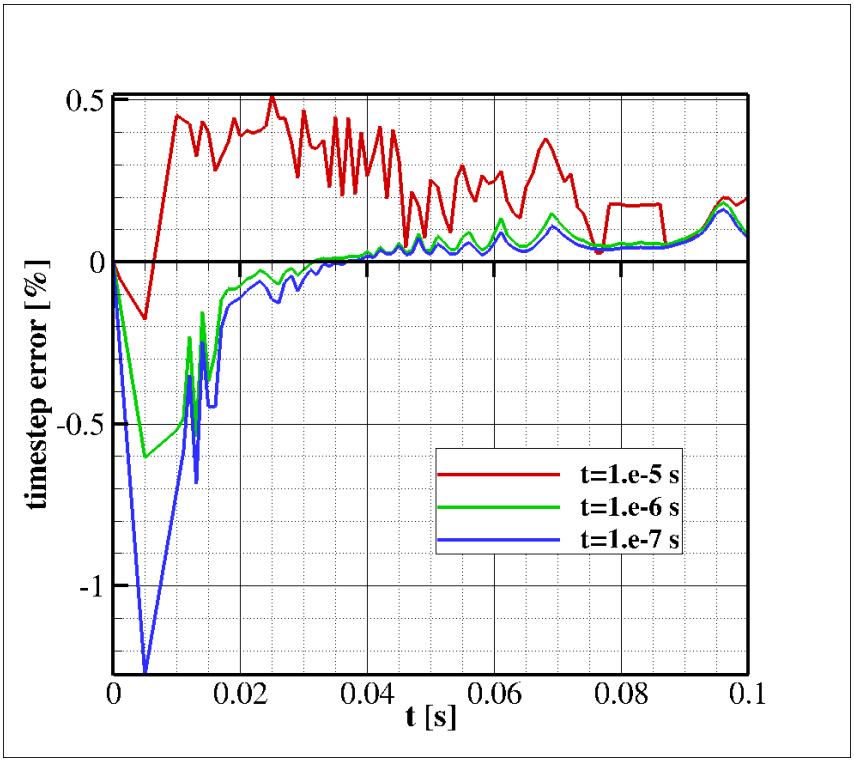

Figure 16: Time convergence of the Stefan problem with different time steps of $\Delta t = 1.0 \cdot 10^{-7}\, s$ (blue curve), $\Delta t = 1.0 \cdot 10^{-6}\, s$ (green curve) and $\Delta t = 1.0 \cdot 10^{-5}\, s$ (red curve).

5.2 *The Sucking-Interface Problem*

Using a similar layout as it was introduced for the Stefan problem in chapter 5.1 the Sucking-Interface problem is distinguished by the temperature in the fluids. In contrary to the Stefan problem, the wall of the Sucking-Interface problem is at saturation temperature T_{sat} just as the vapor phase between the interface and the wall. The driving temperature difference is present in the liquid phase that is superheated, a fixed amount of Kelvin above T_{sat}. A temperature distribution will be present in a thin thermal layer at the interface as it is visualized in figure 17. It will follow the motion of the vapor/liquid separation. This motion is again caused by the expansion of the vapor due to the existing phase change at the interface that adds vapor to the gaseous phase, thus expanding its value when pressure needs to remain constant. This setup is visualized in figure 17.

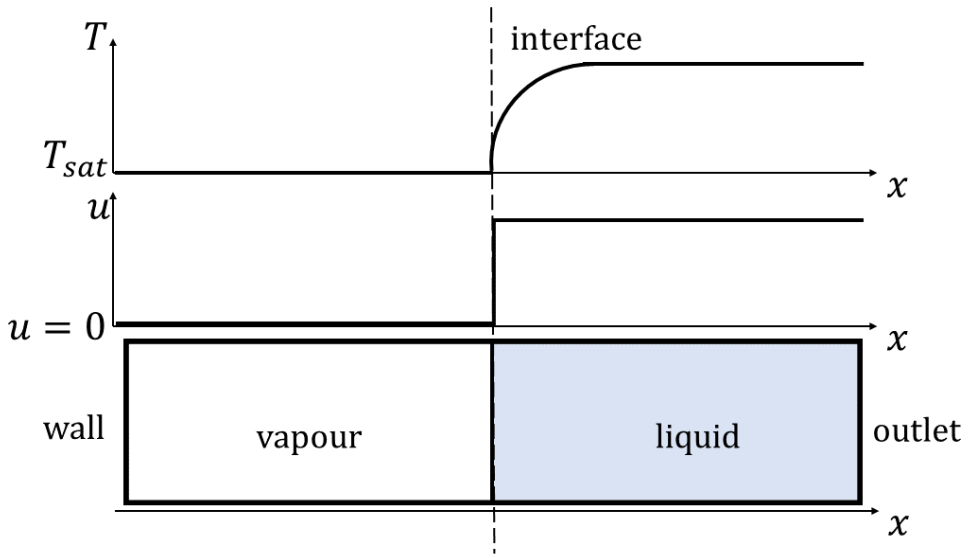

Figure 17: Schematic of the Sucking-Interface Problem. After Sato and Ničeno [7].

Welch and Wilson [25] are describing an analytical solution to this problem, which makes it an excellent and often used choice to validate phase-change codes when the temperature gradient is present in the liquid. This is possible since we use the liquid and the vapor heat fluxes to estimate the amount of phase change as it is described in

equation (46) in section 4.3.1.

At first, the spatial coordinates have to be transformed to locate the interface at the variable $\xi = 0$

$$\xi = x - \int_0^t u_{int}(t)\,\mathrm{d}t\,. \tag{70}$$

Thus, the energy equation for the liquid phase is also transformed into

$$\frac{\partial T}{\partial t} + (u - u_{int})\,\frac{\partial T}{\partial \xi} = \kappa_1 \frac{\partial^2 T}{\partial \xi^2}\,. \tag{71}$$

Where the following boundary conditions are applied

$$\begin{aligned} T(\xi = 0, t) &= T_{sat}\,, \\ T(\xi \to \infty, t) &= T_1\,, \\ T(\xi, t = 0) &= T_1\,. \end{aligned} \tag{72}$$

Where T_1 is the superheated temperature in the liquid phase. At the interface the jump condition for the energy and the mass is

$$\begin{aligned} \rho(u_1 - u_0) \cdot L &= -\lambda \frac{\partial T}{\partial \xi}\bigg|_{\xi=0} \\ -\rho_0 \cdot u_{int} &= \rho(u_{int} - u_1) \end{aligned} \tag{73}$$

Furthermore, one defines the following constants

$$B = \frac{\kappa}{C\beta}, \quad \beta = \frac{\rho_0}{\rho_1}, \quad C = \frac{\lambda}{\rho_0 L} \tag{74}$$

and by using the mass jump condition of equation (73) one gets a simplified energy equation for the superheated liquid

$$\frac{\partial T}{\partial t} + \beta u_{int} \frac{\partial T}{\partial \xi} = \kappa_1 \frac{\partial^2 T}{\partial \xi^2} \,. \tag{75}$$

The interface velocity u_{int} is given by equation (69) extended with the assumption of the temperature gradient located at the interface position $\xi = 0$ and using the defined constant C

$$u_{int} = C \left. \frac{\partial T}{\partial \xi} \right|_{\xi=0} \,. \tag{76}$$

Additionally, one can define the parameter

$$\eta = \sqrt{\frac{1}{2\kappa_0}} \frac{\xi}{\sqrt{t}} \tag{77}$$

and with the transformation

$$T(x,t) = B\phi(\eta) \tag{78}$$

an Ordinary Differential Equation (ODE) is defining the similarity solution

$$\phi'' + (\eta + \phi'(0))\phi' = 0 \,. \tag{79}$$

At the end the boundary conditions in a transformed version have to be used

$$\begin{aligned} B\phi(\eta = 0) &= T_{sat} \\ B\phi(\eta \to \infty) &= T_1 \,. \end{aligned} \tag{80}$$

By using this non-linear ODE a numerical solution was obtained using the Python script language to determine the temperature profile, interface velocity and the interface position at arbitrary times.

For the simulation the same fluid properties for water were used as already described in table 2 for the Stefan problem. Furthermore, the same numerical set-up as described in table 3 was used. Finally, the spatial discretization was set according to the observations from the Stefan convergence study in section 5.1.1.

With the use of equation (79) a similar temperature profile as in Konopka et al. [33] was used to define an initial temperature distribution

$$T(x, t = 0\,s) = T_0 + 5 \cdot 10^{15} \frac{K}{m^5} x^5 - 3 \cdot 10^{13} \frac{K}{m^4} x^4 + 6 \cdot 10^{10} \frac{K}{m^3} x^3 \\ -6 \cdot 10^{7} \frac{K}{m^2} x^2 + 28610 \frac{K}{m} x\,, \tag{81}$$

with $T_0 = 375.15\,K$ and using an initial interface velocity of $u_{int} = 0.1103\,\frac{m}{s}$ to begin the simulation with the temperature profile that the analytical solution provides for $t = 0.1\,s$. The simulation then starts again at a time $t = 0\,s$.

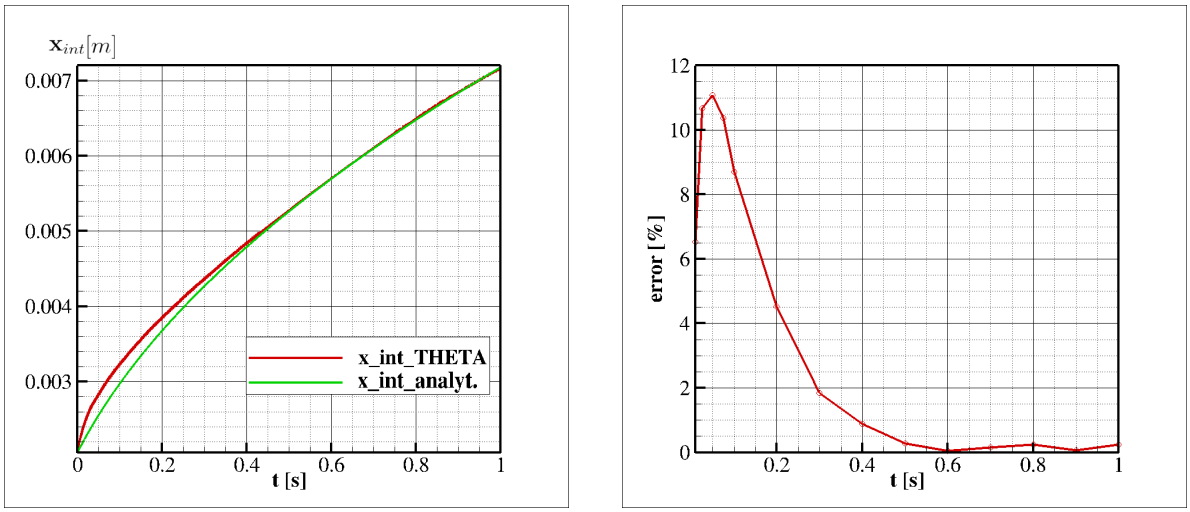

(a) Comparison of interface position from analytical solution (green line) and THETA (red line).

(b) Interface position error of THETA solution of Sucking-Interface Problem for the 500 cell grid solution.

Figure 18: Interface position of Sucking-Interface Problem.

The first figure in this set of comparisons is figure 18a and the corresponding error in the interface position in figure 18b. The overall match of the interface movement in the simulation to the analytical derived value is good. Only in the beginning the error

is around 11% but sharply dropping after this peak to values below 1.0% after 0.38 s of simulated, physical time and remaining at this level for the rest of the investigated time.

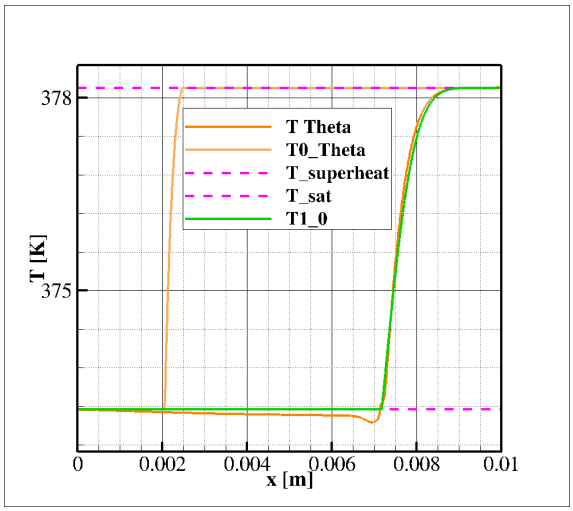

(a) Temperature profile of the analytical solution to the Sucking-Interface Problem and THETA.

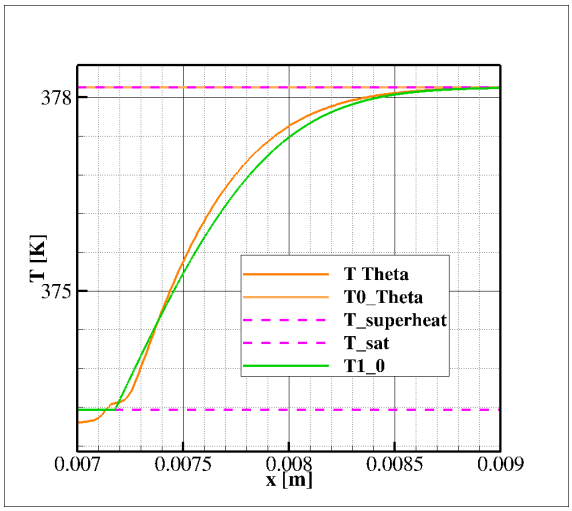

(b) Zoom into the interface area of the temperature profile of the analytical solution to the Sucking-Interface Problem and THETA.

Figure 19: Temperature profile of the Sucking-Interface problem at the end of the simulation at $t = 1\,s$. Shown are the saturation temperature and the liquid bulk temperature (bottom and top dashed purple lines, respectively). The analytical solution of the temperature profile (green line) as well as the simulated THETA temperature profiles at the beginning of the simulation ($t = 0\,s$, light orange line) and at the end ($t = 1\,s$, orange line)

Similar to the Stefan problem, the temperature development in the liquid and vapor phases are of high importance and were again compared to the analytical estimations as presented above. Figure 19a show the temperature profile along the length of the simulated domain. As an upper and lower boundary it is defining the respective temperatures in the vapor phase, which is $T_{sat} = 373.15\,K$ and $T_1 = 378.15\,K$, i.e. a superheat of $5\,K$, and the initial temperature profile at the initial interface position (light orange line) and sets it into relation to the analytical (green line) and numerically estimated profile (dark orange line). Figure 19b adds some detail by viewing a zoomed in version of the graph at the interface position at simulation end. In general the temperature, similar to the interface position, is in good agreement with the expected, analytical result. In the interfacial region, in particular at the vapor side of the interface, the simulation is undershooting the expected temperature value by a smaller value (less than $0.25\,K$). It should be pointed

out, that the result at the end of the simulation at $t = 1\,s$ fits the predicted length of the temperature boundary layer in the liquid and the gradient in the liquid, very well. A commonly used simulation duration was adopted e.g. from [7].

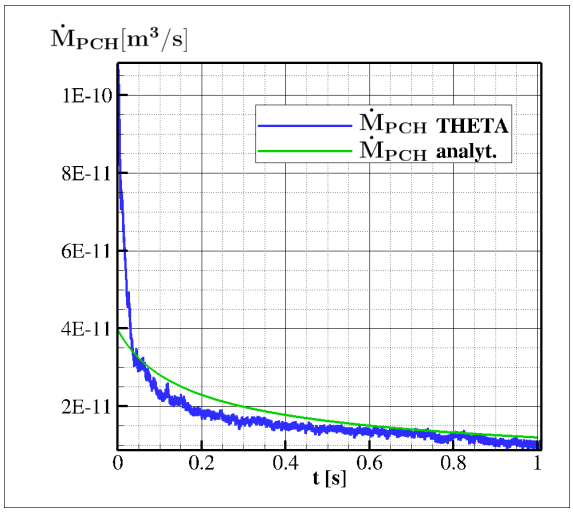

(a) Comparison of phase change mass flux $\dot{m}_{pch}$ of analytical solution (green line) and THETA (blue line).

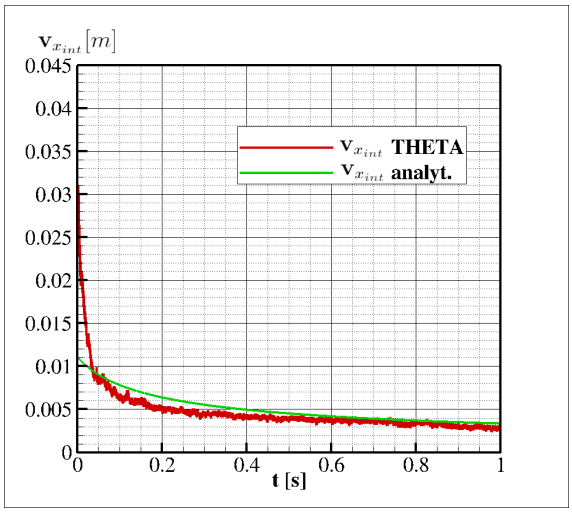

(b) Comparison of interface velocity v_{int} of analytical solution (green line) and THETA (red line).

Figure 20: Interface velocity and evaporation mass flux of the Stefan Problem.

The final set of graphs in figure 20 compares the mass flux as well as the interface velocity with the analytical derived value (similar to figure 12 and figure 13 in section 5.3). It is notable that the initial overestimation of the mass flux and thus the velocity the interface is progressing with. Here the mass flux is 2.5 times as large as expected from theory and the velocity is a similar order higher than expected. This difference vanishes very quickly and after $0.05\,s$, both, the mass flux as well as the velocity are close to the expected values again. Of course, the already observed fluctuations (compare section 5.1) are present again.

Similar to the Stefan problem, the Sucking-Interface problem is further evaluated and discussed in section 7.

5.3 *The Scriven Problem*

The growing vapor bubble in superheated liquid (also known as the Scriven problem) is a well-known test case to validate phase change codes and was first documented

by Scriven [65]. This test case has been used extensively to validate phase change codes e.g. by Wohak [23], Kunkelmann [6] and Sato and Ničeno [7].

A vapor bubble filled with fluid at saturation temperature T_{sat} is located in $1\,K$ superheated liquid and will expand due to the evaporation occurring at the vapor-liquid interface since there is heat flowing from the liquid into the vapor. It is similar to the Sucking-Interface problem of section 5.2 but now occurring in three spatial dimensions. Furthermore, surface tension effects now play a role since the interface is now curved. Similar to the two previous validation test cases an analytical solution exists that makes it possible to derive the expansion of the bubble (that is assumed perfectly spherical in the analytical solution) and the developing temperature profile at the interface. The new radius after evaporation that is present at a time t can be calculated as follows:

$$R = 2\beta_g\sqrt{\kappa_1 t}\,. \tag{82}$$

In order to determine the expansion coefficient β_g the solution to the equation

$$\frac{\rho_1 c_{p_1}(T_\infty - T_{sat})}{\rho_0(L + (c_{p_1} - c_{p_0})(T_\infty - T_{sat}))} = 2\beta_g^2 \cdot \int_0^1 \exp\left[-\beta_g^2\left((1-\zeta)^{-2} - 2\left(1 - \frac{\rho_0}{\rho_1}\right)\zeta - 1\right)\right] \mathrm{d}\zeta \tag{83}$$

is required. Due to the evaporation a temperature profile develops at the interface that can be described for the region outside the bubble radius $r > R$, where superheated liquid is present, and the region within the bubble interface $r \leq R$ where the vapor is at saturation temperature T_{sat}:

$$T = \begin{cases} T_\infty - 2\beta_g^2\left(\frac{\rho_0(L+(c_{p_1}-c_{p_0})(T_\infty - T_{sat}))}{\rho_1 c_{p_1}} x\right) \cdot \\ \qquad \int_{1-\frac{R}{r}}^1 \exp\left[-\beta_g^2\left((1-\zeta)^{-2} - 2\left(1-\frac{\rho_0}{\rho_1}\right)\zeta - 1\right)\right] \mathrm{d}\zeta & \text{for } r > R \\ T_{sat} & \text{for } r \leq R \end{cases} \tag{84}$$

One can define the Jakob number to specify the degree of superheat:

$$Ja = \frac{c_{p_1}(T_\infty - T_{sat})}{L}\,. \tag{85}$$

Also, for the growing bubble problem the in table 2 specified values of water and its vapor were used. This allows for the validation of the test case with an analytical solution that is well documented and derived in detail by Scriven [65]. Furthermore, the same numerical set-up as described in table 3 was used. Finally, the spatial discretization was set according to the observations from the Stefan convergence study in section 5.1.1.

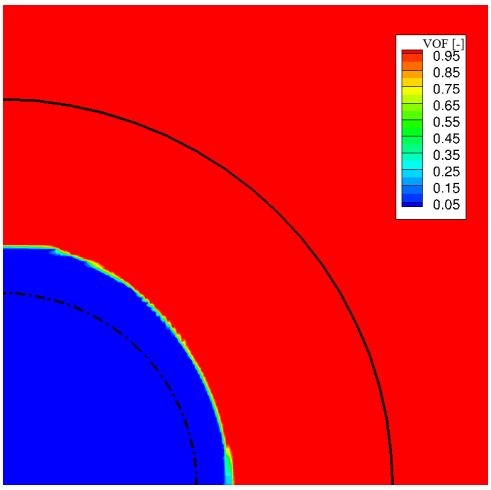

Figure 21: VOF distribution of the Scriven-problem at the end of the simulation at 0.15 seconds. Analytical solution to the Scriven-Problem radius (solid black line) and the solution of the THETA simulation. Dashed line: initial radius

A one-eighth element of the bubble was simulated, using symmetry boundary conditions at the cut areas of the bubble as well as an outflow boundary condition at the top, an approach that is similar to the Stefan- and Sucking-Interface problems. The starting set-up with an initial radius of $0.001\,m$ is visualized in figure 21 with the dashed line in a 2-D cut of the bubble sector boundary. The solid black line indicates the expected analytical result whereas the interface region is indicated in green. The expected radius could not be reached for the conducted simulation since the surface tension had to be reduced by a factor of 10 to improve numerical convergence. This was intended to allow for a stable solution. This reduced surface tension is thought to be responsible for the decreased bubble growth since the pressure jump over the interface is now smaller, hence

the ability to grow against the fluid back-pressure is reduced. In the end, this leads to a smaller than expected radius.

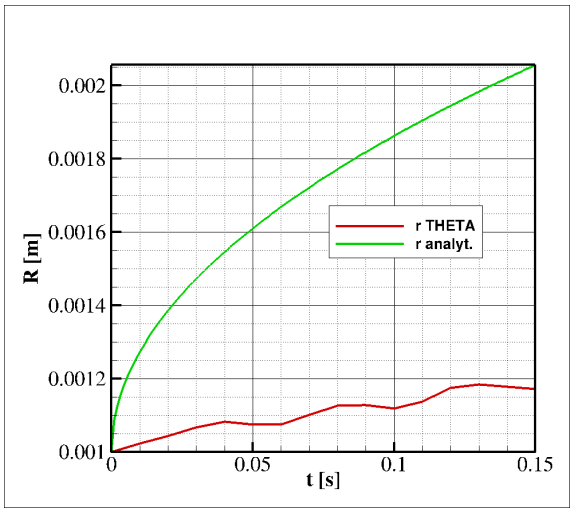

(a) Comparison of bubble radius growth of the analytical solution (green line) and the THETA simulation (red line).

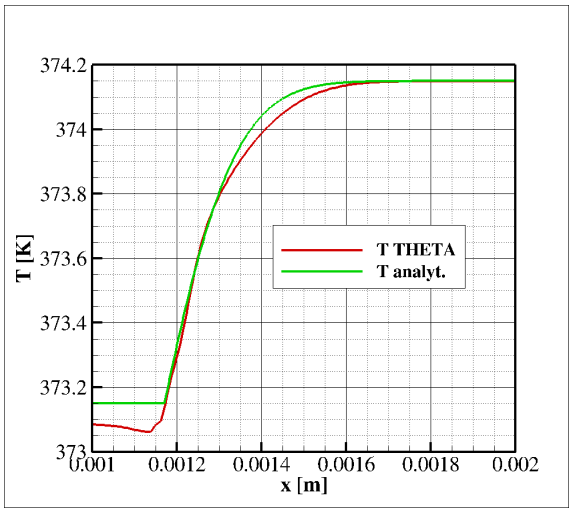

(b) Comparison of temperature profile T of analytical solution (green line) and the THETA simulation (red line).

Figure 22: Radius development over time and the temperature profile of the Scriven-Problem at the end of the simulation at 0.15 seconds.

Figure 22a shows the bubble growth over time and figure 22b the thermal profile at the simulated radius compared to the analytical temperature profile for that radius. Both analytical solutions are depicted with a green line. The temperature profile is also matched with a slight underestimation of the vapor temperature slope when the temperature profile in the liquid reaches the overheat temperature again although the expansion of the bubble has not reached the expected state. The temperature profile is in line with the results from the Sucking-Interface problem in section 5.2.

Additional insights into the problematic interface expansion are provided in figure 23, which shows the temperature field of the bubble again after the simulation was concluded after $0.15\,s$. From this it is visible that the interface progression is limited to a lower value and some so-called parasitic currents are visible at the top curvature of the bubble, indicating the influence of the surface tension on the flow field around the bubble. Thus, disturbing the smooth transition along the bubble surface from the interface temperature to the over-heated temperature in the liquid. The observed phenomena were observed to be independent of the applied mesh density.

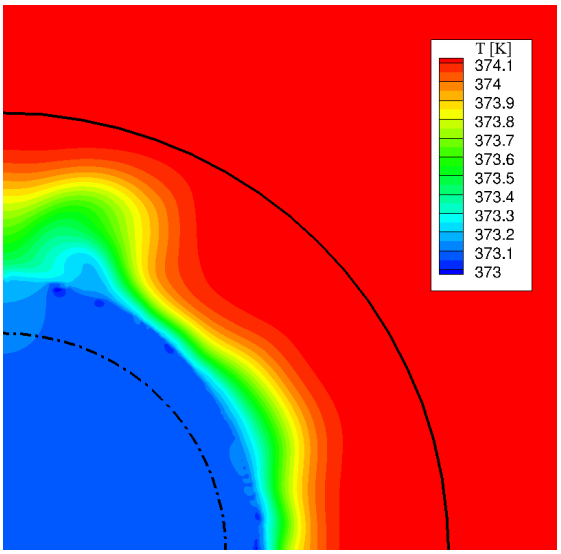

(a) Temperature field of the Scriven-problem around the growing bubble.

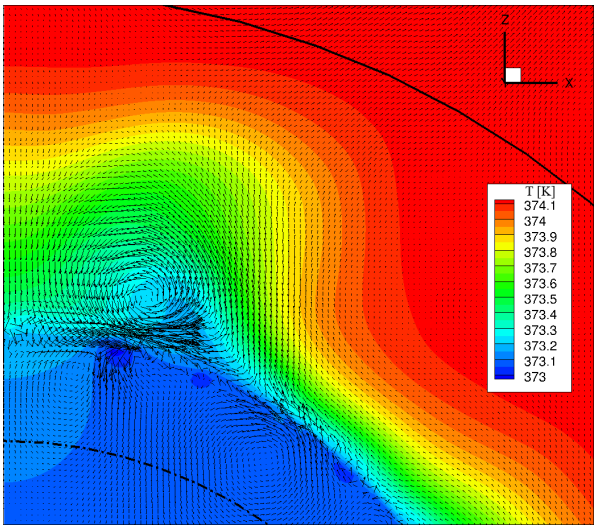

(b) Zoom in the temperature disturbance of the Scriven-problem with the velocity as scaled vectors in the graph plane.

Figure 23: Temperature contour of the Scriven-Problem with the initial radius (dashed-dotted black line) and the expected bubble radius (solid black line)

In the future, additional test cases should be considered to further validate the current state of the code. It is conceivable that the meniscus evaporation test case as used in Kunkelmann [6], the droplet evaporation test investigated for example by Hardt and Wondra [22] as well as different film boiling cases e.g. Welch and Wilson [25] might be useful.

6 The KOALA Stratification Test Case

6.1 *Stratification Process in Upper-Stages of Space Launch Systems*

It has been pointed out in chapter 1.1 that thermal stratification will play a vital role in the characteristics of the propellant during the propulsive and ballistic phases. Especially pump-fed, chemical engines, as it is the case for example for the Ariane 5, require a specified tank inlet pressure to guarantee a smooth operation. This is of utmost importance since cavitation in the pump has to be avoided at any cost.

Thermal stratification is a process that, through a heat flow into a fluid, causes the development of thermal gradients. An important example is the solar radiation that heats the upper stage during the ballistic orbital transfer and causes the cryogenic propellant to stratify prior to engine re-start. These stratifications will result in varying thermal states within the propellant. The then following extraction of liquid towards the engine may therefore include propellant that is outside the narrow pressure and temperature state that is required for the turbo machinery and the following engine in order to function as designed. Some of the most distinguished physical phenomena taking place are listed below (Ratner et al. [8]):

- Microgravity environment
- Solar heat loads
- Thermal conditioning by spinning around the longitudinal axis
- Buoyancy induced recirculation
- Molar diffusivity between propellants and pressurants
- Thermal conduction within tank walls and propellant
- Surface tension effects

In this work, we will focus our effort to investigate stratification effects, which are caused by external heat loads and buoyancy induced recirculation. A schematic overview of the mentioned effects is shown in figure 24.

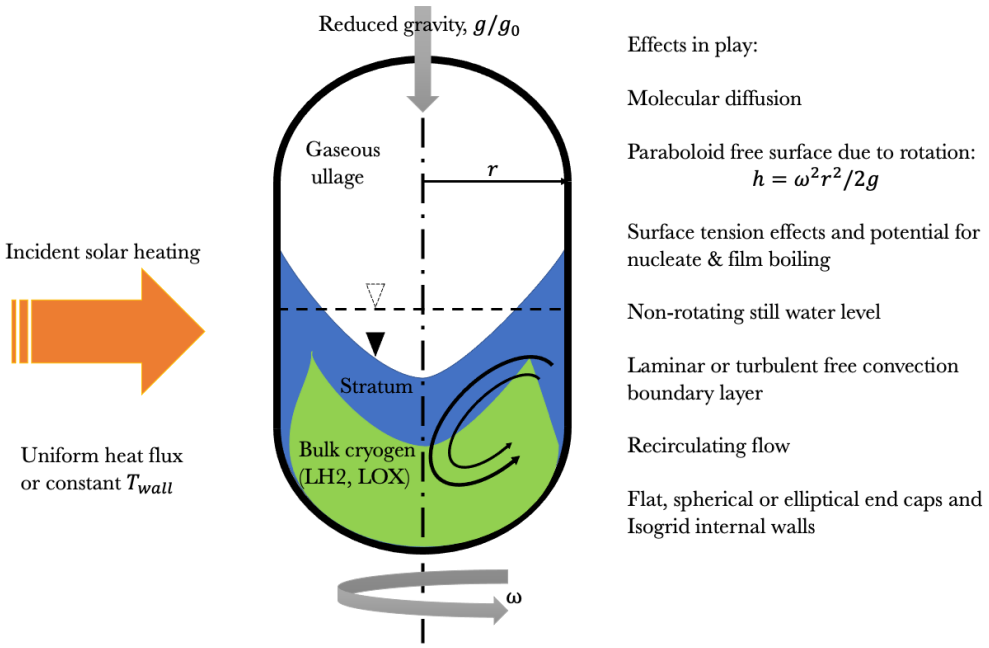

Figure 24: Simplified overview of physical processes in a cryogenic propellant tank after-Ratner et al. [8].

The major effect that plays a role in the modeling of stratification processes is the buoyancy-induced natural convection due to the already mentioned solar heating or, in a minor range the heat produced by the firing engine. Conducted through the tank walls this heat increases the temperature of the adjacent fluid, whose density is decreased (equation of state, equation (1)). A free-convection boundary layer then transports this mass along the tank walls upward into the upper region of the cold bulk. Here, the heated fluid forms a thermally stratified layer.

These kind of flows are specified by the *RAYLEIGH* number Ra. The similarity number is a product of the *GRASHOF* number Gr and the *PRANDTL* number Pr, where the Gr number specifies the ratio of buoyancy to viscous forces and the Pr number the momentum to the thermal diffusivity:

$$Ra = \frac{g\beta\Delta T L^3}{\nu^2}\frac{\mu c_p}{\lambda}\,. \tag{86}$$

The temperature difference ΔT is here specified between the wall and the cold bulk

temperature. Usually, the boundary layer develops at the bottom edge of the tank wall and up to the interface along the tank walls [8]. The boundary layer usually changes from laminar to turbulent flow at $Ra = 10^9$. For the case of an instantaneous change Ratner et al. [8] maps Ra as a function of the reduced gravity ratio g/g_0 for LH2 for different ΔT (see figure 2 in Ratner et al. [8]). The horizontal $Ra = 10^9$ line there separates laminar from turbulent flows.

Again, the heat enters the tank through the boundary layer and all mass flow will be driven upwards to the surface by the Boussinesq mechanism that will form a thermally profiled stratum with the hottest liquid on top and decreasing temperature towards the bottom down to the bulk temperature. There might also exist an energy exchange between the ullage gas and the bulk liquid depending on the conditions at the interface in the tank.

In general, stratification will occur faster with increased gravity level since the driving force, buoyancy, will increase with a higher gravity force causing it. Also, this effect depends on the present fluid. Considering water, LH2 and LOX; water will stratify the fastest, followed by LH2 and LOX being the slowest of these three.

In a nominal operational case, the upper stage will be in the so-called "barbecue mode", which means it will rotate around its longitudinal axis, in order to keep the thermal load uniform, independent from the current attitude towards the sun. This rotation will result in the free surface forming a paraboloid, which practically increases the heating area of the liquid in the tank due to the increased wall area covered by the propellant, whereas the volume will remain constant. Generally, the stratification will be larger with increased rotation although the present low rates of rotation essentially keep the stratification time unaffected (Ratner et al. [8]).

Finally, secondary flow recirculation will also force liquid downward at the centerline, dragging warm liquid with it. This effect is induced by the rising free convection boundary layer flow.

6.2 *Experimental Set-up*

The experiment consists of a dewar that contains 52.1 l of LH2. It is built upon a super-insulated casing that includes a LN2 heat shield between the inner and outer tank wall in the casing. The test volume is also separated from the surrounding atmosphere by shielding in the neck region of the tank. Figure 25 sketches the engineering detail drawing of the dewar compartment and the neck as well as all important volumes, inner

and outer dimensions. Not indicated is the wall thickness of $3mm$. Also visible is the sensor equipment that consists of fill level sensor and an array of temperature sensors with an accuracy of $\pm 0.25\,K$. Those temperature sensors are placed along a vertical line reaching from the top of the dewar down to almost the bottom of the tank. Detailed sensor positions can be found in figure 26b. Three additional sensors are placed in the neck of the tank. The sensor line in placed $0.040\,m$ from the center line of the dewar. Several depicted sensor positions were used to compare the numerical to the experimental values. These data points will be compared in section 6.4.1.

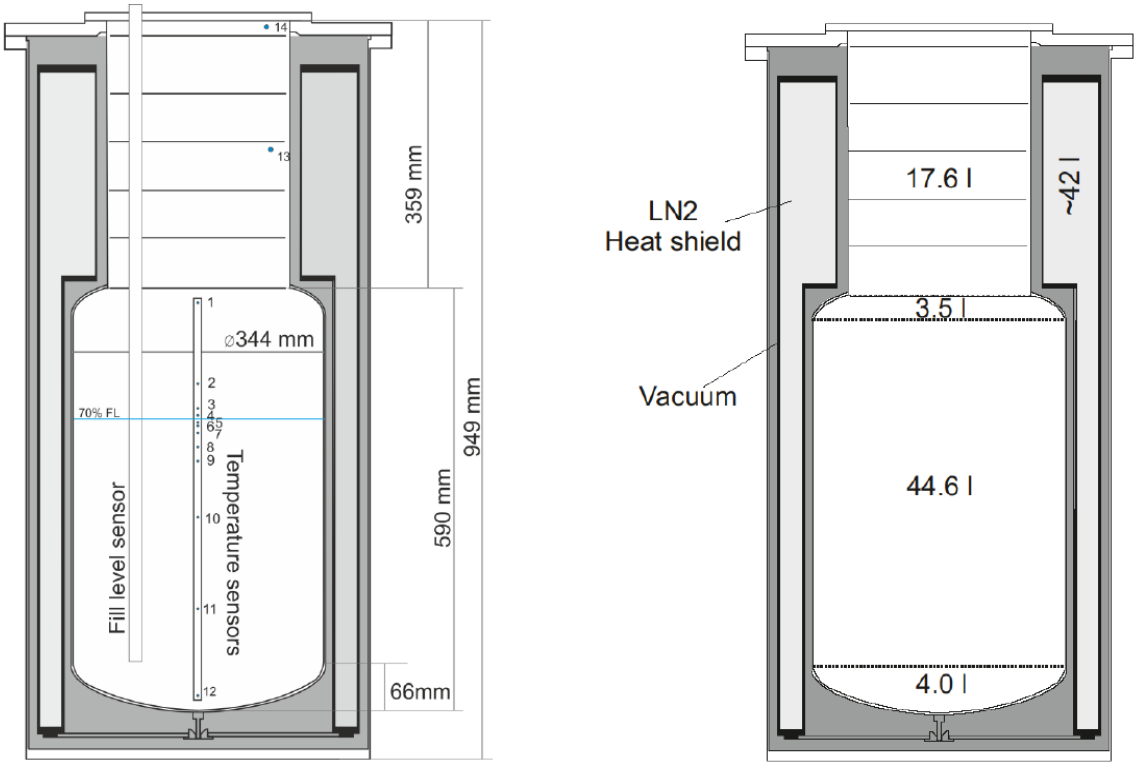

Figure 25: Sketch of the engineering detail drawing of the dewar compartment [9]. Copyright: **ArianeGroup GmbH, 2018.**

The original experiment was composed of two different sequences: one for stratification and the second to demonstrate the pressure evolution. Since it is not feasible due to the incompressible character of the THETA solver, to conduct a numerical study of the pressure evolution it was chosen to simulate only the stratification part of the experiment. The experimental sequence is described in Konopka et al. [9] and shall be numerically

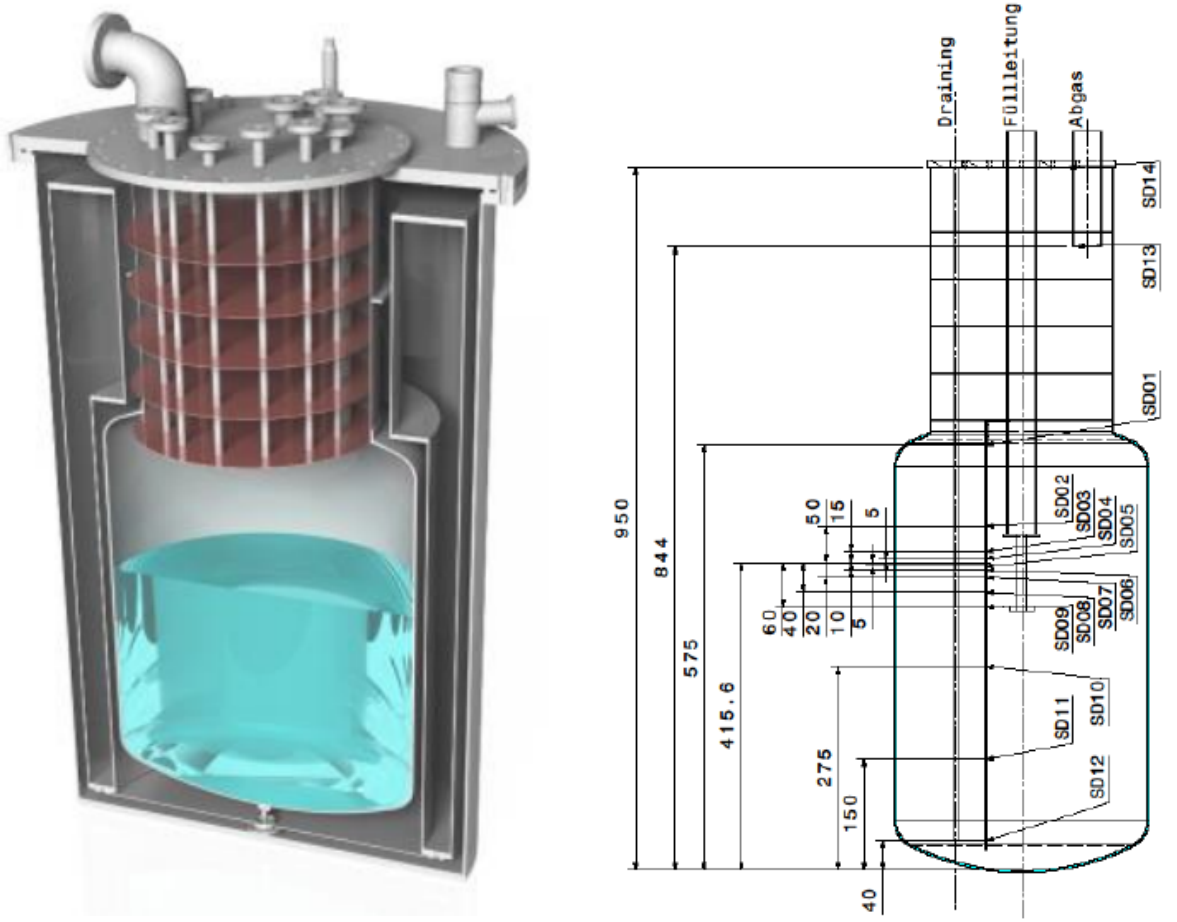

(a) A Render of the KOALA experiment. Copyright: **ArianeGroup GmbH & DLR, 2018.**

(b) Layout of the sensors in the dewar compartment. Copyright: **ArianeGroup GmbH, 2018.**

Figure 26: Additional information on the KOALA set-up (see Konopka et al. [9]).

studied with the present code here. The experimental sequence proceeds as follows: At first the dewar is filled with LH2 at 1 bar and saturation conditions. After the boil-off mass flow remains constant, the exhaust line is closed, and Gaseous Hydrogen (GH2) at 288 K is used to pressurize the tank to 3 bar internal pressure. When the prescribed pressure is reached the filling of the dewar with GH2 is on hold and a pressure-exchange valve keeps the pressure level at 3 bar. During the remainder of the stratification part of the experiment this facilitates the needed GH2 or venting gas i.e. that is the excess amount of GH2. The incompressibility assumptions approximately hold for 700 s after the 3 bar

threshold is reached. It was shown by Konopka et al. [9] that the total integrated heat transfer into the vessel triggers transitional phenomena after about 700 s, which violate the present modeling assumptions of a laminar flow. Hence, the comparison is limited to the time period before this event. Therefore, the simulation will also be conducted for this time duration.

6.3 *Numerical Set-up*

The numerical simulation is conducted with the herein presented update of the DLR THETA code, which is based on version 10.1. Centaur 13.1 was used to prepare the mesh. For the simulation the dewar was meshed as a full 3D model up to the neck, excluding the separating part to the surrounding.

Figure 27 is depicting the mesh that is used for the simulations. The discretization was chosen according to experience with previous evaluations of Gauer [60] and Konopka et al. [9]. The mesh is completely unstructured including the upper boundary condition that is meshed with very fine unstructured cells to improve the convergence at this boundary, especially at the rim of the dewar. A finer discretization at the inflow plane was found to efficiently damp spurious oscillations, which occur on course grids. The interface at the fill-level range of LH2 during the simulation is refined to improve the resolution of the interface region between liquid and gaseous fluid and the resolution of the thermal boundary certainly developing here. Finally, the wall region is refined as well to aid the resolution and development of the thermal boundary condition at the wall. Resolution in the liquid bulk regions of liquid and gas is reduced to safe cells.

The most important mesh statistics are provided in table 4.

Metric	Unstructured cells	Structured	Unit
Mean size	0.813	–	m
Max. size	0.999870	–	m
Min. size	0.073700	–	m

Table 4: Mesh statistics of the used Centaur mesh.

The relevant fluid values for LH2 and GH2 are provided in table 5.

The initial profile for the temperature and the VOF value are shown in figure 29. The temperature profile is modeled as a linear function according to the profile provided at the initial time of the experiment when the pressure was controlled to remain constant. The fill-level was set to $h_{fill} = 0.415\,m$ and the surrounding mesh was refined.

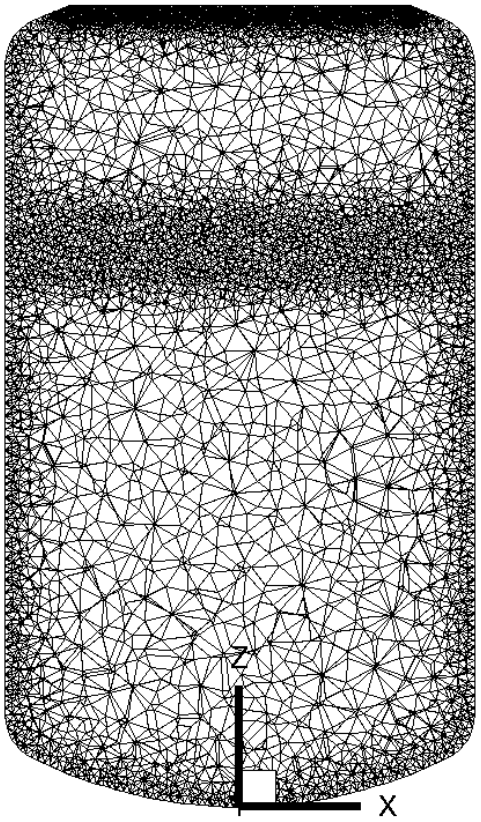

(a) A vertical cut through the mesh.

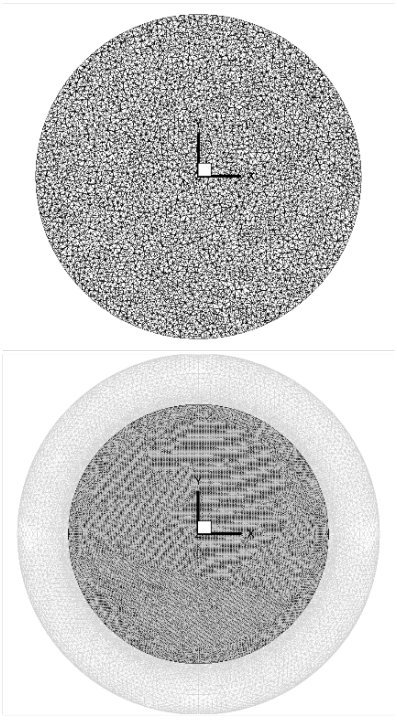

(b) A horizontal cut through the mesh at the interface (top) and the outflow level (bottom).

Figure 27: The three most important cuts through the mesh: vertical slice (27a) and through the interface and outflow boundary condition level (27b)

Furthermore, the initial set-up of the simulation is depicted in figure 29, the VOF value to the left and the temperature on the right. The initial temperature profile over the height of the dewar is also presented in figure 30, reflecting the linear character of the initial distribution.

The simulation was set-up with the following boundary conditions: three wall boundaries and a total pressure plane. The total pressure planes were used for the exit plane at the top boundary of the dewar. It is responsible for setting a constant pressure of $3\,bar$ and to maintain, depending on the conditions in the tank, the in- or out-flowing mass to keep the pressure at the prescribed level. The assigned boundary part on the top of the dewar is a relatively thin ring. The remaining top part of the dewar is a circular, laminar wall boundary that contributes a constant heat flux into the gaseous phase.

The tank walls themselves are split into two parts that are divided by the initial

Fluid	Index	ρ	c_p	λ	μ	L	σ	T_{sat}
vapor	0	1.187	10686	0.0464	$2.1 \cdot 10^{-6}$	–	–	–
Liquid	1	71.084	9693	0.1044	$1.37 \cdot 10^{-5}$	$451.9 \cdot 10^{3}$	0.002	24.68
Units	[–]	$\left[\frac{kg}{m^3}\right]$	$\left[\frac{J}{kgK}\right]$	$\left[\frac{W}{mK}\right]$	$\left[\frac{Pa}{s}\right]$	$\left[\frac{J}{kg}\right]$	$\left[\frac{N}{m}\right]$	$[K]$

Table 5: Fluid properties of liquid hydrogen and its vapor.

interface position at the walls. Both wall boundaries are also laminar and contribute a fixed heat flux in the gaseous and liquid phase, respectively.

In table 6 an overview of the described boundary set-up is presented with respective details of the implemented parameters that apply.

Boundary Name	Sub-Type	Parameters	Thermal Type	Elements
total pressure plane	in- and outflow	$T = 62\,K$	isothermal	5135
wall	laminar	$\dot{q} = 40\,W/m^2$	fixed flux	14120
wall gas	laminar	$\dot{q} = 40\,W/m^2$	fixed flux	19143
wall liquid	laminar	$\dot{q} = 40\,W/m^2$	fixed flux	22031

Table 6: Mesh boundary condition overview of the used mesh.

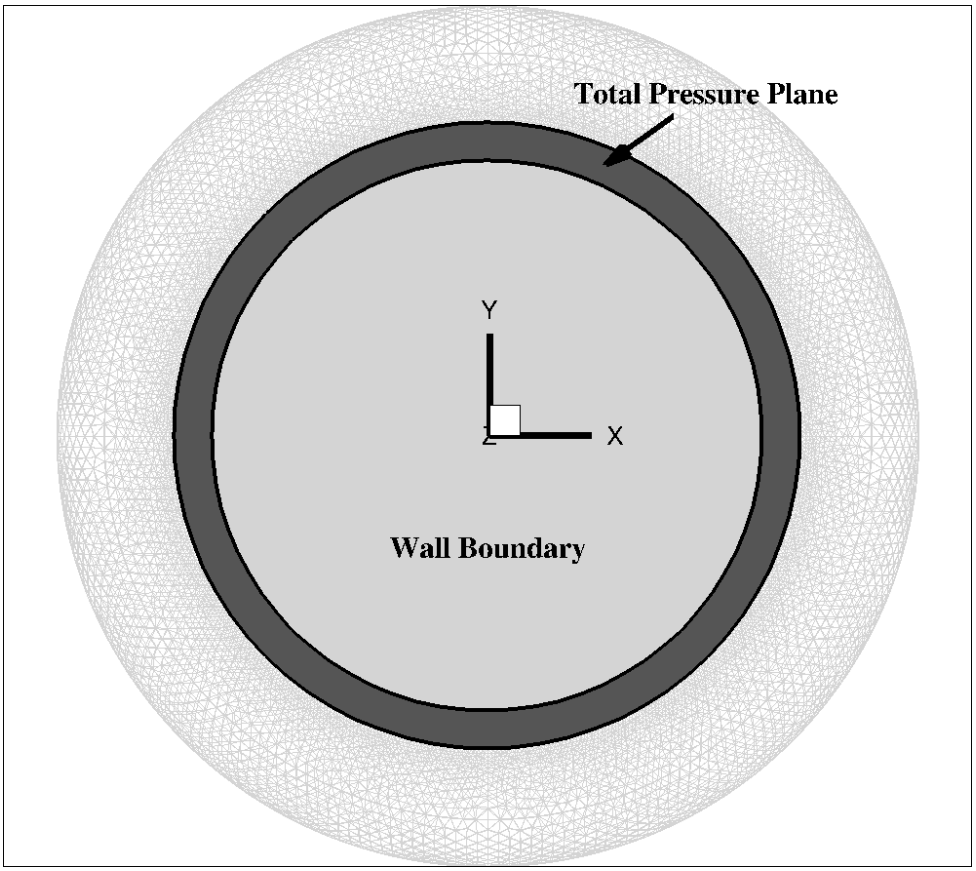

Figure 28: Depiction of the outflow region of the dewar, differentiating between the total pressure plane (dark grey) and the wall boundary (light grey). The visible, transparent mesh is the curved upper section of the dewar that is a wall boundary condition as well.

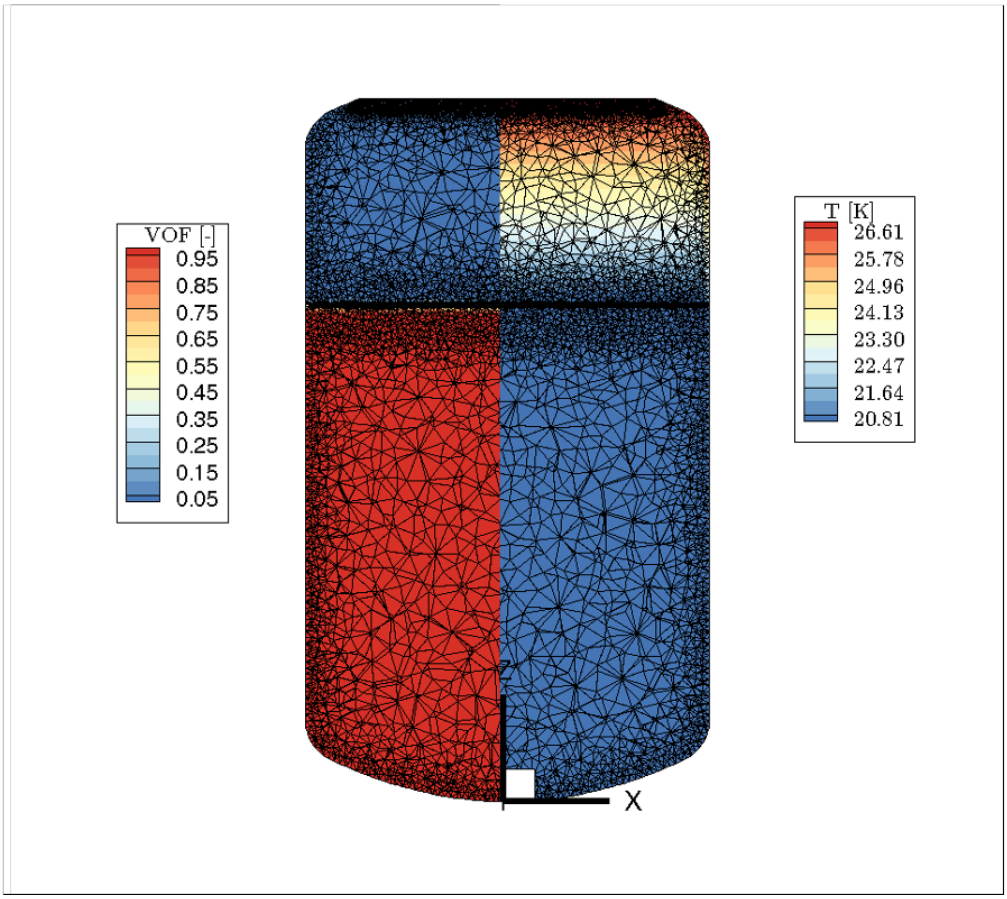

Figure 29: Sketch of the initial temperature and VOF distribution in the dewar.

6.4 *Comparison of CFD to Experimental Data*

In the next section, the simulation will be compared to the available experimental measurements. They were performed by Airbus DS and DLR (Konopka et al. [9]) and explained in section 6.2. The comparison will mainly cover the temperature profiles of the vertical sensor array (section 6.4.1), the fill-level of the dewar (section 6.4.2), and the mass flow rate at the pressure control valve (section 6.4.3).

6.4.1 Temperature Profiles

In this section the temperature profiles of the conducted THETA simulation will be compared with the experimental measurements performed by Airbus DS (now Ariane Group). The different sensors listed in table 7 and were selected to get a good distribution of measurement points along the vertical axis of the dewar, in both the gaseous and liquid medium. Figure 26b shows the technical realization of the sensor line and the distribution of thermal sensors.

Sensor	$xin\,[m]$	$yin\,[m]$	$zin\,[m]$
SD12	0.04	0.0	0.0400
SD11	0.04	0.0	0.1500
SD10	0.04	0.0	0.2750
SD09	0.04	0.0	0.3556
SD08	0.04	0.0	0.3756
SD07	0.04	0.0	0.3956
SD06	0.04	0.0	0.4056
SD05	0.04	0.0	0.4106
SD04	0.04	0.0	0.4206
SD03	0.04	0.0	0.4306
SD02	0.04	0.0	0.4656
SD01	0.04	0.0	0.5750

Table 7: Temperature sensor array positions along the sensor line (Konopka et al. [9]). See 26b for the visualization of the sensor line and the distribution of thermal sensors in the dewar.

The graphs will show the THETA solution as a solid line using five different data points for, which temperature measurements of the LH_2 tank exist. The measured values are presented as a point value in the graphs. A connecting line is plotted to guide the eye. At these points an error bar is included that presents the possible error of the used temperature sensors, which is specified with $\pm 0.25\,K$ [9]. The profiles are plotted as vertical

height in the dewar over temperature, illustrating the distribution of the temperature as a vertical cut through the dewar.

The liquid phase temperature, which ranges from the bottom of the dewar to the initial fill-level of $0.415\,m$, is constant in the presented case at the initial simulation state. In contrast, the vapor phase, ranging from the vapor-liquid interface at $0.415\,m$ to the outflow of the dewar at $0.59\,m$ (not taking into account the neck of the tank), increases from the liquid temperature of $T_{liq} = 20.3\,K$ to the temperature of the outflow boundary condition of $T_{vap} = 26.65\,K$. Figure 30 exemplifies this case, showing that the experimental distribution of the temperature (dashed dark grey) closely corresponds to the assumed distribution in the THETA simulation (solid dark grey line).

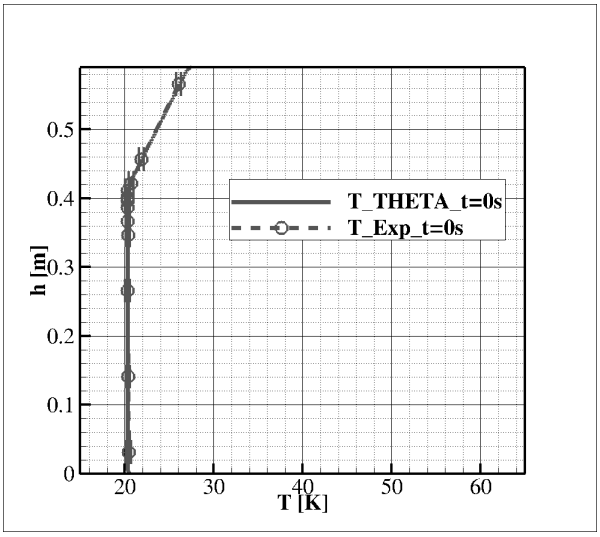

Figure 30: Comparison of temperature profile from the experiment and THETA at $0\,s$.

Figure 31a and figure 31b present the profiles for the first $100\,s$ and compare them to measurements taken at $60\,s$ and $100\,s$. For figure 31a the liquid temperature of the simulation (solid red line) is in good agreement with the experimental values (dashed red line) of the measurements and also lie well within the error bars. The comparison is different for the values in the vapor phase where the development of the temperature within the vapor deviates significantly from the experimentally measured values. The plot shows that the temperature development in the vapor lags behind the actual documented profile, hence the simulation predicts a lower temperature for most of the vapor phase. In details this means that at a fixed height in the dewar e.g. $h = 0.5\,m$ that the temperature

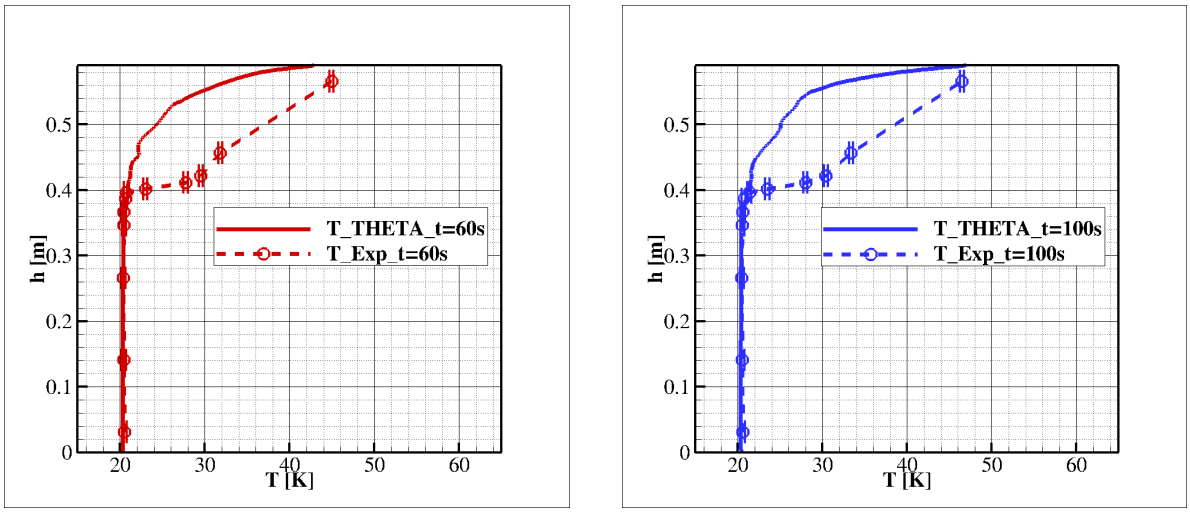

(a) Comparison of temperature profile from the experiment and THETA at 60 s.

(b) Comparison of temperature profile from the experiment and THETA at 100 s.

Figure 31: Temperature comparison between experiment and numerical solution.

is only 24 K instead of the measured 37 K. This represents a deviation of roughly a third. The simulation only gets near the vapor temperature at the interface and towards the top of the dewar. This picture repeats closely for the temporally not far advanced temperature distribution in figure 31b at 100 s, which is very similar to the one shown in figure 31a.

The subsequent figure 32a show the profile for a later point in time of 400 s. Visualized here is that large parts of the liquid body away from the inter-facial region remain just below the now increasing liquid temperature that was measured in the experiment. Although the temperature generally remains below 21 K in most of the liquid body. The temperature adaption from the liquid to the vapor within the interface region is captured well for the 400 s case and with time advancing the vapor in the simulation also approximates the measured case. Still, for most of the vapor region of the simulation, the temperature is still lower at the same position within the vapor region of the dewar. The high deviation that was present in the preceding comparisons at 60 s and 100 s in figures 31a and 31b has now vanished.

Finally, figure 33 displays the temperature profile and a contour plot of the dewar at the end of the simulation at 700 s. Again, shown in figure 32b is that large parts of the liquid body away from the interracial region remain just below the liquid temperature that was measured in the experiment. On the other hand, the temperature profile of the

simulation (solid green line) is now heated over the actual measured results. In contrast, the temperature in the gaseous phase does not significantly evolve for most of the LH_2 filled volume. For the vapor region, the temperature at a given position is still mostly below the measured value. Notable is the high temperature in the simulation compared to the experiment in the top of the dewar above the $0.56\,m$ line. Unfortunately, the simulated value cannot be confirmed by a measured value, but an increase by roughly $10\,K$ from the $400\,s$ solution in figure 32a to the $700\,s$ solution in figure 32b is visible.

In contrast, figure 33 shows the complete temperature contour plot of the dewar at $700\,s$. Similar to figure 29 the mesh is visible, with its refinement structure in the interface area. The interface itself is resented by the horizontal bold black line and moved up compared to the initial position. More details about this movement are given in section 6.4.2. Clearly visible is the hot vapor region in the tank that transfers the heat into the interface region and the liquid below. Here the liquid cools down from the interface temperature to the bulk temperature of the liquid phase. This region is well mixed and no strong temperature gradients prevail. In contrast, the vapor phase has strong gradients as the temperature increases from interface to the top of the dewar.

Position	Error $60\,s$, [%]	Error $100\,s$, [%]	Error $400\,s$, [%]	Error $700\,s$, [%]
0.575	27.2050	29.6072	13.8656	14.4580
0.4656	30.1458	32.3218	24.5130	16.1896
(0.4306)	28.2352	29.0895	12.4886	0.2614
(0.4206)	24.4214	23.2823	2.8581	−11.7659
0.4106	8.9015	9.0136	−4.2375	−19.5715
0.4056	−1.1196	0.7318	−5.9199	−20.1371
(0.3956)	−0.8179	−1.0913	−4.9155	−14.7856
0.3756	−0.0863	0.2149	−2.1593	−5.1585
(0.3556)	0.3974	0.5175	0.2661	−0.3385
0.2750	0.3060	0.4798	1.3671	1.9661
(0.1500)	0.6784	0.9398	1.7321	2.2780
0.0400	1.1481	1.4539	2.3549	2.8891

Table 8: Temperature error along the sensor line during different times in %. Brackets in the position column indicate sensor positions not plotted in the temperature comparisons the figures in this section.

Table 8 shows an overview of the errors when comparing experimental measurements points with the corresponding simulated values at these positions in the dewar. From the relative errors it is observable that the temperature in the simulation remains close to experimentally measured values within the liquid phase of the fluid (The error generally

stays below $\pm 5\,\%$ for values up until the sensor at $0.4056\,m$ where also only the simulated values later than $400\,s$ do exceed this level and have partially much higher errors of up to $-20\,\%$). On the other side, within the gaseous phase of the hydrogen tank, the errors are relatively large, ranging from relatively close 14.45% at the top of the tank at the end of the simulation to 32% at $0.4656\,m$ at $100\,s$ simulated time. Thus, in general the previous observation is confirmed that at the beginning of the simulation the errors are quite large in the gaseous hydrogen phase but are reduced the longer the simulation lasts. For the interface region the opposite observation is true where at the first $400\,s$ the error remains low at sensors between $0.4106\,m$ and $0.3556\,m$ thus suggesting a good fit to the actual measurements. When the simulation progresses to $700\,s$ these errors increase and reach a value of $20\,\%$ at a height of $0.4056\,m$.

In Ludwig [49] the importance of the pressurization gas to the development of the temperature profile in the ullage is stated. Controlling the inflow temperature of the gas is not a standard functionality of the THETA code and was therefore not applied. Instead supplied gas, which needs to enter the simulation domain to maintain the pressure level due to condensing vapor, has the temperature that is defined at the total pressure plane used at the top of the tank. This temperature value was initially set to $T_{in} = 62\,K$. Furthermore, it is visible that motion only kicks in after 310 sec - see figure 39 - so no motion was present for the initial simulation.

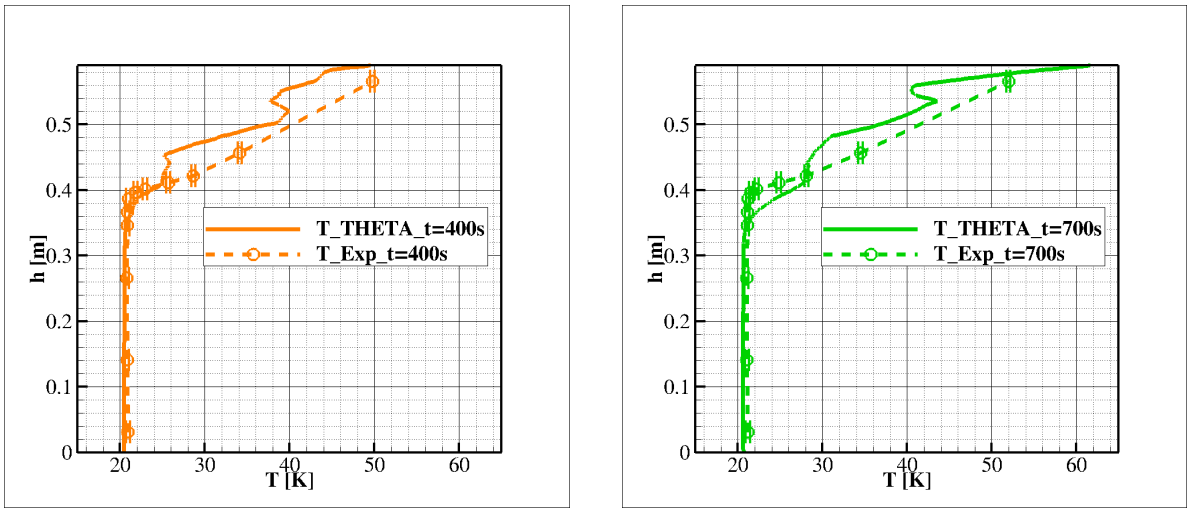

(a) Comparison of temperature profile from the experiment and THETA at $400\,s$.

(b) Comparison of temperature profile from the experiment and THETA at $700\,s$.

Figure 32: Temperature comparison between experiment and numerical solution.

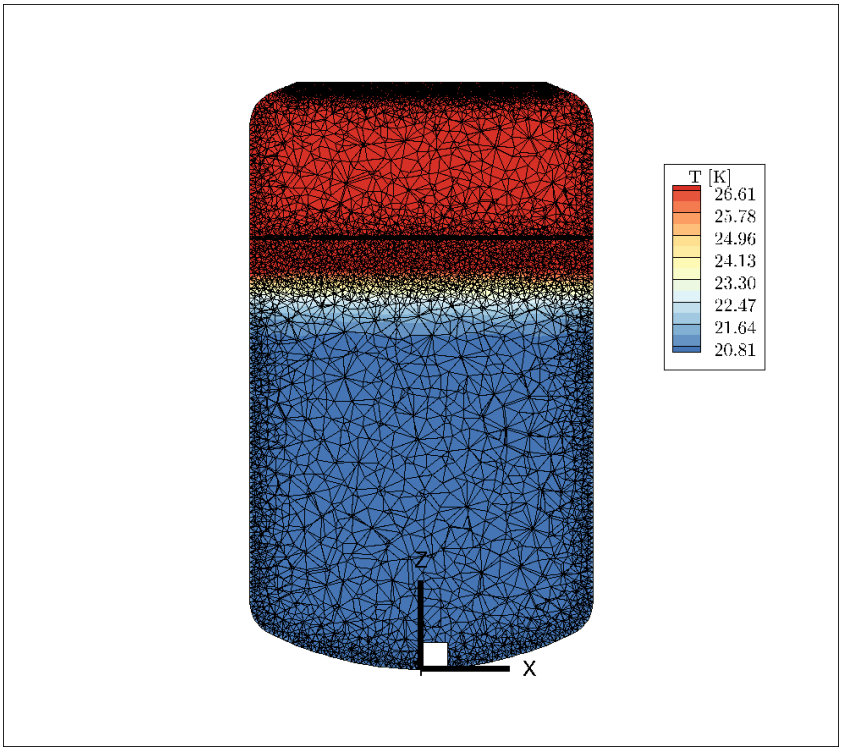

Figure 33: Temperature contour from the THETA simulation at 700 s.

Figure 34 shows a zoomed in and combined version of the previous figures allowing to better compare the solution in the crucial area of the interface. The figure shows the cases at 100 s, 400 s and the final profile at 700 s in figures 34a, 34b and 34c, respectively. Always included in the figure is the initial temperature profile at the beginning of the simulation (0 s, dark grey solid and dashed lines, compare figure 30). Again, for the liquid phase it is observable that the simulation is within the error bars of the measurements for at least the first 100 s (possible longer), as the next available measurement at 400 s is outside or at the lower edge of these error bars. Only the last measurement at 700 s is visible outside the error bars with errors as indicated in table 8. Especially, the values in the interface region are hotter in the simulation compared to the measured values in the experiment. In conclusion, the development of the stratified liquid lacks behind compared to the experimentally measured values, although the error remains low for most of the liquid body, except for the interface region in later parts of the simulation.

Furthermore, it is visible that the transition from liquid to gaseous phase in the interface region is relatively well captured by the measurements at times ranging from 100 s

to 400 s. Additionally, the deviation is visible in the gaseous phase from the experiment. This deviation has already been discussed earlier for the earlier cases, specifically visible in figure 34a. Here the experimental measurements suggest a higher temperature

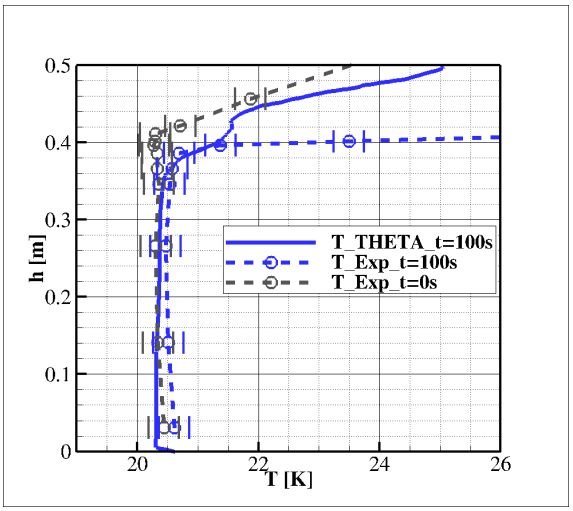

(a) Comparison of temperature profiles from the experiment and THETA at 0 s and 100 s zoomed in to the interface area.

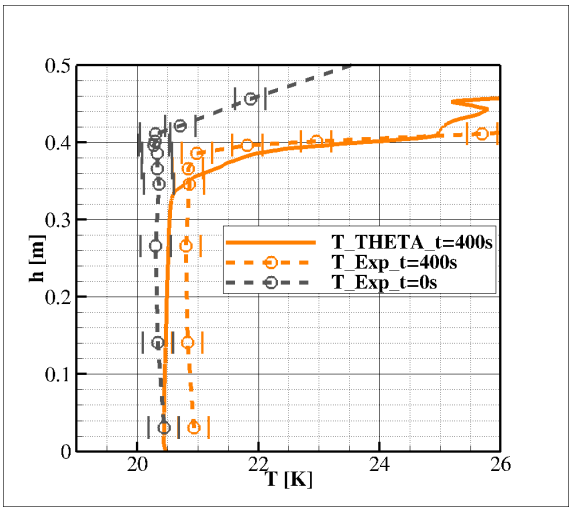

(b) Comparison of temperature profiles from the experiment and THETA at 400 s zoomed in to the interface area.

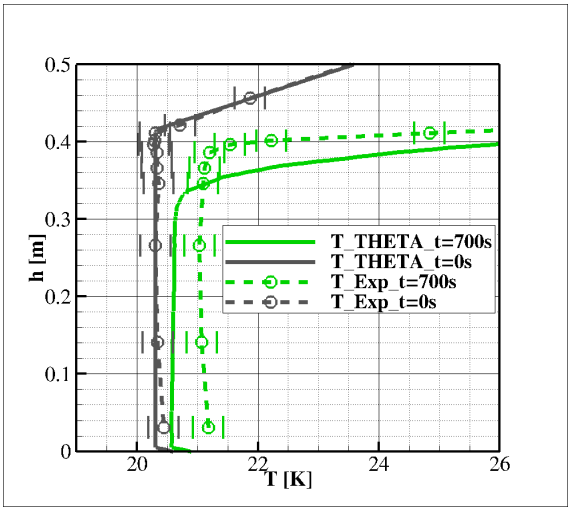

(c) Comparison of temperature profiles from the experiment and THETA at 700 s zoomed in to the interface area. Shown is also the initial temperature profile from experiment and simulation (grey lines)

Figure 34: Temperature comparison between experiment and numerical solution.

compared to the simulation performed with THETA i.e. for example the $21\,K$ mark should reach a height of roughly $0.4\,m$ but reached only a height of roughly $0.48\,m$ in the simulation. In the $400\,K$ case the match between measurement and simulation is good up to the $25\,K$ point where the temperature raises are more pronounced in the gaseous phase and the measured temperature is underestimated again in the simulation. This trend reverses in the last comparison in figure 34c. For the latest measurement at $700\,s$ the simulated temperature profile deviates stronger within the liquid but following the general trend of the development as is also shown in figure 33. Here the temperature at the interface region is overestimated by the simulation up until the $28\,K$ mark (compare figure 32b) where again the simulated $GH2$ temperature is not reached until the top of the dewar.

6.4.2 Fill-Level

This section discusses the development of the fill-level during the conduction of the simulation and will compare it to the experimental data. Figure 35 shows the fill-level increase during the conduction of the simulation. It is raising from an initial level of 0.41516 to a final level of 0.43302. The fill-level was assumed to be the height-level in the tank, at which the VOF value is equal to 0.5 ± 0.001 where the actual sharp interface location is assumed. This assumption is due to the DLR-THETA code approach to model the interface: this is spread out over several computational mesh cells (compare section 4.2.1).

Depicted in red is the simulated case. The graph shows a steady increase from the initial level up to the final fill-level at $700\,s$. Shown in figure 35 is the fill-level over time normalized by the height of the dewar of $h_{dewar} = 0.59\,m$.

This data is compared to the measured values (green line) during the experiment and normalized to the experimental initial and final fill-level. Naturally, experimental data is not smooth and some fluctuations around a steady state level are observed. Interestingly, until around $300\,s$ the simulated increase in the interface progression due to volume expansion in the fluid matches the measured case very well. After this point in time the progression gradient of the two curves deviates until almost up to $700\,s$ where a sudden increase in the measured fill-level is observed that brings it again very close to the simulated data for the last $30\,s$ of the investigation duration of the experiment (the increase in fill-level continuous thereafter).

The reason for the sudden change in the measured fill-level is not known. A problem

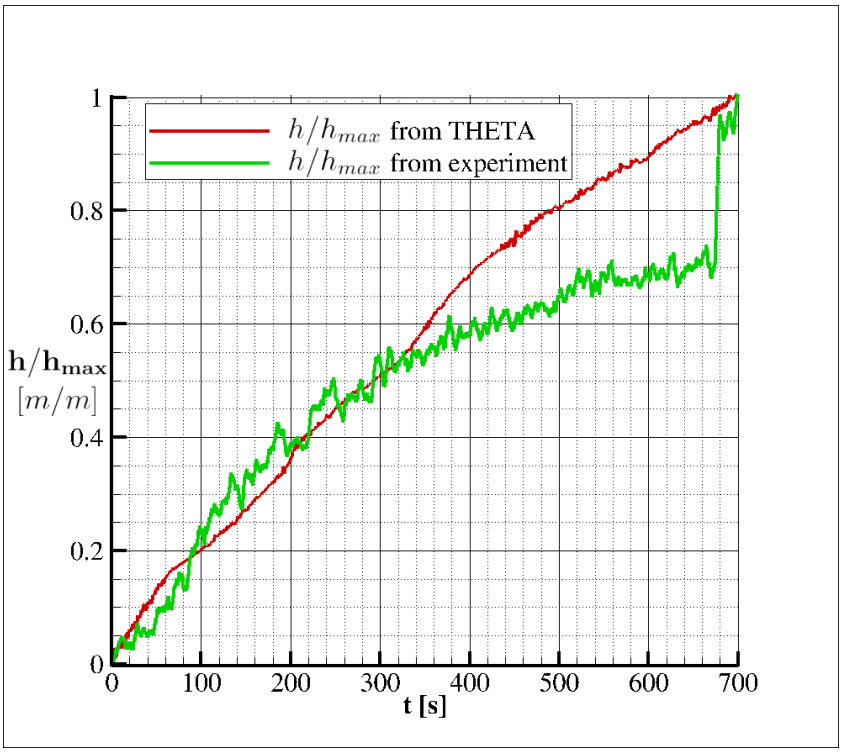

Figure 35: Fill-level change due to phase change calculated from THETA over time normalized by the height of the dewar of $h_{max} = 0.59\,m$.

with the measurements, data recording or a refilling of the dewar could be considered and will be further discussed in section 7.

6.4.3 Mass flow due to Phase-Change

In this section the development of the mass flow due to phase change in the tank is discussed. Similar to the previous sections the data from the experiment performed in Konopka et al. [9] is used to compare it to the simulation by THETA. Figure 36 depicts the development of the mass flow during the conduction of the simulation with a fluctuating, but in general decreasing trend. This decrease in mass flow is also seen in the experimental data. The mass flow is in general in-line with the observed behavior in the experiment although the detailed development could not be recovered in the simulation. The offset close to $200\,s$ in the experimental measurements in figure 36 is due to the pressure control valve. It routes an increased amount of gaseous hydrogen into the dewar in comparison to the stratified case that starts after this initial pressurization (after $200\,s$).

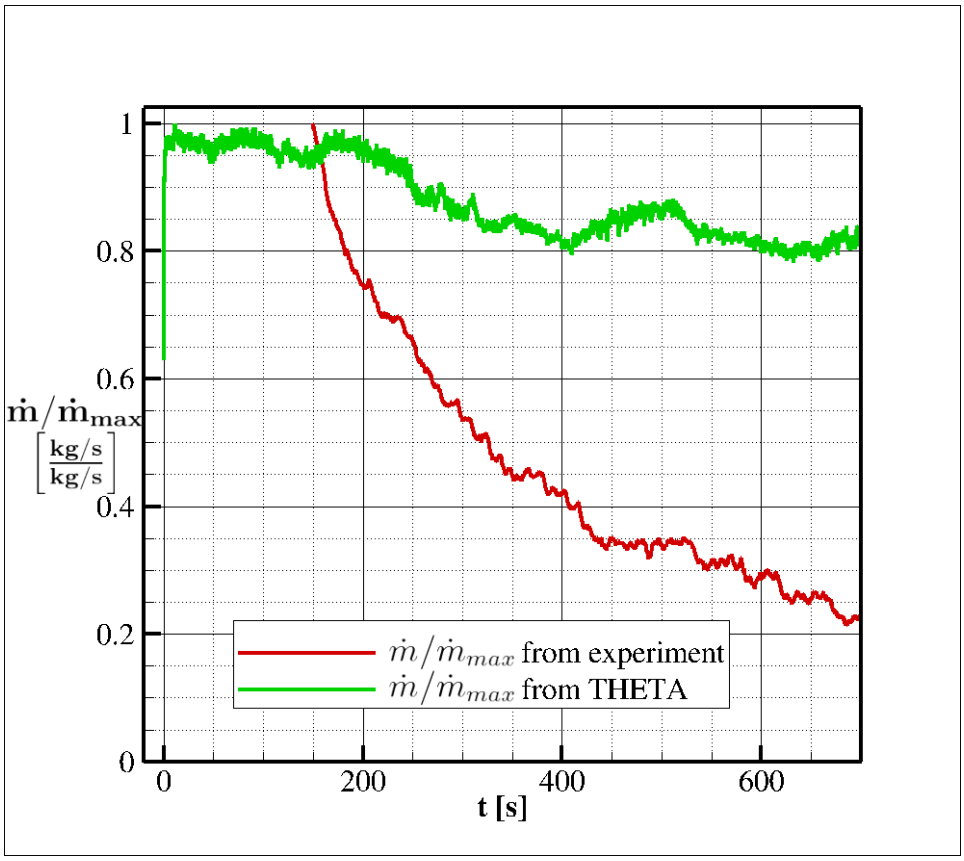

Figure 36: Mass flux due to phase change calculated from THETA over time normalized to the respective maximal value of the experiment and simulation.

Afterwards, the pressure becomes stable and remains at a 3 *bar* level for the remainder of the simulated part of the experiment.

Both, measurement and experiment, follow a decreasing trend although the actual relation to each other is quite different. The corresponding curves were plotted over time normalized to the respective maximal value of the experiment and simulation, respectively. These maximum values are $1.4262 \cdot 10^{-5}\, kg/s$ for the mass flow measured in the experiment and $4.016954 \cdot 10^{-6}\, kg/s$ for the THETA simulation.

There are several reasons possible for the mismatch. More details will be discussed in section 7 in the paragraph Discussion of Mass flow Comparison.

6.5 *Flow-field Investigations*

The following section will investigate the developments in the flow-field. Mainly how velocities and temperature profiles develop at different levels of the dewar over the course of the simulation as well as how the flow-fields behave during the simulation.

6.5.1 Velocity and Stratification Development

At first, this section will investigate the temperature profile development during the progression of the simulation. This will be supplemented by a comparison to theoretical values derived by Ludwig [49]. Secondly, this section will observe the velocity profile at certain positions in the flow-field. Finally, the section will investigate the possibility of turbulence in the dewar during the experiment and hence in the simulation.

Figure 37 shows the temperature development over time at several dedicated monitoring points in the tank. The sensors in the vapor phase are depicted in figure 37b. The submerged monitoring point, measuring temperatures in the liquid phase of the tank, are shown in figure 37a.

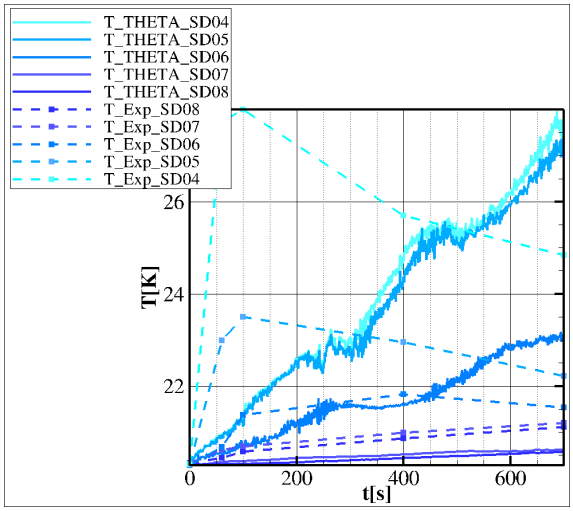

(a) Comparison of temperature profile from THETA over time and several monitoring points along the z-axis for the temperature in the liquid phase.

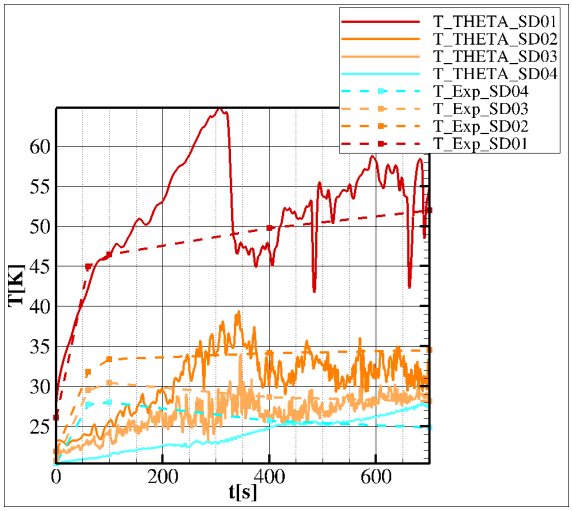

(b) Comparison of temperature profile from THETA over time and several monitoring points along the z-axis for the temperature in the gaseous phase.

Figure 37: Temperature comparison between experiment and numerical solution.

Also included in figure 37 are the experimental data points that were extracted from

the temperature sensor tree that collected, fixed point, time dependant time data for a limited amount of vertical positions and time stamps during the experiment. These time stamps, similar to section 6.4.1, are at $0, 60, 100, 400$ and $700\,s$. The figures show a relatively good agreement for the development of the gaseous phase especially for the monitoring points/sensor at positions $0.4206, 0.4306$ and 0.4656.

On the contrary, they reveal strong deviation for the upper liquid layer that is close to the interface. At least, if one would assume a constant increase of the temperature between $100\,s$ and $400\,s$ where the next measurement is taken. Interestingly, the other measurement times match very well with the simulated temperature points.

For figure 37a this is again different. Here, initial temperatures are lower in the simulation data compared to the two upper most experimental data points. The lower data points are closer to the experimental values especially at positions $0.4106, 0.4056$ and 0.3956 as well as $0.3756\,m$.

According to Ludwig [49] the temperature profile in a stratified liquid $T(z)$ along the z-axis can be estimated via:

$$T_l(z) - T_l = (T_{sat} - T_l)\mathsf{erfc}\left[\frac{H_l - z}{2\sqrt{D_{t,l}t}}\right] . \tag{87}$$

With T_l being the temperature of the liquid in the dewar, H_l its height, t the time of stratification and T_sat the already introduced saturation temperature. The thermal diffusion coefficient $D_{t,l}$ is acquired using equation:

$$D_{t,l} = \frac{\lambda}{\rho \cdot c_p} . \tag{88}$$

For the present case of liquid hydrogen the value is $D_{t,l} = 1.52 \cdot 10^{-7}\,m^2/s$.Used here is erfc, the complementary error function.

This is based on analytical heat transfer models. It approximates the transient heat transfer in a large amount of fluids systems with a constant initial temperature Ludwig [49].

A similar estimation can be performed for the upper GH2 filled part of the dewar. Here the temperature in the ullage can be determined:

$$T_v(z) = T_h + (T_{sat} - T_h)\frac{z_h - z}{H_v}\,. \tag{89}$$

With H_v being the height of the vapor phase and T_h being the temperature at the upper boundary and z_h being the respective height. For the investigated time, $400\,s$ and $700\,s$, this is $T_{h,400} = 49\,K$ and $T_{h,700} = 62\,K$, respectively. This case for the vapor phase is based on a theoretical heat transfer model of the steady-state heat conduction in a flat plate Ludwig [49].

The resulting analytical profiles are shown in figure 38. The two equations are distinguished by different color as they do only apply in the respective phases as pointed out the figure legend.

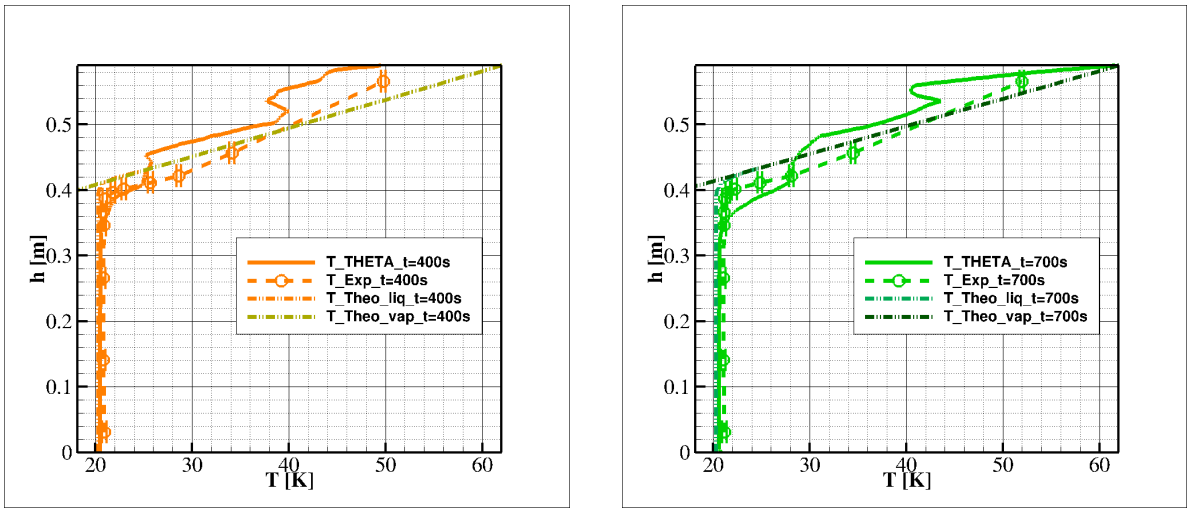

(a) At $400\,s$. (b) At $700\,s$.

Figure 38: Temperature comparison between experiment, analytical profile (for vapor and liquid) and the numerical solution with THETA.

In figure 38 the previously presented figures for the temperature development (figures 32b and 33) are supplemented with the analytical solution of the liquid and vapor phases. Those were derived from equation (87) and 89, respectively.

The figures confirm the general match of the simulation with the experiment and the supplemented analytical solution. For the bulk fluid the analytical solution is actually in better agreement with the simulation, compared to the experiment. For the interface area this trend reverses as the analytical solution and the experiment at $700\,s$ are qualitatively

closer together. Also for the vapor phase, the ullage, the analytical curve represents an ideal case of a temperature profile with a constant gradient increasing from the interface to the upper part of the dewar. It corresponds also with the simulated and experimentally acquired results, although the gradient differs in all three cases.

Figure 39 presents the velocities of the upper most monitoring point in x, y and z-directions. In general it is observable that the up- or downward motion of the gaseous fluid in the top of the tank is negligible compared to the velocity in horizontal plane of the measurement. Up until about $310\,s$ the motion of the vapor is relatively slow, in peaks of about a third of the maximum and chaotic compared to later times. At this time a larger, possibly rotational motion is starting that decreases with ongoing simulation time. After about $500\,s$ the assumed rotation fades again into a more unorganized motion up until $700\,s$ at the end of the simulation. Further below the discussion of figure 44 will explain further possibilities of motion in this area.

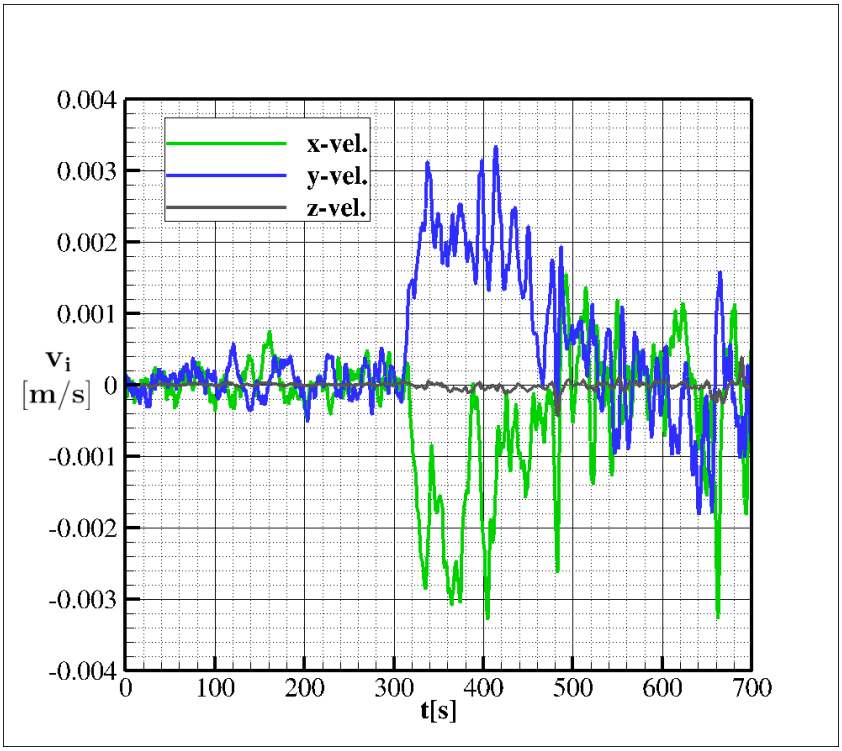

Figure 39: The velocities profile from THETA over time at monitoring point SD01 (see table 7).

In contrast, figure 40a for the monitoring point at SD02 ($h_{dewar} = 0.4656\,m$) and similar figure 40b at SD03 ($h_{dewar} = 0.4306\,m$) show a more chaotic and variable motion for

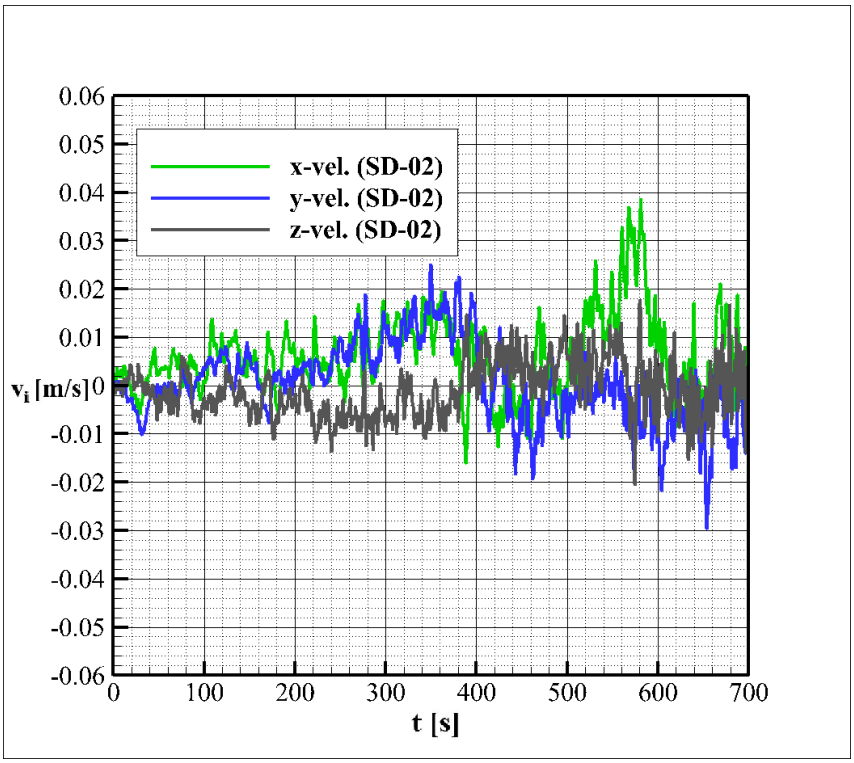

(a) Velocity profile over time at SD02.

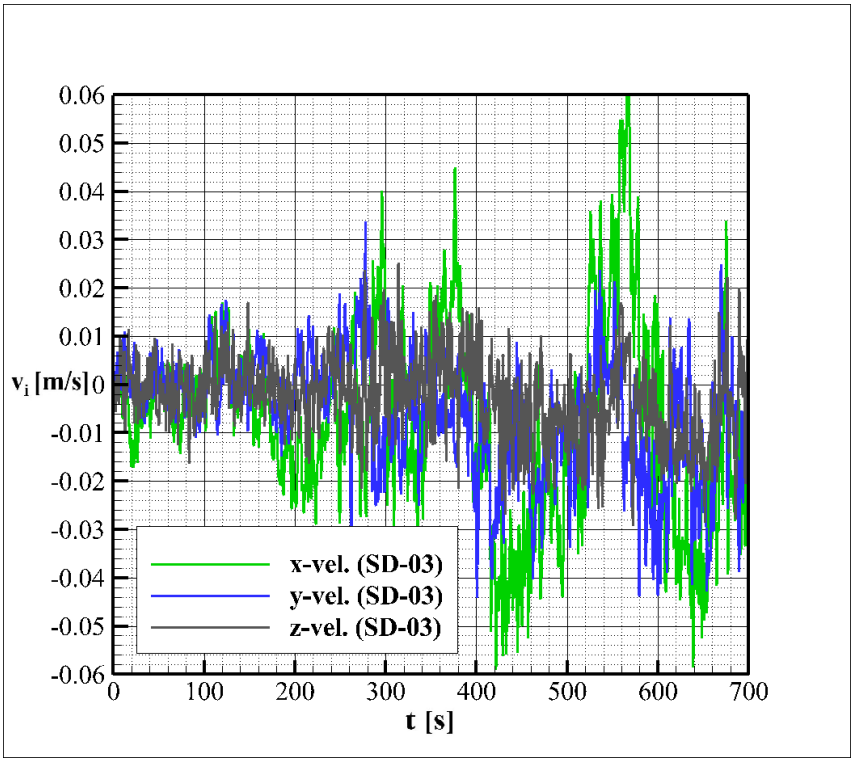

(b) Velocity profile over time at SD03.

Figure 40: The velocities profile from THETA over time at monitoring point SD02 & SD03 (see table 7)

the simulation. Figure 40a illustrates an overall mathematical positive rotation (positive x and y velocity component) until 400 s, which then switches to a negative rotation afterwards (negative x- and y-component as well as negative y- with positive x-component). The flow is generally downwards until at later times after 400 s when it switches to an upward motion to return to a downward motion again towards the end of the simulation.

At the lower point in the dewar at SD03 ($h_{dewar} = 0.4306\,m$), which is close to the interfacial region, the general motion is again different. First, compared to figure 40a, the maximum magnitude is twice as high as at SD02. Secondly, the motion is more variable and towards the end of the simulation, the up- and downward motion changes more frequently than compared to the simulation monitoring point SD02.

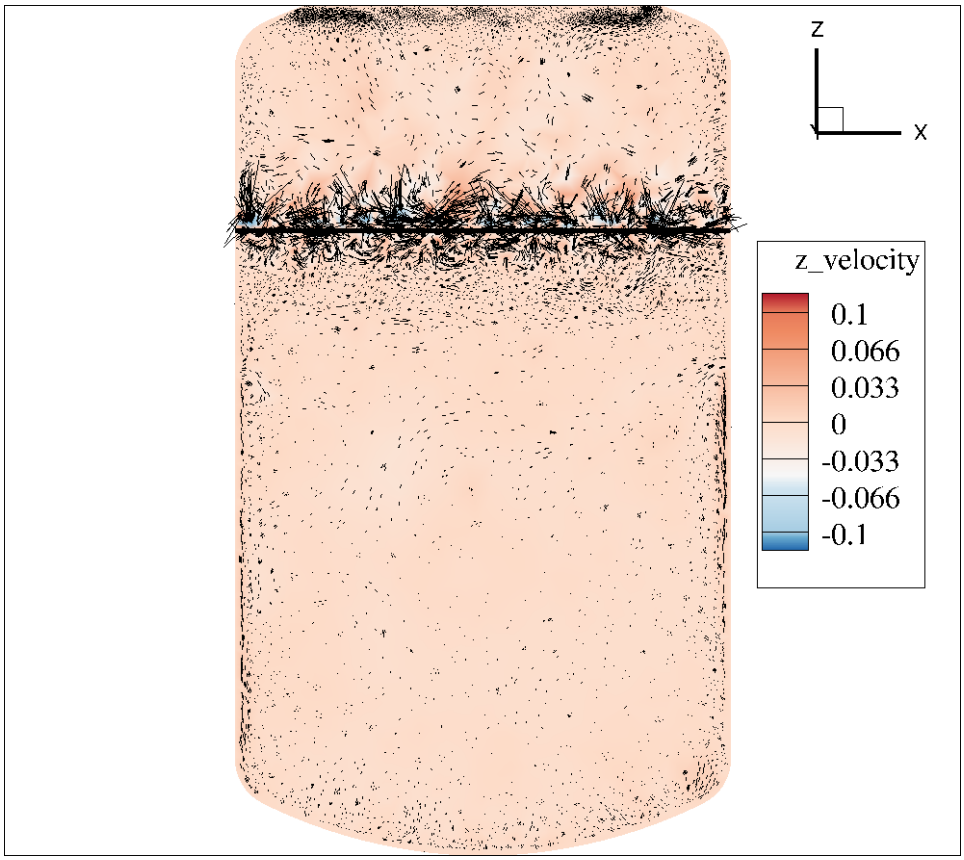

Figure 41: A cut through the z-plane with uniform velocity vectors at 700 s.

In order to get a general overview of the motion within, figure 41 can be consulted. The figure displays a cut through the dewar as a z-plane, plotting the z-component of the velocity, overlapped with the uniform vector field in this plane of the dewar at 700 s

simulation time. For reference a black, solid line depicts the liquid-vapor interface to better distinguish the two regions in the dewar very clearly visible is the strong uplift of liquid at the walls of the dewar when hotter, lighter LH2 flows upwards to the stratified layer. Here, the hotter liquid collects and floats on top of the cooler bulk liquid.

Also visible is a stronger motion above the interface where GH2 is pulled upwards by the effect that is caused by the heated gas at the hot top of the ullage. This gas is sinking towards the cool interface at the walls of the dewar, setting this flow into motion.

Compared to these areas of stronger motion, the cool bulk is generally less mixed due to a more uniform temperature distribution that is colder than the dewar walls and the interfacial region.

To further visualize the flow in the ullage a cut at $z = 0.575\,m$ was produced and is shown in figure 42. Visible is indeed a rotational motion in this cut. Coming from walls vapour is flowing towards the center and collecting at nodes (black concentrations of stream traces).

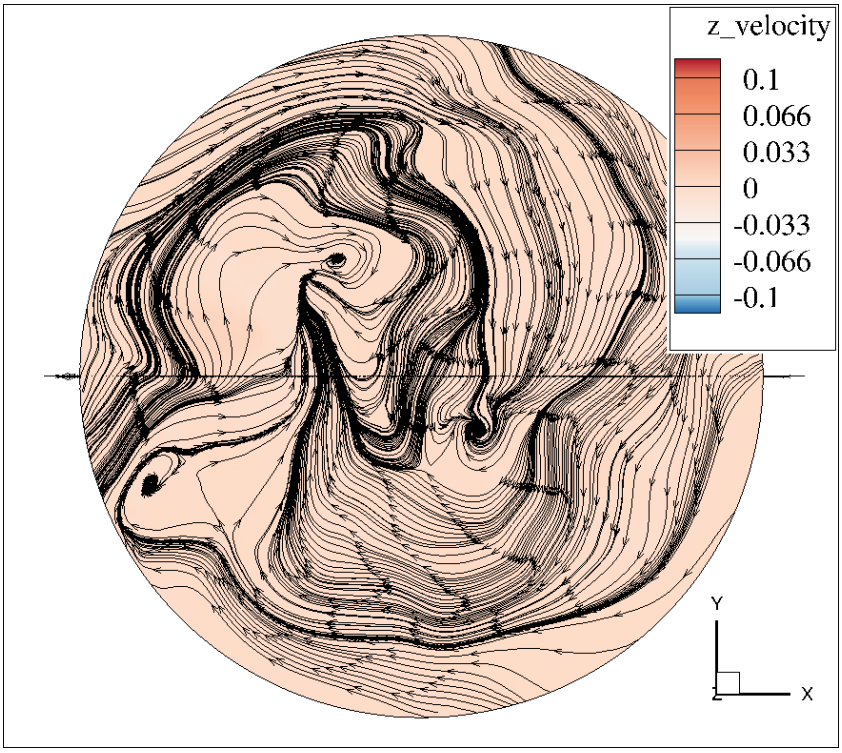

Figure 42: A cut through the $x-y$-plane with velocity stream traces at $700\,s$ and at $z = 0.575\,m$.

As mentioned before, the assumption is observable that the up- and downward mo-

tion of the gaseous fluid in the top of the tank is negligible i.e. z-velocity is approximately $0\,m/s$.

6.5.2 Characteristic Numbers of the Flow

The prominent characteristic numbers for stratified flows are the PRANDTL number Pr, which can be estimated via:

$$Pr = \frac{\mu_l \cdot c_{p,l}}{\lambda_l}\,. \tag{90}$$

Furthermore, the RAYLEIGH number Ra is of importance (as defined in equation (86)).

For the present stratification experiment the characteristic numbers are printed in table 9. For this the values for the dynamical viscosity can be calculated according to:

$$\nu = \frac{\mu}{\rho}\,. \tag{91}$$

Value	*liquid*	*vapor*
$Pr\ [-]$	1.309	0.484
$Ra\ [-]$	$2.9449 \cdot 10^{12}$	$3.2517 \cdot 10^{9}$
$\lambda\ \left[\frac{W}{mK}\right]$	0.1044	0.0464
$c_{p,l}\ \left[\frac{J}{kgK}\right]$	9693	10686
$\mu\ \left[\frac{Pa}{s}\right]$	$1.37 \cdot 10^{-5}$	$2.1 \cdot 10^{-6}$
$\nu\ \left[\frac{m^2}{s}\right]$	$1.93 \cdot 10^{-7}$	$1.7692 \cdot 10^{-6}$
$L\ [m]$	0.433	0.157
$\Delta T\ [K]$	7.36	33.80

Table 9: Values of the Pr and Ra characteristic numbers and the used parameters and the generally defined gravity value on earth $g = 9.81\,m/s^2$.

In figure 43 a regime diagram for different forms of flow is shown (taken from Krishnamurti [11]). It plots the characteristic numbers of the PRANDTL number Pr (defined in equation (90)) versus the RAYLEIGH number Ra (as defined in equation (86)) and allows to assume a flow regime for the test under investigation by examining the values of the mentioned numbers.

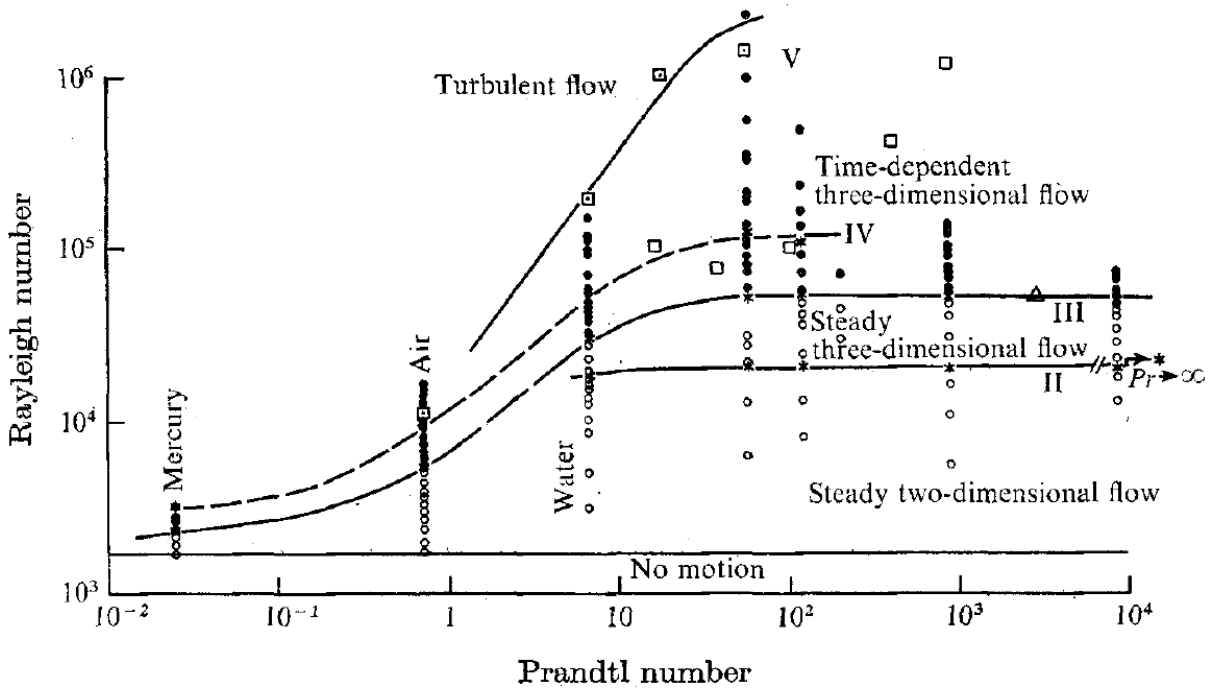

Figure 43: Regime diagram. white dot, steady flows; black dot, time-dependent flows; star, transition points with observed change in slope; square, Rossby's observations of time-dependent flow; square with dot, Deardorff and Willis [10] observations for turbulent flow: triangle, Silveston's point of transition for time-dependent flow. Reprinted by permission from Cambridge University Press from [11], COPYRIGHT (1973)

Transition from laminar to turbulent flow is assumed to happen at RAYLEIGH number Ra 10^9. This was visualized by Ratner et al. [8] (see figure 2 in Ratner et al. [8]). This also makes it clear that a transition from laminar to turbulent under normal gravity condition (which applies for the present experiment) already happens at very low temperature differences. On one hand, for the liquid at $Pr = 1.309$ a $Ra = 2.9449 \cdot 10^{12}$ is reached, well above the critical transition RAYLEIGH number. On the other hand for the vapor at $Pr = 0.484$ a $Ra = 3.2517 \cdot 10^9$ is reached, which is already in the transitional region.

As the value of the characteristic numbers are suggesting the flow within the gaseous phase is close to being turbulent or a least in the area of transition. A further indicator is the velocity development shown in figure 39 in section 6.5.1.

In section 6.5.1 it was pointed out that the strongest motion happens in the vapor

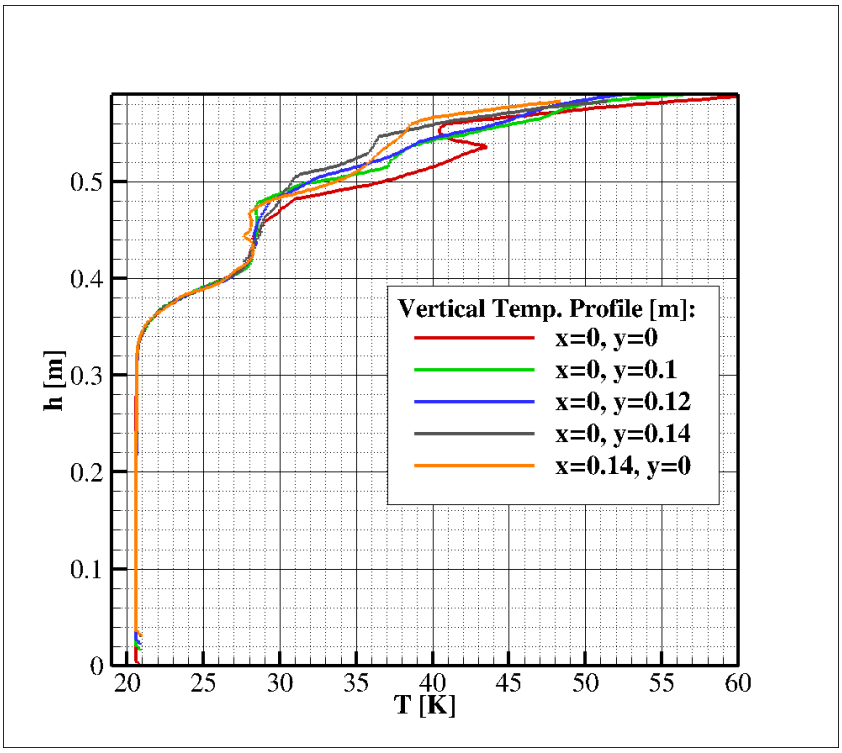

Figure 44: Comparison of several vertical (along the z-axis) temperature profiles from THETA at several places in the dewar, away from the centerline.

phase, the ullage, of the dewar. An additional indicator is figure 44 where the temperature profile in the dewar is plotted for the complete height of the dewar. The mapping of 0 is the already discussed position of the sensor tree (see figure 26b and table 7 for a reference to the exact position). Mappings 1 to 4 indicate different position on the x-plane along the y-axis that were extracted from the simulation.

The temperature profiles match very closely, independent of the position in the simulated dewar. This clearly shows how stable and stratified the liquid bulk is. In contrast, the temperature profiles in the ullage zone of the dewar deviate visibly from each other, indicating that the ullage gas is in motion and by no means stratified. Indeed the vapor profile is different for several positions in the vapor bulk as the shown kink does not appear anywhere again (compare figure 44). The rest of features remain more or less intact. This is another indication that the vapor phase is indeed not a stable homogenous phase.

Especially interesting is the temperature rebound in mapping 0 (red line), where at a height in the dewar of about $0.55\,m$ a reduction in the temperature is visible. This happens despite the increasing trend of temperature towards the top of the dewar. This

rebound is not as prominent as in the other temperature profiles (mapping 1 to 4).

This is a possible reason for this could be a concentration of cooler gas in the center of the ullage as the gas is heated at the top of the dewar as well as at the side walls of the ullage area. This means, that in the top of the ullage the gas is heated over time building up a layer on top of the vapor phase that is increasing over time. This is visible for example in figures 31 and 32, where the temperature profile shows raising temperatures over the simulation time. In addition to this increasing temperature in the top of the ullage, since the sidewall is also heated, a raise of temperature there is also observed. Thus, adding vapor to the temperature layer at the top that possess the same temperature. This favours the assumption of a layer build-up, which is supported by the negligible up- or downward component of the velocity profile shown in figure 39.

When looking at the temperature profiles in figure 44 it can be observed that from close to the sidewall towards the center of the dewar (lower y, first 4 mappings) the temperature is decreasing. This suggests that in the center of the dewar a pocket of cooler vapor remains, which is not yet heated to the same temperature from the top, nor the sidewalls.

The sketched process that could be considered of being close to turning into a turbulent flow. Still, a turbulent model was not considered to be used for the duration the simulation of the dewar, especially since it was discussed by Konopka et al. [9] that the involvement of a turbulence model did not result in any difference of the observed parameters, mainly temperature, in the liquid phase. It is to be noted that the gaseous phase was not discussed there!

7 Conclusion and Outlook

Discussion of Model Development and Implementation The presented work started from the baseline of an isothermal two-phase flow implementation that was described in section 4.2 and implemented by Gauer [60]. After a thorough literature study, that is outlined in section 2, an approach was chosen that was suitable in the already provided THETA and VOF framework. Expanding on this isothermal code this work included the possibility to use the existing temperature model in combination with the VOF approach. Thus, both fluids are able to have temperature dependant density values according to the ideal gas law or the Boussinesq approach (see section 4.3.3).

Following this idea, the first step of the implementation of a non-isothermal two-phase model in THETA is the introduction of a phase change model including the respective source terms in the mass conservation equation (equation (26)). To complete the implementation a way to redistribute the source terms was introduced and additional required source terms for the energy equation where implemented (compare to equation (60)).

The resulting changes were then tested and validated using basic test cases and a complex application case. These tests are discussed in the following.

Discussion of the basic Validation Test Cases In section 5 three main numerical experiments were discussed: the Stefan-, Sucking- and Scriven-problem. For the first two the results were in very good agreement with the considered analytical solution. Figure 11 point this out clearly for the Stefan problem, which is regarded as the initial test to validate phase change CFD codes. The error for the problem ranges from $+4\%$ at the beginning to -2% at the end of the simulation, showing a generally satisfying match to the analytical solution presented in section 5.

As quickly presented in this section, the Stefan problem was used as a basic, fast processing example to evaluate the correct implementation of the phase change addition to the THETA code. After some initial investigation with the approach by Wróbel [31] that was yielding a satisfying result a different approach to introduce a source term for phase change was used. The resulting changes in the velocity profiles were presented in figure 14. One sees clearly that for a stable and valid solution the implemented approach using a smoothed-out source-term that is based on the temperature gradient in the interfacial region, was the technical choice at hand that yielded the most promising results for the Stefan problem.

Furthermore, for the Sucking Interface problem, the selected modeling approach is able to produce results that fit the expected, analytical outcome to a high degree. The larger difference in the interface region vanishes during later times below 1% for a fair amount of simulation time (basically surpassing this limit after roughly $0.38\,s$). One possible reason for the discrepancy is thought to be the overestimated mass flux due to phase changes that are well above the initial analytical solution, but are matched relatively fast after about $0.05\,s$. Since the temperature gradient in the interfacial region is very large a different interpolation length (parameter d_{int} in equation (61)) might improve the initial solution but would not catch the later gradient when the interface temperature gradient is further stretched out in the liquid phase. The investigations show the overall spatial temperature profile is matching the analytical solution well and also a detailed look into the interfacial region reveal a satisfying match between the simulation and the theoretical estimated value for the temperature. Only the profile near the interface is deviating stronger from the reference value (in this case the saturation temperature of the vapor), a fact that supports the theory of an initial overestimation of the temperature gradient and thus the evaporation mass flux.

For the Scriven Problem, the expansion of a vapor bubble in an overheated liquid, was simulated to a lesser success. The main issue here was the missing stability of the solution due to the surface tension. As discussed in section 5.3 a valid solution of the test case was only possible with a fraction of the actual surface tension of the fluid. Changing the liquid under consideration e.g. to LH2, which has much lower surface tension, did not improve the result since the surface tension itself is not the measure for stability, but in which relation it is with viscosity and density. Meaning for other fluids the problem remains despite a very much reduced surface tension, suggesting a stability issue indeed. Eventually, the investigation of the Scriven Problem was concluded with 10% of the realistic surface tension to find a compromise between the stability of the simulation and an expansion of the simulated bubble. Unfortunately, due to the reduced surface tension, the pressure inside the bubble was not at a realistic level and thus, the pressure drop over the interface was neither resulting in a reduced push against the fluid from inside the bubble, which finally resulted in the observed, reduced bubble growth. Furthermore, the surface tension is not a parameter of the analytical solution, only for the numerical one. For the analytical solution, only the density and heat transfer parameters are playing a role (see section 5.3).

Concluding from the three basic test cases, it is reasonable to assume a successful implementation of the presented phase change model into the existing, two-phase VOF modification of the DLR THETA code. The remaining open issue is the interplay between the phase change source term, that is smoothed over a region on both sides of the liquid-vapor interface, and the surface tension implementation that is smoothed over the unsharp interface of the VOF implementation.

Discussion of KOALA Vertical Temperature Profiles Comparison Section 6.4.1 showed the comparison of the temperature profiles in the experimental and simulation case. A discussion of the results will be performed in this paragraph.

The initial conditions were put as close to the known experimental set-up as possible in order to match the initial condition of the dewar as similarly as possible. The initial temperature was fitted well as figure 30 demonstrates and the simulation was set-up as described in section 2.2 resulting in static start condition for the simulation as shown in figure 29. Although these conditions could be fit correctly to the experiment, the history of the filling and pressurization could not be reflected in these initial conditions, thus, not catching the initial motion caused by filling the dewar with pressurization gas or the initial motion of the fluids, due to the already existing temperature gradients. Due to the incompressible nature of the used solver, no simulation of the ramp up of pressure was technically possible.

In figure 31 it was visible that the simulation is not developing the same temperature distribution at the same speed as the experiment i.e., for the initial phase of the simulation the temperature is underestimated. In these cases the experiment reaches a higher temperature at the same height of the dewar. Thus, the LH2 heats slower in the THETA simulation. In contrast it could be shown, that in figure 31a and to a more visible extent in figure 34b the temperature profile in the liquid is comparatively close to the experiment. The subsequent development up until $400\,s$ is not comparable as the experiment does not provide temperature readings for this period. This trend is reverted for the later times of $400\,s$ and $700\,s$, as shown in detail in table 8, where the error in the ullage of the dewar is decreasing from its initial high values to a lower level whereas, the error in the fluid is increasing over the simulation time.

A clear cause of these discrepancies could not be identified. Some causes will be discussed in the following sections, mainly an unknown role of turbulence, since the fluid is in the transition region from laminar to turbulent for LH2 in the gaseous phase. Although the influence was deemed minimal in Konopka et al. [9], this might be different for the full 3D simulation performed in this presented work. For more details see paragraph "Discussion of Characteristic Numbers of the Flow" of this section. It has been pointed out in paragraph "Discussion of the basic Validation Test Cases" of this section that the surface tensions caused issues when simulating the Scriven problem. In the case of the KOALA experiment this should not cause any issues as the experiment was performed under nor-

mal gravity conditions where the capillary forces should play a minor role. Due to this gravity environment phase change effect at the boundary-interface intersection should be similarly negligible in the KOALA experiment.

Discussion of Fill-Level Development The fill-level comparison was shown in section 6.4.2 and a discussion will follow in this paragraph. The parallel plotting of the simulated and experimental result revealed an interesting deviation starting after 330 s until shortly before the simulation ends (see figure 35).

Therefore, several options that could cause such a deviation in the measurement of the experiment are possible. Suspicious is the initial match between the two lines. Later, the jump in the experimentally measured values makes a good comparison difficult.

Of course one could consider experimental issues as a reason. For example the measurement technique could have yielded wrong results after the deviation in the two curves, with a sudden jump back to the actual measured value after roughly 670 s. This could be due to a fluctuating offset or gain correction value in the fill-level measurement sensors. Also the rapid increase of the fill-level, almost a step, could suggest problems with sensors, as the fill level increase is roughly in the order of 25% in a few seconds. during the remaining measurements the fill-level was only changing by a few percentages.

Other experimental effects are feasible as well e.g. an additional filling of the tank. In contrast a rise in pressure due to increased condensation is not identified to have happen at this time of the experiment.

Of course on the other hand, the simulation could start to over predict the rise of the liquid (if one ignores the match at the end of the comparison where the two measured or respectively simulated characteristic rises) after the initial match, possibly due to an over estimation of the temperature in the bulk interface region.

Discussion of Mass flow Comparison In section 6.4.3 the evolution of the mass flow in the experiment and the simulation was presented. The comparison revealed that the initial mass flow rate that is supplied into the dewar in the experiment due to condensation and the need to keep the pressure at a value level of 3 bar is not matched by the simulation.

But as the pressure development of the experiment shows in Konopka et al. [9] (figure 4a), the pressure development is only stable after about 200 s after the initialization of the simulation where LH2 is still supplied to increase the pressure to the experimental level of 3 bar. Thus, only after this initial inflow of pressurization gas the pressure is stable, and the control valve only supplies the amount that is condensing at the interface. This reasoning could explain the found difference in the mass flow rates between simulation and experiment. Furthermore, this effect could also be one of the drivers as to

why the initial temperature profiles in the THETA simulation are off the experimentally evaluated values in the beginning, whereas the influence of the inflow of the pressurization gas might vanish as the simulation progresses.

Discussion of Velocity and Stratification Development Section 6.5.1 was investigating how the velocity was developing in the parts of the dewar, liquid bulk and gaseous ullage. Additionally, the development of the temperature with time was investigated and the profiles were compared to theoretical results. Especially figure 37 provided interesting results when compared to the temporal development of the temperature in the simulation with the timely evolution of the temperature of the measurement points on the sensor array in the dewar. For the vapor phase this development seems to be well predicted by the THETA simulation with the exception of the upper most monitoring point, which is located a short distance under the top of the dewar. Its temperature is increasing rapidly following the measurements at the monitoring points up to $100\,s$, where they align effectively with predictions by THETA. This trend continues until shortly after $300\,s$, where the temperature is sharply dropping, undershooting a linear fit between the monitoring points at $100\,s$ and $400\,s$, but then oscillating around a similar fit up to $700\,s$. Eventually, the temperature is only a few degree above the measured value. Interestingly, the sharp decline in temperature corresponds with the sharp increase in the x and y components of the velocity field at this very measuring point (SD01) that ramps up shortly before $320\,s$ to keep up the motion until $500\,s$ after which it is declining again. This strong temporal succession of the increase in velocity and decrease in temperature suggest that there is a connection of the two events where the increased motion starts distributing the accumulated heat much more efficiently, thus increasing the temperature at this measuring point.

The situation in the bulk liquid is different. Here the two lowest monitoring points that were investigated (SD06 and SD07) predict a simulated temperature only a few tenths of a degree below the actual, experimental measurements with the general trend of increasing temperature with advancing time. In general the same can be observed for a third of the five monitoring points of figure 37a. In contrast the next two higher monitoring points, the last two in the liquid, just below the interface, show a reversed match i.e. where the THETA predicted temperature is steadily increasing with time. Interestingly, the temperature of the experiment is increasing at first, to only drop after the first $100\,s$ (if assuming a linear fit between the measurement points at $100\,s$ and $400\,s$). This is a behavior that could not be replicated with the simulated dewar, which suggests that after an initial accumulation of hotter liquid below the interface, a stronger mixing in the liquid is taking place, which increases the temperature in the lower parts of the bulk. A process

that was not observed at this strength in the simulation.

On top of the aforementioned investigations in this section, an analytical comparison was performed comparing a model derived by Ludwig [49] to the experiential measurements and the THETA simulations. This comparison was documented for the two later measurement times at $400\,s$ and $700\,s$, respectively. In this context the analytical solution can be considered a general trend and that the temperature in the cylindrical dewar will develop when a certain dimension is given, and the used liquid is specified. One interpretation of the result of this development is a centerline for the temperature profiles because at a certain height (the y-axis in figure 38) the measured and simulated temperatures are below or above this trend line. In the bulk this analytical temperature is closer to the simulated temperature, whereas in the ullage the zone close to the interface has a temperature above the analytical temperature. This changes at a height of about $0.5\,m$ when the analytical temperature is above the measured one. The simulated temperature development is always below the one predicted by the analytical model. These general observations are visible in both sub-figures for $400\,s$ and $700\,s$.

The analytical solution also matches the experimental result better from a general point of view in the ullage part of the dewar, thus suggesting that the simulation was not able to match the real-world energy generation or distribution in the dewar. On the other hand, the analytical solution is overestimating as it cannot account for several real-world effects like friction, energy loss over the dewar boundaries, possible turbulent mixing and radiation among other effects that play a role in the experimental set-up.

The investigation of the velocity fields show a strong upward flow of heated liquid at the dewar walls as well as strong motion of the vapor in the ullage section of the dewar. As will be discussed in the next part of the discussion this could be propelled by the transition to turbulent flow in the ullage.

Unresolved is the question why the initial temperature in the upper liquid is so high at the start of the experiment when plotting the temperature at the sensor line over time in figure 37a in section 6.5.1. A conceivable circumstance is that inflow of pressurization gas reported in paragraph "Discussion of Mass flow Comparison", and thus the increasing pressure, is changing the saturation temperature in the liquid.

Discussion of Characteristic Numbers of the Flow In the previous section 6.5.2, the characteristic numbers of the flow were discussed. Similar to the PRANDTL number (LH2: 1.272 to GH2: 0.484) the RAYLEIGH number is different in the liquid and the vapor. In the current case (LH2: $3.1061 \cdot 10^7$ to GH2: $2.7394 \cdot 10^9$) the liquid is far below the turbulent transition level of Ra 10^9. On the contrary this is not the case for the vapor phase of GH2, which is well in the region of initiation of transition to a turbulent flow.

Right from the beginning, the use of a turbulent model for the simulation was excluded since the main focus was set to the liquid phase where stratification occurs. Also, investigations by other groups on the same simulation (see Konopka et al. [9]) had strong indications that the addition of a turbulent model in the processing did not have a strong impact on the results. Furthermore, although it is possible to use two turbulent models, the standard $k-\omega$ and the $k-\omega$-Shear Stress Transport model, in THETA no validation data on the models are available for a two-phase flow. Although the general correctness of the models within THETA is well established Lambert et al. [66].

In hindsight of course, it is possible that the inclusion of a turbulence model could yield better results in the gaseous ullage and give a more strongly mixed zone of GH2. Thus, being able to fit the experimental results even closer. This could possibly also improve the transport of energy from the interface region into the ullage, which would overspill the temperature in the interfacial region, which is over predicted compared to the experimental results. Compare to figure 32b or figure 34.

As of writing of this work the THETA two-phase implementation was not validated on a smaller test-case for the use of the turbulent models that are verified to work with the implementation of the two-phase flow. A future work could therefore perform a validation experiment and if successful redo the simulation of the KOALA stratification experiment. Performing such a calculation, which might come at the additional cost of increased computation time, would support a better understanding of the temporal and spatial differences in the ullage and how the flow within it develops with progressing simulation time.

As section 6.5.2 demonstrated, especially the ullage is far from being a static body of fluid, highlighting in contrary that the KOALA test case consists of two separated flow regimes with laminar in the liquid bulk and near turbulent flow in the vapor ullage.

Summary & Outlook In the presented work the multiphase model in the THETA code was extended for phase and energy transitions. This was done by implementing the model utilized by Kunkelmann [6]. Verification and accuracy assessments, based on basic test cases showed their fundamental applicability. The validation of basic test cases revealed, that the solver, with the during a previous work implemented VOF approach by Gauer [60], is sensitive to high surface tension in fluids with high density ratios, as is the case for the investigated fluids of water ($\rho_1/\rho_0 = 1605$) and LH2 ($\rho_1/\rho_0 = 60$). Eventually, this behavior is not deemed critical for the conduction of the large stratification simulation of the KOALA test case. In the KOALA case the interface is flat, and the buoyancy effect dominates over capillary forces (in contrast to the Scriven problem).

Overall, the simulation was able to predict the evolution of a stratification experiment to a satisfying degree, although the detailed investigation in section 6.4 of the presented work showed that some deviations exist. Nonetheless, the general behavior was caught. A deeper investigation also revealed some unexplained measurements in the compared experimental data e.g. the offset measured in the inflow of pressurization gas and the increased temperature in the liquid at the beginning of the measurements. Furthermore, the reason for the sharp step in the fill-level of the experiment at the end of the investigated time-frame remains unresolved. These differences were discussed in detail in the current section 7.

During the cause of this work some areas of potential improvements were identified to increase the applicability of the presented approach to more use cases. Some areas of improvements remain to be investigated in future developments that might use a different CFD solver, similarly developed at the DLR but using different numerical approaches when compared to the TAU and THETA codes. These potential areas for development are discussed below:

Improvements & Lessons Learned This work primary focus was to solve the problem of phase change in the context of the established THETA solver. Therefore, no changes in the VOF implementation where conducted. This could be a field of investigation to improve the stability of the solver with respect to the discussed issues with the Scriven problem. One approach could be to use the now implemented estimation of the interface position to use a sharp VOF approach that is no longer smearing the interface. The theory of these approaches was discussed in section 4.2 and to a greater extent

in Gauer [60].

To improve the assurance of the prediction of the phase change mass flow, a dynamical estimated interpolation length based on quality measures e.g. the change in temperature between bulk and ullage could be foreseen. For example, if this overall gradient is high the calculation of the temperature gradient for the phase change mass flow should use a smaller interpolation length and vis-versa.

The paragraph "Discussion of Characteristic Numbers of the Flow" pointed towards the laminar to turbulent transition character of the investigated flow in the dewar. Thus, an investigation and validation of the turbulence models implemented in the THETA code and how they interact with two-phase VOF model would be a useful expansion of the current state of the simulation tool.

In the future the implementation of the presented approach into a compressible solver like CODA (that is planned as a successor of the DLR THETA code) should be preferable since this will allow the simulation of a larger spectrum of test cases and also consider pressurization scenarios that precede the actual stratification test case like KOALA, that was investigated in this work. This would improve the starting conditions of the actual stratification phase and therefore increase the comparability of simulation and experiment.

Appendix

A The THETA Phase-Change Expansion Overview

The expansion of the THETA VOF functionality is based on THETA version 2017.1. Changes were mainly done in the files *model_vof.c* and *model_eng_temp.c* with minor changes in *smoother.c* and in files where ρ_0 or ρ_1 are used, since due to the implementation of the Boussinesq approximation, the previously static values for the densities are now indexed fields that point to temperature dependent densities values at every dual-grid point.

The scope of the parameter input was expanded with the values in table 10. Furthermore, the table includes notes and recommendations as to what these new items provide. It is indicated where the new parameters follow the definition from the THETA user guide [67], by only providing input for the second fluid.

The code can be produced with the standard THETA *Makefile* and requires no further considerations when building it.

The model selections, which have to include the choices *VOF*, *MOM_SRC* and *ENG_TEMP* in order to function properly, have to be taken into account. It is also possible to use the recent expansion of the turbulence applicability to two-phase flows. Furthermore, the boundary conditions "isotherm" and "fixed flux" can be applied with the standard usage as described in the THETA user guide [67]. The conditions "real wall" remains unusable at the moment.

Please be aware that the Equation of State (EOS) is very sensitive to its initial conditions and requires special care! Further information regarding this implementation can be found in the report accompanying this code.

Parameter name	Type	Range	Default	Note
Specific heat capacity second fluid	float	$0 \leq x$	$4216.0\,J/kgK$	Same definition as for standard Theta parameters; default for water in $\left[\frac{J}{kgK}\right]$
Thermal conductivity first fluid	float	$0 \leq x$	$0.025\,\frac{W}{mK}$	Thermal conductivity value for the specified fluid in $\left[\frac{W}{mK}\right]$; default for water
Thermal conductivity second fluid	float	$0 \leq x$	$0.679\,\frac{W}{mK}$	The thermal conductivity value for the specified fluid in $\left[\frac{W}{mK}\right]$; default for water
Equation of state (Linear/Ideal gas) second fluid	string	-	Linear	Specifies for the second fluid which EOS shall be used; Same definition as for standard Theta parameter
Specific gas constant second fluid	float	$0 \leq x$	461.5	Same definition as for standard Theta parameter; default for water in $\left[\frac{J}{kgK}\right]$
Expansion coefficient second fluid	float	$0 \leq x$	$214.0e^{-06}$	Thermal expansion coefficient (isobaric) $[-]$
Reference temperature second fluid	float	$0 \leq x$	$300.0\,K$	Same definition as for standard Theta parameter; default for water in $[K]$
Saturation temperature	float	$0 \leq x$	$373.15\,K$	The value of the saturation temperature at the specified reference pressure in $[K]$; default for water at $p = 1\,bar$
Latent heat	float	$0 \leq x$	$2.257e^{+06}\,Jkg$	in $\left[\frac{J}{kg}\right]$; default for water
Stencel	float	$0 \leq x$	$0.0\,m$	It is recommended to choose three mesh cells (or an average value of three cells) as the value for this parameter; in $[m]$
Max. Iteration Smoother	int	$0 \leq x$	20	The value can be changed to account for complex interface shapes with higher iteration numbers for the smoother

Table 10: Additional input parameter of THETA phase-change model.

References

[1] NASA Arianespace, ESA. Jwst stowed inside the ariane 5, 2009. URL https://www.esa.int/ESA_Multimedia/Images/2009/10/JWST_stowed_inside_the_Ariane_52.

[2] ESA. Ariane 5 es galileo orbital transfer, 2016. URL https://www.esa.int/ESA_Multimedia/Images/2016/11/Ariane_5_ES_Galileo_orbital_transfer.

[3] *Phase Equilibrium*, pages 159–185. Springer US, Boston, MA, 2002. ISBN 978-0-306-47061-5. doi: 10.1007/0-306-47061-6_9. URL https://doi.org/10.1007/0-306-47061-6_9.

[4] Hans Dieter Baehr and Stephan Kabelac. *Thermodynamik*. Springer, Berlin, Heidelberg, Heidelberg, 15 edition, 2012. ISBN 978-3-642-24160-4.

[5] Y.A. Çengel and M.A. Boles. *Thermodynamics: An Engineering Approach*. McGraw-Hill series in mechanical engineering. McGraw-Hill Higher Education, 2006. ISBN 9780073107684. URL https://books.google.de/books?id=5-hSAAAAMAAJ.

[6] Christian Kunkelmann. *Numerical Modeling and Investigation of Boiling Phenomena*. PhD thesis, Technische Universität, Darmstadt, Mai 2011. URL http://tuprints.ulb.tu-darmstadt.de/2731/.

[7] Yohei Sato and Bojan Ničeno. A sharp-interface phase change model for a mass-conservative interface tracking method. *Journal of Computational Physics*, 249:127 – 161, 2013. ISSN 0021-9991. doi: https://doi.org/10.1016/j.jcp.2013.04.035. URL http://www.sciencedirect.com/science/article/pii/S0021999113003197.

[8] Mark D. Ratner, Fumitaka Goto, Daniel Kirk, and Paul A. Schallhorn. Modeling of upper stage cryogenic propellant stratification in a rotating , reduced gravity environment. In *Thermal and Fluids Analysis Workshop (TFAWs)*, Orlando, FL, August 8-12 2005. URL http://tfaws.nasa.gov/TFAWS05/Website/files/PropulsionPaperSession/TFAWS05_%20MRatner_PROP.pdf. Florida Institute of Technology.

[9] Martin Konopka, Anna Schubert, Diana Gaulke, Dennis Haake, Thorben Bruns, Alexander Fischer, and Jens Gerstmann. Liquid Hydrogen Propellant Management

Experiments and Simulations. In *JPC 2018 Proceedings. AIAA Propulsion and Energy Forum*, number AIAA 2018-4941. American Institute of Aeronautics and Astronautics, July 2018.

[10] J. W. Deardorff and G. E. Willis. Investigation of turbulent thermal convection between horizontal plates. *Journal of Fluid Mechanics*, 28(4):675–704, 1967. doi: 10.1017/S0022112067002393.

[11] R. Krishnamurti. Some further studies on the transition to turbulent convection. *Journal of Fluid Mechanics*, 60:285–303, January 1973. doi: 10.1017/S0022112073000170.

[12] International Launch Services Issues Additional Details on the Yamal 402 Proton Launch Anomaly Cause and Corrective Actions, 14/2/2013. URL `http://www.ilslaunch.com/newsroom`.

[13] Thales Makes Second Attempt to Adjust Yamal Orbit, 14/2/2013. URL `http://en.ria.ru/russia/20121211/178063835.html`.

[14] Jens Gerstmann. Research association upper stage, 2019. URL `https://www.dlr.de/irs/en/desktopdefault.aspx/tabid-11283/`.

[15] Jens Gerstmann, T. Arndt, Jörg Klatte, Uwe Rosendahl, Phillip Behruzi, and Rainer Kocik. Cryo-laboratories for test and development of propellant storage and management technologies. In *Ground-Based Space Facilities Symposium*, 2013. URL `https://elib.dlr.de/87258/`.

[16] W. Wagner. New vapour pressure measurements for argon and nitrogen and a new method for establishing rational vapour pressure equations. *Cryogenics*, 13(8):470–482, 1973. ISSN 0011-2275. doi: https://doi.org/10.1016/0011-2275(73)90003-9. URL `https://www.sciencedirect.com/science/article/pii/0011227573900039`.

[17] Matthias Hase. *Numerische Berechnung dreidimensionaler Transportvorgänge an angeströmten, sich verformenden Tropfen*. PhD thesis, Institut für Thermodynamik der Luft- und Raumfahrttechnik, University of Stuttgart, 2005.

[18] G. Son and V. K. Dhir. Numerical analysis of film boiling near critical pressures with a level set method. In *American Society of Mechanical Engineers, Heat Transfer Division, (Publication) HTD*, volume 342, pages 3–18, 1997. doi: http://dx.doi.org/10.1115/1.2830042. Only as print version. See ring binder.

[19] Mark Sussman, Peter Smereka, and Stanley Osher. A level set approach for computing solutions to incompressible two-phase flow. *Journal of Computational Physics*, 114(1):146 – 159, 1994. ISSN 0021-9991. doi: https://doi.org/10.1006/jcph.1994.1155. URL `http://www.sciencedirect.com/science/article/pii/S0021999184711557`.

[20] Damir Juric and Gratar Tryggvason. Computations of boiling flows. *International Journal of Multiphase Flow*, 24(3):387 – 410, 1998. ISSN 0301-9322. doi: 10.1016/S0301-9322(97)00050-5. URL `http://www.sciencedirect.com/science/article/pii/S0301932297000505`.

[21] Ichiro Tanasawa. Advances in condensation heat transfer. volume 21 of *Advances in Heat Transfer*, pages 55 – 139. Elsevier, 1991. doi: https://doi.org/10.1016/S0065-2717(08)70334-4. URL `http://www.sciencedirect.com/science/article/pii/S0065271708703344`.

[22] S. Hardt and F. Wondra. Evaporation model for interfacial flows based on a continuum-field representation of the source terms. *Journal of Computational Physics*, 227(11):5871 – 5895, 2008. ISSN 0021-9991. doi: https://doi.org/10.1016/j.jcp.2008.02.020. URL `http://www.sciencedirect.com/science/article/pii/S0021999108001228`.

[23] Matthias Wohak. *Numerische Simulation des Verdampfungsvorgangs eines Aufsteigenden Tropfens im Direkt-Kontakt mit einer heißeren, schwereren und nicht mischbaren Flüssigkeit*. Technische Hochschule Darmstadt, Fachbereich Maschinenbau, Darmstadt, 1996.

[24] Stefan Batzdorf. *Heat transfer and evaporation during single drop impingement onto a superheated wall*. PhD thesis, Technische Universität, Darmstadt, 2015. URL `http://tuprints.ulb.tu-darmstadt.de/4542/`.

[25] Samuel W.J. Welch and John Wilson. A volume of fluid based method for fluid flows with phase change. *Journal of Computational Physics*, 160(2):662 – 682, 2000. ISSN 0021-9991. doi: https://doi.org/10.1006/jcph.2000.6481. URL http://www.sciencedirect.com/science/article/pii/S0021999100964817.

[26] P.C. Stephan and C.A. Busse. Analysis of the heat transfer coefficient of grooved heat pipe evaporator walls. *International Journal of Heat and Mass Transfer*, 35(2):383 – 391, 1992. ISSN 0017-9310. doi: https://doi.org/10.1016/0017-9310(92)90276-X. URL http://www.sciencedirect.com/science/article/pii/001793109290276X.

[27] C. Ma and D. Bothe. Numerical modeling of thermocapillary two-phase flows with evaporation using a two-scalar approach for heat transfer. *Journal of Computational Physics*, 233:552–573, 2013. ISSN 0021-9991. doi: https://doi.org/10.1016/j.jcp.2012.09.011. URL https://www.sciencedirect.com/science/article/pii/S0021999112005426.

[28] Daniel Deising, Holger Marschall, and Dieter Bothe. A unified single-field model framework for volume-of-fluid simulations of interfacial species transfer applied to bubbly flows. *Chemical Engineering Science*, 139:173 – 195, 2016. ISSN 0009-2509. doi: https://doi.org/10.1016/j.ces.2015.06.021. URL http://www.sciencedirect.com/science/article/pii/S0009250915004297.

[29] Martin Rieber. *Numerische Modellierung der Dynamik freier Grenzflächen in Zweiphasenströmungen*. PhD thesis, Universität Stuttgart, 2004.

[30] Jan Schlottke. *Direkte Numerische Simulation von Mehrphasenströmung mit Phasenübergang*. PhD thesis, Institut für Thermodynamik der Luft- und Raumfahrttechnik, University of Stuttgart, January 2010.

[31] K.M. Wróbel. *Modelling and Numerical Simulation of Flows with Evaporation and Condensation*. PhD thesis, University of Twente, Enschede, 2006.

[32] Sébastien Tanguy, Michaël Sagan, Benjamin Lalanne, Frédéric Couderc, and Catherine Colin. Benchmarks and numerical methods for the simulation of boiling flows. *Journal of Computational Physics*, 264:1–22, May 2014. doi: 10.1016/j.jcp.2014.01.014. URL https://doi.org/10.1016%2Fj.jcp.2014.01.014.

[33] Martin Konopka, Peter Noeding, Jörg Klatte, Philipp Behruzi, Anton Stark, Nicolas Darkow, and Jens Gerstmann. Analysis of ln2 filling, draining, stratification and sloshing experiments. In *46th AIAA Fluid Dynamics Conference*, 2016. URL `https://elib.dlr.de/105016/`.

[34] Sebastian Schmitt. *Experimental and Numerical Investigations of Two-Phase Flow with Non-Isothermal Boundary Conditions under Microgravity Conditions*. PhD thesis, Center of Applied Space Technology and Microgravity (ZARM), University of Bremen, 2017.

[35] Paul Schallhorn, D Campbell, Sukh Chase, Jorge Piquero, Cindy Fortenberry, Xiaoyi Li, and Lisa Grob. Upper stage tank thermodynamic modeling using sinda/fluint. URL `https://arc.aiaa.org/doi/abs/10.2514/6.2006-5051`.

[36] NASA. Evaluation of AS-203 low gravity orbital experiment. Technical Report NASA-CR-94045, HSM-R421-67, BB-3.4.3-5-101, NASA, January 1967.

[37] Gary Grayson, Alfredo Lopez, Frank Chandler, Leon Hastings, and Stephen Tucker. *Cryogenic Tank Modeling for the Saturn AS-203 Experiment*. doi: 10.2514/6.2006-5258. URL `https://arc.aiaa.org/doi/abs/10.2514/6.2006-5258`.

[38] Olga Kartuzova and Mohammad Kassemi. Modeling interfacial turbulent heat transfer during ventless pressurization of a large scale cryogenic storage tank in microgravity. 07 2011. ISBN 978-1-60086-949-5. doi: 10.2514/6.2011-6037.

[39] Matthew Moran, Nancy B. McNelis, Maureen Kudlac, Mark S. Haberbusch, and George A. Satornino. Experimental results of hydrogen slosh in a 62 cubic foot (1750 liter) tank. (AIAA PAPER 94-3259), 07 1994.

[40] M. M. Hasan, C. S. Lin, and N. T. Vandresar. Self-pressurization of a flightweight liquid hydrogen storage tank subjected to low heat flux. (NASA-TM-103804), 07 1991.

[41] S. Barsi and M. Kassemi. Numerical and experimental comparisons of the self-pressurization behavior of an lh2 tank in normal gravity. *Cryogenics*, 48(3):122 – 129, 2008. ISSN 0011-2275. doi: https://doi.org/10.1016/j.cryogenics.2008.01.003. URL `http://www.sciencedirect.com/science/article/pii/S0011227508000040`.

[42] C. S. Lin and M. M. Hasan. Numerical investigation of the thermal stratification in cryogenic tanks subjected to wall heat flux. (AIAA PAPER 90-2375):19, 07 1990.

[43] Matthew Moran. Cryogenic fluid storage technology development: Recent and planned efforts at NASA. (NASA/TM-2009-215514), 12 2008.

[44] Nikolai Kulev and Michael Dreyer. Drop Tower Experiments on Non-isothermal Reorientation of Cryogenic Liquids. *Microgravity Sci. Technol.*, 22:463–474, 2010.

[45] Lisa Meyer. Contact angle in THETA. Technical Report DLR-IB xxx-2016 A xx, German Aerospace Center (DLR), 2016. Internal DLR Report.

[46] Sebastian Schmitt and Michael E. Dreyer. Free surface oscillations of liquid hydrogen in microgravity conditions. *Cryogenics*, 72:22 – 35, 2015. ISSN 0011-2275. doi: https://doi.org/10.1016/j.cryogenics.2015.07.004. URL `http://www.sciencedirect.com/science/article/pii/S0011227515000946`.

[47] Michael Dreyer. Propellant behavior in launcher tanks: an overview of the COMPERE program. *EUCASS Proceedings Series*, 1:253–266, 09 2009. doi: 10.1051/eucass/200901253.

[48] Carina Ludwig and Michael Dreyer. Analyses of cryogenic propellant tank pressurization based upon experiments and numerical simulations. In *5th EUCASS*, 2013. URL `https://elib.dlr.de/84708/`.

[49] Carina Ludwig. *Analysis of Cryogenic Propellant Tank Pressurization based upon Experiments and Numerical Simulations*. PhD thesis, University of Bremen, August 2014. URL `https://elib.dlr.de/105611/`.

[50] Philipp Behruzi, Jörg Klatte, Nicolas Fries, Andreas Schuette, Burkhard Schmitz, and Horst Koehler. Cryogenic propellant management sounding rocket experiments on TEXUS 48. 07 2013. ISBN 978-1-62410-222-6. doi: 10.2514/6.2013-3904.

[51] Philipp Behruzi and Mark Michaelis. Behavior of the cryogenic propellant tanks during the first flight of the Ariane 5 ESC-A upper stage. 07 2006. doi: 10.2514/6.2006-5052.

[52] Philipp Behruzi, Francesco De Rose, P. Netzlaf, Hans Strauch, and Airbus-Allee. Ballistic phase management for cryogenic upper stages. 2011. URL `https://www.flow3d.com/wp-content/uploads/2014/08/Ballistic-Phase-Management-for-Cryogenic-Upper-Stages.pdf`.

[53] Arnold van Foreest. *Modeling of cryogenic sloshing including heat and mass transfer*. PhD thesis, Deutsches Zentrum für Luft- und Raumfahrt, Januar 2014. URL `https://elib.dlr.de/105613/`.

[54] Arnold van Foreest. Modeling of cryogenic sloshing including heat and mass transfer. In *AIAA Joint Propulsion Conference, 25.-28. Juli 2010, Nashville, USA.*, Juli 2010. URL `http://elib.dlr.de/68140/`.

[55] Arnold van Foreest, M. Dreyer, and T. Arndt. Moving two-fluid systems using the volume-of-fluid method and single-temperature approximation. *AIAA Journal*, 49 (12):2805–2813, December 2011. URL `http://elib.dlr.de/75557/`.

[56] Onno Ubbink. *Numerical Prediction of Two Fluid Systems with Sharp Interfaces*. Department of Mechanical Engineering, Imperial College of Science, Technology & Medicine, London, 1997.

[57] Markus Gauer, Volker Hannemann, and Klaus Hannemann. Implementation of the VOF Method in the DLR TAU Code. In *JPC 2009 Proceedings. 45th AIAA/ASME/SAE/ASEE Joint Propulsion Conferences & Exhibit*, number AIAA 2009-4863. American Institute of Aeronautics and Astronautics, 2 - 5 Augut 2009.

[58] Markus Gauer and Klaus Hannemann. Interface Advection with the TAU Code and the CICSAM Method on Arbitrary Grids. In *7th International Conference on Multiphase Flow*, pages 1–9, Tampa, FL, USA, May 30th-June 4th 2010. University of Florida.

[59] Markus Gauer, Markus Lambert, Roland Kessler, and Klaus Hannemann. Two-phase Flow Modeling Combining The CICSAM with the Projection Method. In *JPC 2012 Proceedings. 48th AIAA/ASME/SAE/SAE/ASEE Joint Propulsion Conference & Exhibit*, number AIAA 2012-4298. American Institute of Aeronautics and Astronautics, July 2012.

[60] Markus Gauer. *Simulation of the Sloshing Behaviour of Two-phase Flows in Cryogenic Rocket Upper Stages*. PhD thesis, Institut für Thermodynamik der Luft- und Raumfahrttechnik, University of Stuttgart, 2013.

[61] Jakob Hurst. Implementation and Testing of a Time Dependent Acceleration Model for the Numerical Simulation of Sloshing. Technical Report DLR-IB 224-2013 A 91, German Aerospace Center (DLR), 2013. Internal DLR Report.

[62] J. U. Brackbill, D. B. Kothe, and C. Zemach. A Continuum Method for Modeling Surface Tension. *J. Comput. Phys.*, 100(2):335–354, June 1992.

[63] S. Patankar. *Numerical Heat Transfer and Fluid Flow*. Series in computational methods in mechanics and thermal sciences. Taylor & Francis, 1980. ISBN 9780891165224. URL `https://books.google.de/books?id=5JMYZMX3OVcC`.

[64] David Keiderling, Klaus Hannemann, Markus Gauer, and Jacob Hurst. Numerical modelling of cryogenic two-phase flow in the dlr tau code. In *Space Propulsion 2014*, number 963952 in Conference Proceedings on CD-ROM, pages 1–8, 2014. URL `https://elib.dlr.de/89114/`. Paper-Nr. SP2014-2963952, Session 62.

[65] L.E. Scriven. On the dynamics of phase growth: L. e. scriven, chem. engng. sci.10: 1–13, 1959. *Chemical Engineering Science*, 50(24):3905, 1995. ISSN 0009-2509. doi: https://doi.org/10.1016/0009-2509(96)81820-3. URL `http://www.sciencedirect.com/science/article/pii/0009250996818203`. Frontiers of Chemical Engineering Science.

[66] Markus Lambert, Roland Kessler, Massimiliano Di Domenico, and Erich Noll Berthold. The DLR THETA code the incompressible brother of TAU an overview. In *TAU User Meeting 2011*, October 2011. URL `https://elib.dlr.de/71306/`.

[67] Roland Kessler. THETA user-guide. 06 2019.

Affirmation

I declare that I have completed this dissertation single-handedly without the unauthorized help of a second party and only with the assistance acknowledged therein. I have appropriately acknowledged and cited all text passages that are derived verbatim from or are based on the content of published work of others, and all information relating to verbal communications. I consent to the use of an anti-plagiarism software to check my thesis. I have abided by the principles of good scientific conduct laid down in the charter of the Justus Liebig University Giessen "Satzung der Justus-Liebig-Universität Gießen zur Sicherung guter wissenschaftlicher Praxis" in carrying out the investigations described in the dissertation.

Göttingen, in February 2023

Signature, David Keiderling